Magnetothermal study of a superconducting coil in a carbon therapy cyclotron magnet

Auteur : Denis, Louis
Promoteur(s) : Vanderheyden, Benoit; Geuzaine, Christophe
Faculté : Faculté des Sciences appliquées
Diplôme : Master en ingénieur civil physicien, à finalité approfondie
Année académique : 2022-2023
URI/URL : http://hdl.handle.net/2268.2/17393

University of Liège

Faculty of Applied Sciences

Magnetothermal study of a superconducting coil in a carbon therapy cyclotron magnet

Academic supervisors:
Prof. Christophe GEUZAINE
Prof. Benoît VANDERHEYDEN

Jury members:
François HENROTTE
Vincent NUTTENS
Prof. Philippe VANDERBEMDEN

Master's Thesis conducted by Louis DENIS
for obtaining the Master's Degree in Engineering Physics

Academic year 2022-2023

ACKNOWLEDGEMENTS

Over the last few months, I have received the support of many people, and I would like to take this opportunity to thank them.

First of all, I am extremely grateful to my academic supervisors, Prof. Christophe Geuzaine and Prof. Benoît Vanderheyden, for sharing their invaluable expertise with me. Their constant availability and support have played a fundamental role in my progress through every step of this work. Through our weekly meetings, they have always steered me in the right direction while providing constructive suggestions to keep improving this manuscript.

I would like to warmly thank my IBA advisor, Vincent Nuttens, for taking so much of his time to share his knowledge of cyclotrons with me. He was able to answer all my questions and, thanks to him, I always felt welcome and supported at the IBA office in Louvain-la-neuve.

In addition, I am also immensely thankful to the whole IBA team for giving me the incredible opportunity to present some results of this thesis at the 14th International Particle Accelerator Conference in Venice last May. It has been a truly extraordinary experience. I thank Gaëlle Gérard, Philippe Caillau, Jacob Kelly, Marc Leenheer, Philippe Velten, Laurent Maunoury and Virgile Letellier for welcoming me into their team during the conference. Again, special thanks go to Prof. Christophe Geuzaine, Prof. Benoît Vanderheyden and Vincent Nuttens for helping me write my first paper.

I would like to thank the members of my jury, François Henrotte, Vincent Nuttens and Prof. Philippe Vanderbemden for agreeing to evaluate my work. I would also like to express my gratitude to Prof. Philippe Vanderbemden for introducing me to the fascinating world of superconductivity.

Last but certainly not least, I thank my family and friends for their support during my studies. In particular, I must express my deepest gratitude to my parents for their constant encouragement over the years. I cannot thank them enough for their incredible support.

ABSTRACT

The C400 is the first compact superconducting cyclotron used for carbon therapy in the world. During the ramp-up procedure from zero to nominal current, the changing magnetic field leads to heat dissipation within the superconducting coil. The aim of this thesis is to predict the magnetothermal behaviour of the superconducting coil during ramp-up. To this end, a finite element model of the C400 has been developed using the GetDP open-source software.

Based on a detailed theoretical background, the magnetic and thermal models are first described individually as their numerical parameters are fine-tuned for optimal efficiency. The magnetothermal results are then studied in detail. The hysteresis losses, occurring in superconducting filaments, play a central role in the magnetothermal behaviour of the coil, as the inter-filament coupling losses are found to be negligible. Due to the efficiency of the liquid helium cooling system, the maximal temperature rise in the coil is less than 0.01 K. The results are compared with expectations from dimensional analysis and several parametric studies are carried out. Among other results, the ramp-up procedure cannot be performed in less than 20 minutes and an optimized current profile allows the maximal temperature rise to be reduced by 14 %.

In the second part of this work, a filament model is introduced to compute the hysteresis loss at the superconducting filament scale. The results are compared with analytical approximations, highlighting the complexity of the physical phenomena involved. Among other observations, the critical current density dependence on flux density and the effect of transport current on flux penetration cannot be neglected. Finally, a multi-scale approach, based on the filament model, is proposed and implemented for computing the hysteresis loss within the coil, together with the corresponding temperature distribution. Its robustness significantly improves the accuracy of the results, since analytical approximations underestimate the losses in the intermediate field regime.
The observed temperature rise in the coil is small and the filaments should remain in the superconducting state during a regular ramp-up procedure.

CONTENTS

INTRODUCTION

Developed in collaboration between Ion Beam Applications (IBA) and Normandy Hadrontherapy (NHa), the C400 is a compact superconducting cyclotron used for carbon therapy [1]. Superconducting cyclotrons are at the cutting edge of technology, combining many complex physical phenomena involving both ferromagnetic and superconducting materials, while relying on cryogenic equipment for cooling. The remarkable properties of the superconducting Nb-Ti alloy used in the C400 coil allow it to carry large currents without dissipating much energy [2], making it possible to generate large magnetic fields required for accelerating ions in a compact environment. During the ramp-up procedure from zero to nominal current, the changing magnetic field leads to heat dissipation within the superconducting coil. It is critical to accurately predict the temperature rise of the coil, as an excessive temperature increase would drive the superconductor out of its superconducting state. In such a case, the magnetic energy contained in the cyclotron would be released in the form of heat, potentially causing irreversible damage to the device [3].

The main goal of this study is to develop a numerical model to predict the magnetothermal behaviour of the coil during the C400 energization process. It involves solving for the magnetic field in the cyclotron, while computing the temperature distribution inside the superconducting coil during ramp-up. The most popular approach for modelling such a behaviour is the finite element method. To this end, the GetDP [4] open-source software is used for solving the finite element problem. It provides a complete control of the numerical modelling, which allows to freely describe the coupling between magnetodynamics and thermodynamics. The mesh required for discretizing the finite element problem is produced by the Gmsh [5] open-source software.

This thesis is divided into eight chapters. The medical context of the study is presented in Chapter 1, where the concept of hadron therapy is briefly introduced before discussing the basic working principle of isochronous cyclotrons. The C400 geometry is described in Chapter 2, where the symmetries of the device are used for modelling one eighth of the cyclotron. The modelling assumptions are discussed and a simplified axisymmetric model is also introduced for preliminary computations.

The theoretical background required for modelling the various physical phenomena is presented in Chapter 3. The theory related to magnetodynamic modelling heavily relies on the previous works of Geuzaine [6] and Dular [7]. An extensive description of superconducting materials is provided, including practical considerations and theoretical models for the constitutive law of superconductors. The different types of losses in composite conductors are discussed in the last part of the chapter. In particular, analytical approximations for hysteresis losses in Nb-Ti filaments are adapted from [8].

The magnetic model of the cyclotron is introduced in Chapter 4. After studying their sensitivity to numerical parameters, magnetostatic and magnetodynamic results are presented. Models of increasing complexity are investigated, from a two-dimensional axisymmetric geometry to the full three-dimensional geometry of the cyclotron. The differences between the various configurations are also highlighted. The thermal model of the coil is described in Chapter 5 and the effective thermal properties of the homogenized coil are derived. Furthermore, the magnetic and thermal time constants of the system are determined in these two chapters.

The coupled magnetothermal model is presented in Chapter 6, where the corresponding results are discussed and a physical interpretation is provided. Additionally, the order of magnitude of the temperature rise is compared with expectations based on dimensional analysis. The difference between the simplified axisymmetric model and the full three-dimensional model is also highlighted. In the last part of the chapter, several parametric studies are carried out. Among others, the effect of the cooling efficiency and the effect of the total ramp time on the temperature rise are investigated. This chapter provides a comprehensive description of the magnetothermal behaviour of the coil during the ramp-up procedure.

In Chapter 7, the accuracy of the analytical approximations used for computing the hysteresis loss in the coil is evaluated. For this purpose, a model at the filament scale is introduced. The influence of several physical parameters on the hysteresis loss in Nb-Ti filaments is studied and numerical results are compared with analytical predictions. Again, a physical interpretation of the various observations is provided.

In Chapter 8, the models described in Chapter 6 and Chapter 7 are combined and a multi-scale approach is proposed to determine the maximal coil temperature during the ramp-up procedure. After discussing the implementation of the method, the final results are compared with those presented in Chapter 6 and the robustness of the multi-scale approach is highlighted.

Computational resources have been provided by the Consortium des Équipements de Calcul Intensif (CÉCI), funded by the Fonds de la Recherche Scientifique de Belgique (F.R.S.-FNRS) under Grant No. 2.5020.11. In particular, all computing times reported in this study have been measured on the NIC5 cluster, hosted at the University of Liège and operated by the CÉCI. The convention for mathematical notations used throughout the thesis is described in Appendix A.1.

CHAPTER 1
MEDICAL CONTEXT

The purpose of the C400 cyclotron is to accelerate protons and carbon ions for treating cancer. In this chapter, the conventional radiotherapy, involving photons, is compared to hadron therapy with protons and carbon ions. Their respective advantages are discussed. In the second part of the chapter, the working principle of cyclotrons for medical applications is briefly described. In particular, the focus is set on the isochronous cyclotron.

1.1 Radiation therapy for cancer treatment

Throughout the 20th century, the knowledge of particle physics rapidly evolved following Wilhelm Röntgen's discovery of a new type of radiation known as X-rays, in 1895 [9]. Photons were immediately used for medical applications, as the first X-ray radiograph was performed in 1896. In 1901, the first use of radiation for cancer treatment was brachytherapy, in which a radioactive source was placed near the tumor to be treated. In the 1930s, the first experiments on *radiotherapy* involving X-rays for healing diseased animals were conducted. During this time, scientists also achieved successful results using neutron beams. Unlike photons, neutrons have mass, marking the emergence of what is nowadays called *hadron therapy*. The technology continued to evolve, and in 1946, Wilson proposed the use of accelerated protons for hadron therapy [10]. Since then, the impact of various particles on tumors has been studied. Today, both conventional radiotherapy and hadron therapy remain popular and effective cancer treatment techniques, alongside *chemotherapy*. Hadron therapy is mostly performed using protons and carbon ions [9].

To understand the difference between conventional radiotherapy and hadron therapy, their working principles must be introduced. In a simplified way, diseased cells can grow in an uncontrolled manner, forming a cluster known as a tumor. In radiotherapy, a high-energy photon beam (~ 10 MeV) is applied to the tumor, where the photon transfers its energy to electrons through ionization processes. These energetic electrons can then collide with cells and in particular, they can break the DNA of diseased cells.
Unfortunately, using this type of radiotherapy, a significant dose is also deposited in the healthy tissues surrounding the tumor. The dose deposited in tissues varies smoothly with the depth of deposition, unlike what is observed for hadron therapy methods [11]. For charged particle beams, ionization occurs mostly at the end of the penetration range [12]. As a result, the dose transmitted to tissues exhibits a Bragg peak, first observed by William Henry Bragg in 1904 [13]. Bragg peaks for proton and carbon ion beams are shown in Fig. 1.1. The depth of the Bragg peak can be adjusted by tuning the energy of the particles.

Such a radiation peak allows the focus of radiation on the tumor without strongly affecting the surrounding healthy tissues. Conversely, a higher dose can be delivered to the tumor while maintaining the same irradiation level in healthy tissues as achieved using X-rays. This property is particularly important when dealing with children: hadron therapy reduces the probability of developing later tumors compared to conventional radiotherapy [9].

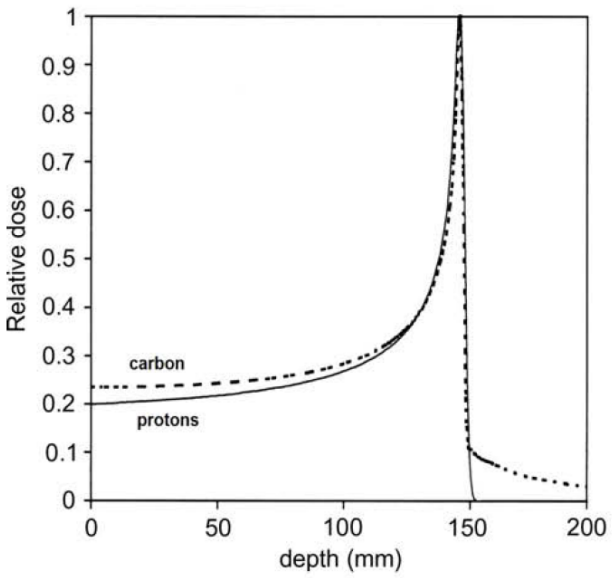

Figure 1.1: Relative dose distributed in tissues against depth of proton and carbon ion beams calibrated for a Bragg peak at $\sim$ 14 cm. Figure from [12].

As observed in Fig. 1.1, the relative dose after the Bragg peak drops more rapidly using protons. However, working with carbon ions offers a significant advantage. Since the charge of carbon ions is six times greater than that of single protons, the ionization density of carbon ions is 36 times larger [11]. This results in a much lower lateral spread of ionization in tissues for carbon ion beams compared to proton beams. Additionally, due to their charge, carbon ions decelerate more rapidly when reaching their Bragg peak. Without delving into details, in addition to the secondary ionization process associated with the emission of high-energy electrons (already discussed for photons), primary ionization processes occur within the tumor when using carbon ions. This is not the case for proton beams. Primary ionization processes arise from the interaction of carbon ions with molecules and lead to denser ionizations, potentially causing double strand breaks. Consequently, carbon therapy proves more effective in treating radioresistant and hypoxic tumors, which lack oxygen and are less responsive to secondary ionizations [9]. However, while the proton therapy industry is already well-developed, carbon therapy is still in the process of being commercialized. Nevertheless, carbon therapy has already demonstrated remarkable efficiency in the treatment of various types of malignancies [14], and the future prospects for this technology are highly promising.

IBA is a leader in the hadron therapy market and is the most experienced company in proton therapy. It has successfully launched multiple particle accelerators for proton therapy, such as the C235 isochronous cyclotron and the S2C2 synchrocyclotron. The C235 cyclotron is based on a normal-conducting magnet, while the S2C2 relies on superconducting Nb-Ti. The C400 cyclotron studied in this work is a superconducting isochronous cyclotron for proton therapy and carbon therapy. It is developed in collaboration between IBA and NHa [1]. Its main advantage is the possibility for medical centers to produce proton and carbon ion beams with one single machine.
In the C400, $^{12}C^{6+}$ carbon ions are accelerated to 400 MeV/u (or 4800 MeV). Protons are usually accelerated to 230 MeV. Next, the concept of isochronous cyclotron is described.

1.2 Isochronous cyclotron

To understand the utility of isochronism in a cyclotron, the basic working principle of the classic cyclotron is presented first, and some of its implications are discussed.
In a cyclotron, an ion (charge q in [C] and mass m in [kg]) with velocity v [m/s] in a flux density

$\boldsymbol{b}$ [T] follows a circular orbit of radius r [m], due to the centripetal Lorentz force $\boldsymbol{f}_L = q\boldsymbol{v} \times \boldsymbol{b}$ (in [N]). Its angular frequency ω [rad/s] is then given by

$$\omega = \frac{v}{r} = \frac{qb}{m}. \tag{1.1}$$

While magnetic induction b bends the trajectory of the charged particle, it cannot accelerate the particle, as the work done by the Lorentz force is equal to zero: $\boldsymbol{f}_L \cdot \boldsymbol{v} = 0$. The particle is accelerated by means of an electric field $\boldsymbol{e}$ [V/m]. In practice, radiofrequency (RF) cavities are used to transfer energy to the particle. For consistent acceleration, the angular frequency of the electric field must be the same as or a multiple of the revolution frequency of the particle, given by Eq. (1.1) [15].
In a classic cyclotron, the flux density $\boldsymbol{b}$ is assumed to be uniform in space. In that case, the maximum energy that can be reached is limited by the relativistic mass increase that needs to be taken into account for high-energy particles. More generally, the angular frequency is

$$\omega = \frac{qb}{m} = \frac{qb}{\gamma m_0} = \frac{qb}{m_0}\sqrt{1 - \left(\frac{v}{c}\right)^2}, \tag{1.2}$$

with γ [-] the relativistic factor, m_0 [kg] the ion rest mass and c [m/s] the speed of light [16]. The relativistic impact is not negligible as for carbon ions at 4800 MeV, $\gamma = 1.43$. At any given moment, the frequency of the electric field in RF cavities must match Eq. (1.2). However, the velocity v of the particle increases with the radius r of its orbit. Therefore, if the magnetic induction b is uniform, the frequency of the electric field must be adjusted as r increases.

A second issue arises in the case of a classic cyclotron: orbit stability [15]. Due to its transverse dimensions, not all of the beam circulates exactly in the median plane of the cyclotron or on the ideal trajectory. Instead, it oscillates around it, as shown in Fig. 1.2. Radial deviations are observed in the median plane of the cyclotron, while axial deviations are perpendicular to the median plane.

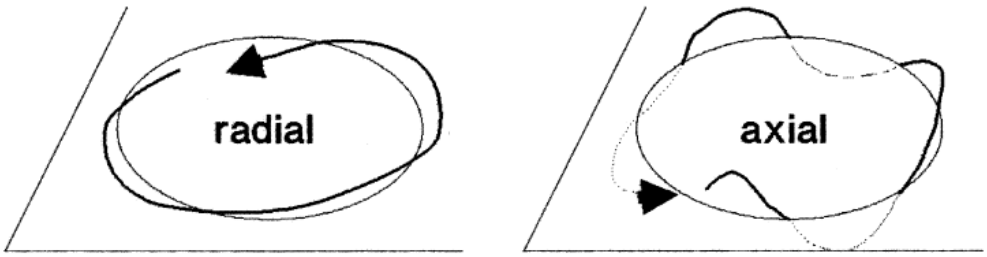

Figure 1.2: Illustration of the concepts of radial and axial stability of a charged particle in a cyclotron. The circular path (equilibrium orbit) represents the ideal trajectory of a particle at constant velocity, while the modified path is a perturbed yet stable trajectory. The oscillation amplitude is not at scale. Figure from [15].

For the particle trajectory to remain stable, focusing Laplace forces are required to act against the deviations. Focusing can be achieved with a flux density varying with the radial position. The spatial evolution of the magnetic induction is typically described by

$$b(r) = b_0 \left(\frac{r}{r_0}\right)^{-n_b}, \tag{1.3}$$

with n_b [-] the field index and b_0 [T] and r_0 [m] some reference quantities [16]. From [15], radial orbit stability is achieved for $n_b < 1$ and axial orbit stability for $n_b > 0$. Hence, the condition for global orbit stability is $0 < n_b < 1$. In a classic cyclotron, the field index is $n_b = 0$ and the stability condition is not met.

One possible way to achieve orbit stability while accounting for the relativistic mass increase (Eq. (1.2)) is through the use of a synchro-cyclotron. In a synchro-cyclotron, the flux density decreases with radius, indicated by a positive field index n_b, which ensures orbit stability. To satisfy Eq. (1.2), the frequency of RF cavities also decreases with radius to balance the simultaneous induction decrease and mass increase [16]. This principle has been exploited in the IBA S2C2.

In an isochronous cyclotron, the frequency of RF cavities remains constant. For satisfying Eq. (1.2), the field index must be negative meaning the flux density in the median plane increases with radial position [16]. As a result, the axial stability condition is not met, and additional axially focusing forces are required. These forces are achieved with an azimuthally varying field (AVF) cyclotron.
In practice, the magnet of the cyclotron is modified to induce high magnetic field zones (hills or poles) and low field zones (valleys), as shown in Fig.1.3. Consequently, the equilibrium orbit is no longer perfectly circular. In high field zones, the ions have a smaller radius of curvature compared to low field zones. As a result, the velocity of ions is no longer exclusively azimuthal but now has a radial component. At the transition between hills and valleys, the magnetic induction has an azimuthal component. It can be shown that the corresponding local Lorentz force provides strong focusing [15]. Please refer to [15] for a detailed and graphical demonstration.

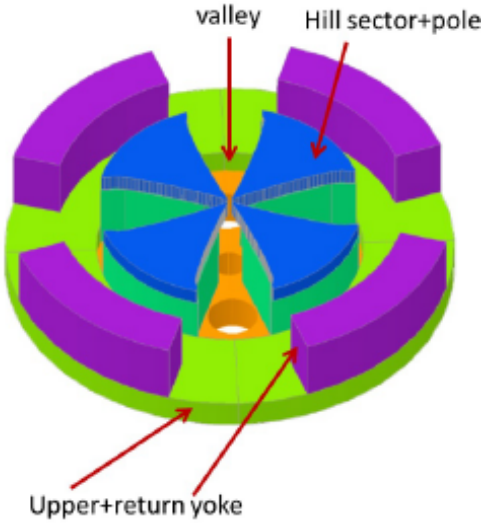

Figure 1.3: Yoke shape of an azimuthally varying field cyclotron. Figure from [16].

This concept was first introduced by Thomas in 1938 [16] and the corresponding forces are thus called Thomas forces. In an isochronous cyclotron, focusing Thomas forces overcome the vertical defocusing caused by the negative field index and axial stability is achieved. In practice, the focusing obtained with AVF cyclotrons can be significantly increased by using spiralized poles instead of straight poles. Due to the shape of the poles, the local Lorentz force at hill/valley transitions is alternatively focusing and defocusing. That alternating focusing can be quite strong [16].

In the C400 cyclotron, which is described in detail in the next chapter, isochronism has been respected to account for the relativistic mass increase. It enables a constant frequency of the electric field in RF cavities. The negative field index related to isochronism has been achieved with an elliptical pole gap. As the vertical gap between the poles decreases, the magnetic field in the median plane increases. Moreover, the spiralized poles ensure vertical focusing of the ion beam.
A strong magnetic field is required for the ions to reach high energy within a compact space. In the C400, it is produced by a superconducting coil in combination with a ferromagnetic yoke used to channel flux lines. The superconducting coil allows the C400 to be the first compact superconducting cyclotron used for carbon therapy in the world.

As mentioned earlier, the C400 accelerates $^{12}C^{6+}$ carbon ions to 4800 MeV. As shown in Eq. (1.1), the charge-to-mass ratio q/m governs the beam dynamics. To maintain this ratio constant for the production of proton beams, $^{2}H^{+}$ ions are accelerated (to 230 MeV/u). At extraction, the $^{2}H^{+}$ beam passes through a stripper foil, a thin carbon sheet that breaks the bond between the two protons [16]. Consequently, the resulting H^{+} protons possess a kinetic energy of 230 MeV.

CHAPTER 2
GEOMETRY AND PROBLEM DEFINITION

As mentioned in the first chapter, the C400 cyclotron is an isochronous cyclotron with spiralized poles and elliptical gap. Its first design was proposed by IBA in 2007 [17]. The cyclotron is owned by Normandy Hadrontherapy (NHa) and its current design status can be found in [1]. This chapter focuses on the geometrical description of the C400 model studied in this thesis.

The cyclotron exhibits a reflection symmetry in the middle of the pole gap. The x-z symmetry plane is further referred to as the *median plane* of the cyclotron. The vertical axis is the $\hat{\boldsymbol{y}}$-axis. One realistic view of the bottom half of the ferromagnetic yoke is shown in Fig. 2.1(a). Please note that the mapping system also represented in the figure does not belong to the permanent cyclotron design. The yoke does not exhibit a four-fold rotational symmetry, due to the single extraction channel at the bottom of Fig. 2.1(a). Nevertheless, the geometry has been simplified by IBA in order to take advantage of that four-fold rotational symmetry as represented in Fig. 2.1(b). The equivalent symmetric model has been designed in order to take the impact of the single extraction channel into account using effective radial extraction channels. In practice, the central vertical hole in the yoke contains the injection line, for injecting low-energy particles inside the cyclotron cavity.

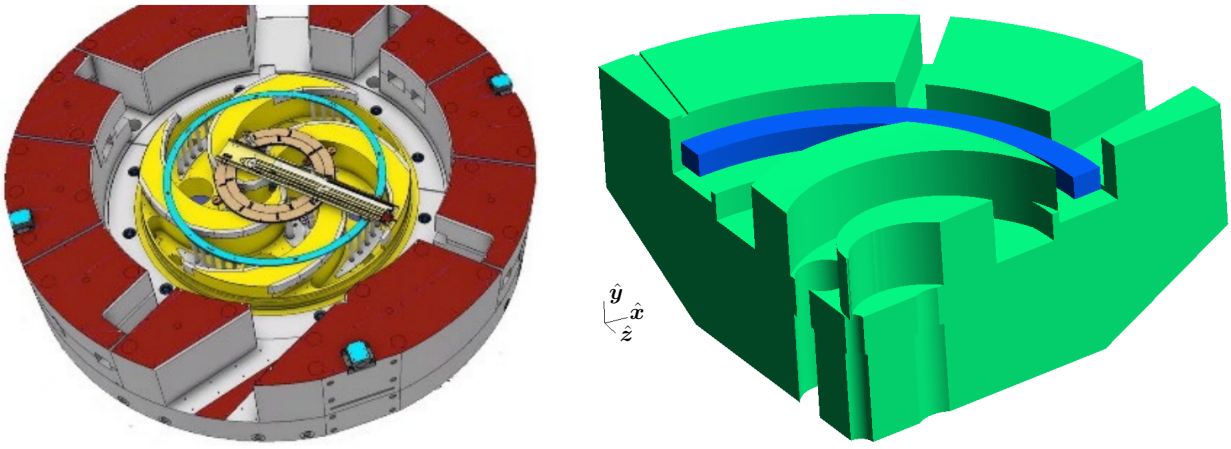

(a) (b)

Figure 2.1: (a) Bottom part of the ferromagnetic yoke. Figure from [18]. The light brown and cyan rings as well as the central rod are parts of the temporary mapping design developed in [18].
(b) One quarter of the bottom part of the ferromagnetic yoke (in green) and the bottom superconducting coil (in blue), from the CAD file *c400_vs4.stp* prepared by IBA. For scale, the radius of the yoke is ~ 3.5 m.

Consequently, one eighth of the cyclotron has been modelled in this work, with Gmsh [5] and GetDP [4]. Implementing the symmetries has allowed to reduce the number of degrees of freedom of the numerical system to be solved, as well as the computing times. The final model of the C400 is shown in Fig. 2.2. For confidentiality reasons, the exact dimensions of the model are not included in this report. They have been retrieved from the CAD file *c400_vs4.stp* provided by IBA. The choice has been taken to model one quarter of the top part (not the bottom part !) of the cyclotron. Note that an offset angle of $\theta_{\text{offset}} = 0.2$ rad has been introduced in the final geometry to ease mesh generation. Moreover, the present model also takes the helium vessel into account.

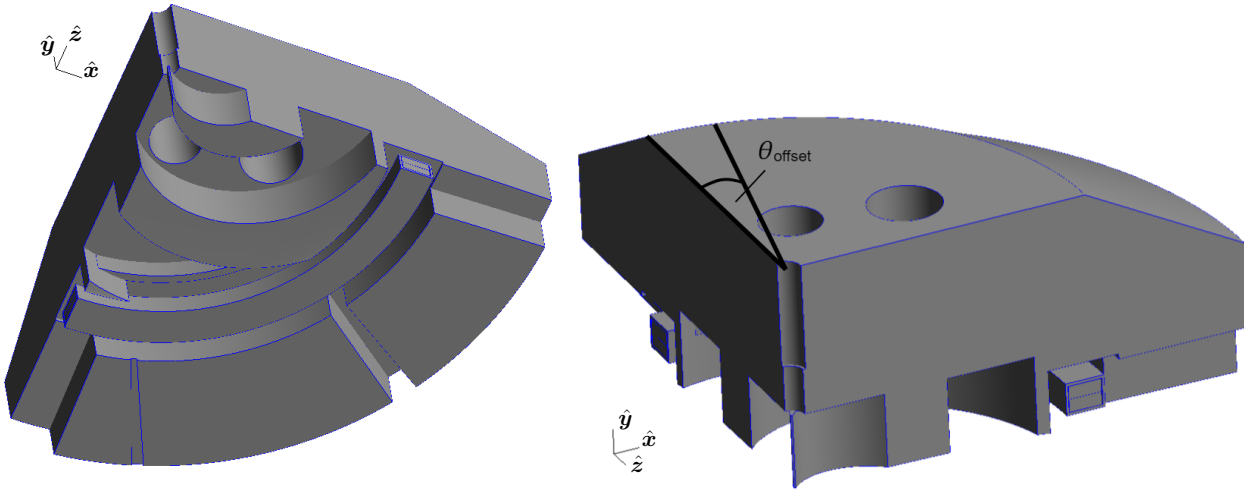

Figure 2.2: Numerical model of one quarter of the cyclotron top part implemented in Gmsh and GetDP. Only solid parts are shown: the ferromagnetic yoke, the helium vessel and the coil. For scale, the radius of the yoke is ~ 3.5 m.

Air is assumed outside of the cyclotron. The ferromagnetic yoke is made of iron and is at room temperature. Perfect vacuum is assumed in the central cavity of the yoke. The helium vessel is made of stainless steel (SS304L). Inside the helium vessel, liquid helium is assumed to be at a temperature of $T_{\text{He}} = 4.2$ K. The helium vessel is the central part of the cryostat used to cool the coil. Together, the helium vessel and the coil form the *cold mass* of the cyclotron. The coil is immersed in flowing liquid helium and split in two sub-coils for a total of 1344 conductor turns ($N_{\text{t}} = 672$ turns per sub-coil). Note that the cyclotron contains four sub-coils and two of them above the median plane. The conductor is made of copper and superconducting Nb-Ti and its exact composition is further discussed in Section 3.3.1.

The goal of this study is to solve for the magnetic field in the cyclotron, while retrieving the temperature distribution inside the superconducting coil during *ramp-up*. The ramp-up of the cyclotron consists in the energization of the coil, starting from zero current to reach nominal operating current. The beam extraction mechanism, the beam injection line as well as the RF cavities are neglected from a magnetic point of view. Liquid helium is considered as vacuum. The focus is set on the superconducting coil itself. A simplified axisymmetric geometry is used several times for preliminary computations in this study. An axisymmetric model enables working in two dimensions, significantly reducing computing times. It is presented next.

2.1 Simplified axisymmetric geometry

The axisymmetric model used for preliminary studies is represented in Fig. 2.3. It has been obtained by neglecting the yoke cavities, the off-center vertical holes in the yoke and the extraction channels.

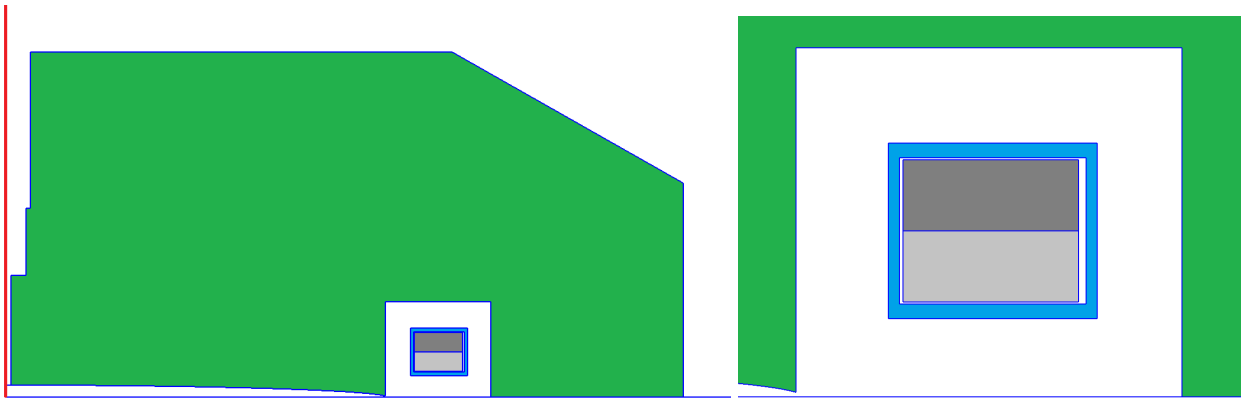

(a) Axisymmetric top part of the yoke. (b) Helium vessel - coil assembly.

Figure 2.3: Top part of the simplified axisymmetric yoke (in green) and its internal components: the helium vessel (in blue) and the two sub-coils (top part in dark grey, bottom part in light grey). The vacuum and the air are represented in white. The outer domain is not represented. The geometry is simplified to be made axisymmetric with respect to the $\hat{\boldsymbol{y}}$-axis (in red).

Figure 2.3(b) represents the cross-section of the helium vessel - coil assembly, which is axisymmetric by definition. The radial width of the coil is denoted by w_{coil} [m] and its height by h_{coil} [m]. The top sub-coil is further referred to as *sub-coil 1*, the bottom one as *sub-coil 2*. In practice, the assembly is supported by a stainless steel support located between the lower coil (below the median plane, not shown) and the upper coil. It is also neglected in this work. The horizontal space between the coil and the vessel is larger than the vertical space, as radial movement can occur during cool-down or energization. The space is assumed to be completely filled with liquid helium. Grooved plates are placed at the top and bottom surfaces of the coil, which are designed to allow efficient circulation of the liquid helium. Again, the grooves are neglected.

2.2 Current profile

In this work, linear current profiles are considered. The total ramp-up time of the C400 cyclotron is 2 hours: $T_{\text{up}} = 7200$ s. Tab. 2.1 gathers the different nominal current configurations in the conductor composing the two sub-coils represented in Fig. 2.3(b). The two different carbon configurations constitute two different solutions for accelerating carbon ions as they produce a very similar flux density in the median plane. Such an observation is also valid for the two proton configurations. Configuration 0 is the default configuration in which most of the results of this study are obtained, unless otherwise specified. The intentional current asymmetry between the two sub-coils is implemented for beam dynamics purposes. It is achieved by applying an opposite voltage difference between the terminals of sub-coil 2. In the following, the *steady-state* solution corresponds to the calculated static magnetic flux density distribution at nominal current.

Configuration	0	Carbon 1 (C1)	Carbon 2 (C2)	Proton 1 (P1)	Proton 2 (P2)
i_1 [A]	1002	990	1015	990	1015
i_2 [A]	918	948	932	1034	1015

Table 2.1: Different nominal current conditions investigated. Current in the conductor of sub-coil 1 is denoted i_1 [A], for a total current in sub-coil 1 of $I_1 = N_{\text{t}} i_1$. The four last columns correspond to C400 operating conditions during beam extraction. Please note that these are hypothetical values, subject to modification and used for modelling purposes.

CHAPTER 3

THEORETICAL BACKGROUND

Now that its geometry has been presented, this chapter focuses on establishing the theoretical background required for modelling the magnetothermal behaviour of the C400 cyclotron. First, magnetodynamics is discussed, introducing the magneto-quasi-static approximation. This chapter also presents the properties of ferromagnetic materials and superconducting materials, which play a crucial role in the working principle of the C400 cyclotron. Furthermore, a more detailed description of superconductivity, along with practical considerations, is provided. The heat equation and other thermodynamic quantities are also discussed. Finally, the physical coupling mechanisms between magnetodynamics and thermal physics are presented. In particular, the losses occurring in superconducting cables are described in detail, as they will play a central role in the magnetothermal behaviour of the coil, as highlighted in Chapter 6.

3.1 Magnetodynamics

Maxwell's equations are valid in any medium:

$$\nabla \cdot \boldsymbol{b} = 0, \qquad (3.1) \qquad\qquad \nabla \cdot \boldsymbol{d} = \rho_e, \qquad (3.2)$$

$$\nabla \times \boldsymbol{h} = \boldsymbol{j} + \partial_t \boldsymbol{d}, \qquad (3.3) \qquad\qquad \nabla \times \boldsymbol{e} = -\partial_t \boldsymbol{b}, \qquad (3.4)$$

with $\boldsymbol{b}$ [T] denoting the flux density, $\boldsymbol{d}$ [C/m^2] the electric displacement field, $\boldsymbol{h}$ [A/m] the magnetic field, $\boldsymbol{e}$ [V/m] the electric field, $\boldsymbol{j}$ [A/m^2] the current density and ρ_e [C/m^3] the electric charge density [19]. Equations (3.1) to (3.4) are referred to as the differential forms of Gauss's law for magnetism, Gauss's law for electricity, Ampère-Maxwell's law, and Faraday's law, respectively. Source terms $\boldsymbol{j}$ and ρ_e, along with constitutive laws, initial and boundary conditions, allow to solve for the electromagnetic fields in the domain of study Ω. In this work, the boundary of Ω is denoted by $\Gamma = \partial\Omega$.
Constitutive laws describe the interaction of the medium with electromagnetic fields. They allow to close the system of Maxwell's equations:

$$\boldsymbol{b} = \mu \boldsymbol{h}, \qquad (3.5) \qquad\qquad \boldsymbol{d} = \varepsilon \boldsymbol{e}, \qquad (3.6)$$

with μ [H/m] denoting the permeability of the medium and ε [F/m] its permittivity. In an isotropic medium, they can both be considered as scalar values. Generally, they are expressed as

$$\mu = \mu_0 \, \mu_r \left(\boldsymbol{h} \right), \qquad (3.7) \qquad\qquad \varepsilon = \varepsilon_0 \, \varepsilon_r \left(\boldsymbol{e} \right), \qquad (3.8)$$

with $\mu_0 = 4\pi \times 10^{-7}$ H/m the free space magnetic permeability, $\varepsilon_0 = 8.854 \times 10^{-12}$ F/m the free space electric permittivity, the relative permeability $\mu_r\,(\boldsymbol{h})$ [-] and the relative permittivity $\varepsilon_r\,(\boldsymbol{e})$ [-] accounting for the material response. The relative permeability of the C400 ferromagnetic yoke is described in Section 3.2. As mentioned later in this work, it is convenient to express the magnetic constitutive law (Eq. (3.5)) in terms of the reluctivity $\nu = \mu^{-1}$ [m/H] as

$$\boldsymbol{h} = \nu\,(\boldsymbol{b})\,\boldsymbol{b}. \tag{3.9}$$

For normal conductors (e.g. iron or stainless steel), the electric field is linked to the current density through Ohm's law:

$$\boldsymbol{j} = \sigma \boldsymbol{e}, \tag{3.10}$$

with the electrical conductivity σ [S/m] being considered independent of the electric field. Please note however that the electrical conductivity depends on temperature [20]. Equation (3.10) is not valid for materials in the superconducting state, for which the conductivity strongly depends on the electric field $\sigma\,(\boldsymbol{e})$. This is discussed in Section 3.3.
As in the previous works of Geuzaine [6] and Dular [7], the conducting part of the domain, for which Eq. (3.10) is valid, is denoted by Ω_{c}. By contrast, the current density is assumed equal to zero in air and in vacuum:

$$\boldsymbol{j} = \boldsymbol{0}. \tag{3.11}$$

Air and vacuum are the non-conducting part of the domain, denoted by $\Omega_{\mathrm{c}}^{\mathrm{C}} = \Omega \backslash \Omega_{\mathrm{c}}$.
In stranded conductors, the source current density is imposed

$$\boldsymbol{j} = \boldsymbol{j}_{\mathrm{s}} \tag{3.12}$$

and it is assumed independent of the local electromagnetic fields [6]. The volume of stranded conductors is denoted Ω_{s} and numerically, it is a subset of $\Omega_{\mathrm{c}}^{\mathrm{C}}$ as eddy currents are neglected. Hence, in $\Omega_{\mathrm{c}}^{\mathrm{C}}$, the current density is

$$\boldsymbol{j} = \begin{cases} \boldsymbol{j}_{\mathrm{s}}, & \text{in } \Omega_{\mathrm{s}}, \\ \boldsymbol{0}, & \text{in } \Omega_{\mathrm{c}}^{\mathrm{C}} \backslash \Omega_{\mathrm{s}}. \end{cases} \tag{3.13}$$

As the dimensions of the system are much smaller than the electromagnetic characteristic wavelength (see Appendix A.4), the displacement current term $\partial_t \boldsymbol{d}$ can be neglected and Ampère's law (Eq. (3.3)) reduces to

$$\nabla \times \boldsymbol{h} = \boldsymbol{j}, \tag{3.14}$$

which is called the magneto-quasi-static (MQS) approximation [2]. In that case, the energy is mostly stored under magnetic form, as expected for a cyclotron. The MQS approximation is particularly valid when dealing with good conductors and thus, it is valid inside superconductors.
In terms of magnetic boundary conditions, an interface between two regions, region 1 and region 2, is considered. Denoting by $\boldsymbol{n}$ the normal unit vector pointing from region 1 into region 2, the following boundary conditions must be satisfied at any instant:

$$\boldsymbol{n} \times (\boldsymbol{h}_2 - \boldsymbol{h}_1) = \boldsymbol{K}, \tag{3.15}$$

$$\boldsymbol{n} \cdot (\boldsymbol{b}_2 - \boldsymbol{b}_1) = 0, \tag{3.16}$$

with $\boldsymbol{K}$ [A/m] the surface current at the interface and $\boldsymbol{x}_i$ the quantity $\boldsymbol{x}$ evaluated at the interface in region i [2]. Similarly, the tangential component of the electric field is continuous across any interface: $\boldsymbol{n} \times (\boldsymbol{e}_2 - \boldsymbol{e}_1) = \boldsymbol{0}$.
As in [7], the boundary Γ of the magnetic domain is split into two distinct subsets Γ_e and Γ_h, on which boundary conditions are applied:

$$\boldsymbol{h} \times \boldsymbol{n} = \bar{\boldsymbol{h}} \times \boldsymbol{n} \quad \text{on } \Gamma_h, \tag{3.17}$$

$$\boldsymbol{e} \times \boldsymbol{n} = \bar{\boldsymbol{e}} \times \boldsymbol{n} \quad \text{on } \Gamma_e, \tag{3.18}$$

with $\bar{\boldsymbol{h}}$ and $\bar{\boldsymbol{e}}$ imposed fields. In the case of homogeneous boundary conditions, Eq. (3.18) implies

$$\boldsymbol{e} \times \boldsymbol{n} = \boldsymbol{0} \quad \text{on } \Gamma_e \quad \Rightarrow \quad \partial_t \boldsymbol{b} \cdot \boldsymbol{n} = 0 \quad \text{on } \Gamma_e \quad \Rightarrow \quad \boldsymbol{b} \cdot \boldsymbol{n} = 0 \quad \text{on } \Gamma_e, \tag{3.19}$$

in which last equation is obtained assuming the initial condition satisfies $\boldsymbol{b} \cdot \boldsymbol{n} = 0$ on Γ_e [7].
Next, two different formulations are described: the magnetic vector potential formulation and the magnetic field formulation, denoted respectively as the a-formulation and the h-ϕ-formulation. These are required for discretizing the problem in the context of the finite element method.

Vector potential formulation

From Eq. (3.1) and Eq. (3.4), one can define the magnetic vector potential $\boldsymbol{a}$ [Tm] and the electric scalar potential v [V], such that

$$\boldsymbol{b} = \nabla \times \boldsymbol{a} \tag{3.20}$$

$$\boldsymbol{e} = -\partial_t \boldsymbol{a} - \nabla v. \tag{3.21}$$

Note that v is only defined in Ω_c. As shown in [7], it is possible to define an auxiliary quantity such that $v^* = 0$ and

$$\boldsymbol{e} = -\partial_t \boldsymbol{a}^* \quad \text{in } \Omega_\mathrm{c}, \tag{3.22}$$

with $\boldsymbol{a}^*$ [Tm] the modified magnetic vector potential. The modified vector potential is adopted in this study and further, it is denoted by $\boldsymbol{a}^* = \boldsymbol{a}$. In that context, $\boldsymbol{a}$ is uniquely defined in Ω_c but it is not in $\Omega_\mathrm{c}^\mathrm{C}$, where a gauge condition is required for selecting one particular solution [21]. The gauging issue and its impact on the magnetic solution is addressed in Section 4.5.
The (modified) vector potential formulation relies on the following strong form:

$$\nabla \times (\nu \nabla \times \boldsymbol{a}) = \begin{cases} -\sigma \partial_t \boldsymbol{a}, & \text{in } \Omega_\mathrm{c}, \\ \boldsymbol{j}_\mathrm{s}, & \text{in } \Omega_\mathrm{s}, \\ \boldsymbol{0}, & \text{in } \Omega_\mathrm{c}^\mathrm{C} \backslash \Omega_\mathrm{s}, \end{cases} \tag{3.23}$$

which is based on Ampère's law. It simultaneously satisfies Eq. (3.9), Eq. (3.10), Eq. (3.13), Eq. (3.14), Eq. (3.20) and Eq. (3.22). A general representation of the different regions involved in Eq. (3.23) is shown in Fig. 3.1.

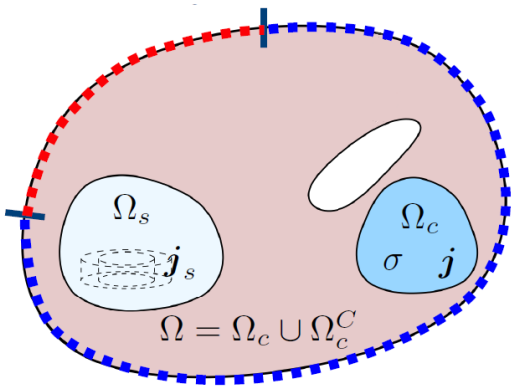

Figure 3.1: Abstract representation of Ω, $\Omega_\mathrm{c} \in \Omega$ and $\Omega_\mathrm{s} \in \Omega_\mathrm{c}^\mathrm{C}$, along with Γ_e (in red) and Γ_h (in blue). Figure adapted from [22].

The main unknown is the vector potential $\boldsymbol{a}$. Considering the fact that $\boldsymbol{a}$ is a primitive of $\boldsymbol{e}$ and $\boldsymbol{a}(t=0) = \boldsymbol{0}$ in this work, the boundary condition (Eq. (3.18)) reduces to an essential boundary condition $\boldsymbol{a} \times \boldsymbol{n} = \bar{\boldsymbol{a}} \times \boldsymbol{n}$ on Γ_e. The weak formulation is obtained by seeking $\boldsymbol{a} \in \mathcal{A}(\Omega)$, multiplying Eq. (3.23) by a test function $\boldsymbol{a}' \in \mathcal{A}_0(\Omega)$ and integrating over the volume Ω. Please refer to Appendix A.2 for the definition of function spaces $\mathcal{A}(\Omega)$ and $\mathcal{A}_0(\Omega)$. Adapting the a-formulation derived in [7] to the present study, the weak formulation reads:

$$\boxed{\begin{array}{c} \text{From a zero initial solution in } t = 0, \text{ find } \boldsymbol{a} \in \mathcal{A}(\Omega) \text{ such that, for } t > 0, \forall \boldsymbol{a}' \in \mathcal{A}_0(\Omega), \\ (\nu \, \nabla \times \boldsymbol{a}, \nabla \times \boldsymbol{a}')_\Omega - \langle \bar{\boldsymbol{h}} \times \boldsymbol{n}, \boldsymbol{a}' \rangle_{\Gamma_h} + (\sigma \, \partial_t \boldsymbol{a}, \boldsymbol{a}')_{\Omega_\mathrm{c}} = (\boldsymbol{j}_\mathrm{s}, \boldsymbol{a}')_{\Omega_\mathrm{s}}, \end{array}} \tag{3.24}$$

involving the inner product notations $(\cdot, \cdot)_\Omega$ and $\langle \cdot, \cdot \rangle_\Gamma$ defined in Appendix A.1. The essential boundary condition on Γ_e is strongly imposed through $\mathcal{A}(\Omega)$ while the natural boundary condition on Γ_h is weakly satisfied. The a-formulation is applied to the C400 geometry in Chapter 4.

Magnetic field formulation

Alternatively, the h-ϕ-formulation strong form relies on Faraday's law (Eq. (3.4)). Later in this work, the h-ϕ-formulation will be used for modelling the behaviour of a single superconducting filament. In that case, no source current density $\boldsymbol{j}_\mathrm{s}$ is considered and $\Omega_\mathrm{s} = \emptyset$. As mentioned in Section 3.3.4, the superconducting behaviour can be modelled using an equation of the form:

$$\boldsymbol{j} = \sigma(\boldsymbol{e})\boldsymbol{e} \quad \Longleftrightarrow \quad \boldsymbol{e} = \rho(\boldsymbol{j})\boldsymbol{j}, \tag{3.25}$$

in which ρ [Ωm] denotes the electrical resistivity.
As explained in Section 7.1, the superconductor filament will constitute the only conductor in the domain and therefore it can be denoted by Ω_c. The net current $\bar{I}_\mathrm{t}$ [A] flowing in Ω_c is imposed strongly by setting the circulation of $\boldsymbol{h}$ along a closed loop $\mathcal{C}$ around Ω_c to

$$\mathcal{I}(\boldsymbol{h}) = \oint_{\mathcal{C}} \boldsymbol{h} \cdot \boldsymbol{dl} = \bar{I}_\mathrm{t}, \tag{3.26}$$

with $\mathcal{I}(\boldsymbol{h})$ the functional of the net current through Ω_c given $\boldsymbol{h}$. It is the integral version of Ampère's law in the MQS approximation (Eq. (3.14)). The weak formulation is obtained by seeking the unknown $\boldsymbol{h}$ in $\mathcal{H}(\Omega)$, which takes the strong global condition of Eq. (3.26) into account. $\mathcal{H}(\Omega)$ is defined in Appendix A.2 alongside $\mathcal{H}_0(\Omega)$. Throughout this work, the magnetic field is equal to zero in $t = 0$. Introducing a test function $\boldsymbol{h}' \in \mathcal{H}_0(\Omega)$, the weak formulation can be adapted from [7]:

$$\boxed{\begin{array}{c}\text{From a zero initial solution in } t = 0, \text{ find } \boldsymbol{h} \in \mathcal{H}(\Omega) \text{ such that, for } t > 0, \forall \boldsymbol{h}' \in \mathcal{H}_0(\Omega), \\ (\mu\, \partial_t \boldsymbol{h}, \boldsymbol{h}')_\Omega + (\rho\, \nabla \times \boldsymbol{h}, \nabla \times \boldsymbol{h}')_{\Omega_\mathrm{c}} - \langle \bar{\boldsymbol{e}} \times \boldsymbol{n}, \boldsymbol{h}' \rangle_{\Gamma_e} = 0.\end{array}} \tag{3.27}$$

Please refer to [7] for the full derivation of the weak formulation. When applying an electric potential difference to the conductor, the right-hand-side of the weak formulation is not zero. Nevertheless, this situation is not encountered in this work.
The essential boundary condition on Γ_h is imposed through $\mathcal{H}(\Omega)$ while the natural boundary condition on Γ_e is weakly satisfied. In $\Omega_\mathrm{c}^\mathrm{C}$, $\boldsymbol{h}$ is curl-free: $\nabla \times \boldsymbol{h} = \boldsymbol{0}$. As a consequence, a scalar magnetic potential ϕ [A] can be introduced, such that

$$\boldsymbol{h} = -\nabla\phi. \tag{3.28}$$

Numerically, the curl-free property is ensured by decomposing $\boldsymbol{h}$ as a sum of gradients of nodal functions in $\Omega_\mathrm{c}^\mathrm{C}$ [7]. The h-ϕ-formulation is further adapted in Section 7.1 as it is used for modelling the behaviour of a superconducting filament.

Performance of both formulations

Dular [7] has shown that the a-formulation leads to better performance than the h-ϕ-formulation in geometries including ferromagnetic materials. This is linked to the concavity of the ferromagnetic constitutive law (cf. Section 3.2). Non-convergence of the Newton-Raphson linearization scheme can be observed in the case of the h-ϕ-formulation. Conversely, the strongly nonlinear constitutive law in type-II superconductors leads to better performance with the h-ϕ-formulation than with the a-formulation. This can also be explained by the shape of the power-law (cf. Section 3.3.4).
For systems that include both ferromagnetic and superconducting materials, Dular has proposed hybrid finite-element formulations that yield effective results [7].
In this work, the magnetic behaviour of the C400 at the macroscopic scale is modelled without taking the superconducting constitutive law into account, as explained in Chapter 4. In that case, the

a-formulation is preferred.
In Chapters 7 and 8, the local response of single superconducting filaments is assessed with a separated model. The filament-scale model does not involve any ferromagnetic material. The h-ϕ-formulation is thus preferred for modelling single filaments.

3.1.1 Magnetostatics case

In this work, some magnetostatic computations are also performed at the macroscopic scale of the whole cyclotron. In that case, the source current density $\boldsymbol{j}_\mathrm{s}$ is assumed constant in time. In practice, it corresponds to the nominal state of operation of the cyclotron. The magnetic field distribution is therefore constant and in particular, $\partial_t \boldsymbol{a} = \boldsymbol{0}$, which corresponds to the steady-state assumption. As a consequence, the a- formulation (Eq. (3.24)) simplifies to

$$\boxed{\begin{array}{c}\text{Find } \boldsymbol{a} \in \mathcal{A}(\Omega) \text{ such that, } \forall \boldsymbol{a}^{'} \in \mathcal{A}_0(\Omega), \\ (\nu \nabla \times \boldsymbol{a}, \nabla \times \boldsymbol{a}^{'})_\Omega - \langle \bar{\boldsymbol{h}} \times \boldsymbol{n}, \boldsymbol{a}^{'} \rangle_{\Gamma_h} = (\boldsymbol{j}_\mathrm{s}, \boldsymbol{a}^{'})_{\Omega_\mathrm{s}}.\end{array}} \tag{3.29}$$

As a reminder, the essential boundary condition (Eq. (3.18)) is strongly imposed through $\mathcal{A}(\boldsymbol{a})$. Note that in steady-state, there is no distinction between Ω_c and $\Omega_\mathrm{c}^\mathrm{C}$ and the gauge condition must be applied in the whole domain.

3.1.2 Magnetic energy

For the purpose of evaluating the convergence of a global quantity during a parametric study, the magnetic energy E_m [J] is introduced. It will be particularly useful for assessing the convergence of the results with respect to the global mesh size in Chapter 4. The magnetic energy density u_m [J/m^3] can be defined as

$$u_m(b) = \int_0^b h(b^*)\, db^* = \int_0^b \nu(b^*)\, b^*\, db^* = \begin{cases} b^2/2\mu, & \text{in } \Omega_\mathrm{L}, \\ \displaystyle\int_0^b \nu(b^*)\, b^*\, db^*, & \text{in } \Omega_\mathrm{NL}, \end{cases} \tag{3.30}$$

by anticipating on the next section and splitting the magnetic domain in its linear part Ω_L and its nonlinear part $\Omega_\mathrm{NL} = \Omega \backslash \Omega_\mathrm{L}$. In Ω_L, the reluctivity ν of the medium does not depend on b. The total magnetic energy can finally be computed as

$$E_m = \int_\Omega u_m \, d\Omega. \tag{3.31}$$

3.2 Ferromagnetic materials

The nonlinear magnetic domain is constituted by ferromagnetic materials as described in this section. In the context of the C400, the magnet yoke is made of iron, a ferromagnet.
Ferromagnetic materials exhibit a strong material response to an applied magnetic field and the b-h relation is not linear. In this work, the ferromagnetic yoke is considered isotropic, its permeability is scalar and the magnetic response is decomposed as

$$\boldsymbol{b} = \mu(\boldsymbol{h})\boldsymbol{h} = \mu_0(\boldsymbol{h} + \boldsymbol{m}(\boldsymbol{h})), \tag{3.32}$$

with $\boldsymbol{m}$ [A/m] the magnetization of the material, which depends on the magnetic field and can be large when dealing with ferromagnets. The magnetic response of the material is linked to microscopic *domains* that are spontaneously magnetized. Without an applied magnetic field, the microscopic magnetic moments are randomly arranged. When the applied field is increased, domain walls (boundaries between neighbouring domains) tend to move in such a way that the domains with magnetization parallel to the field are growing. When all magnetic dipoles are aligned with the applied field, the material enters the *saturation* regime [23] and $dm/dh = 0$. This theory is referred to as the Weiss theory.
Moreover, ferromagnetic materials exhibit an hysteretic behaviour. The first magnetization b-h curve of the ferromagnetic yoke has been measured by IBA and is shown in Fig. 3.2. In the context of the cyclotron ramp-up from zero to nominal current, working with the first magnetization curve seems adequate.

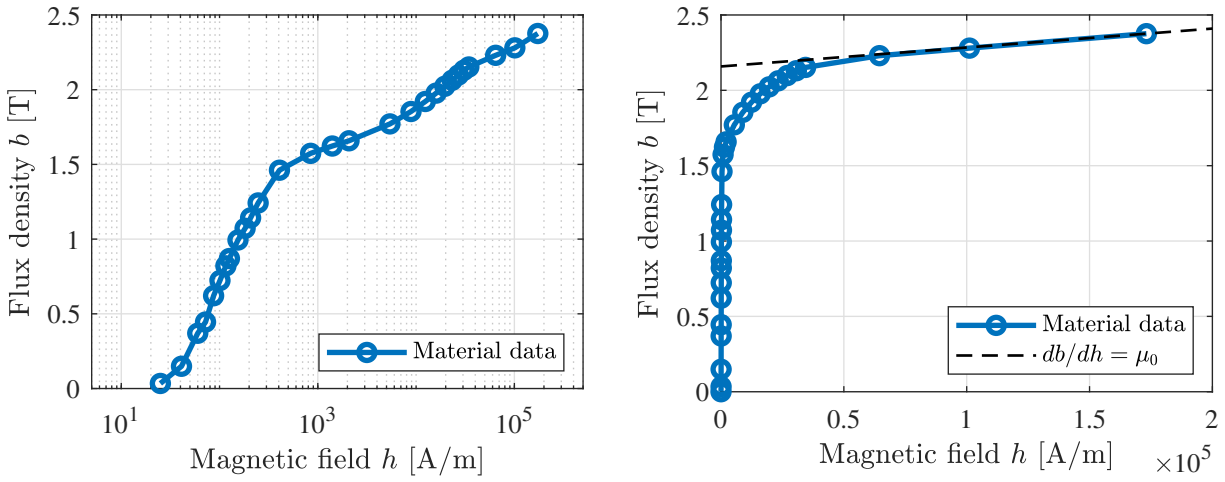

(a) (b)

Figure 3.2: Experimental flux density b - magnetic field h curve of the ferromagnetic yoke, (a) h in logarithmic scale, (b) in linear scale, along with the extrapolated saturated curve of slope $\mu_0 = 4\pi \times 10^{-7}$ H/m.

As can be observed, experimental data is only gathered for $b < 2.38$ T. However, as will be observed in Chapter 4, the flux density in the cyclotron can be larger than that. This issue has been solved by artificially adding new b-h points for larger b. As can be observed in Fig. 3.2(b), the experimental curve has reached the saturation regime as it matches the curve of linear slope μ_0 for $h > 10^5$ A/m. Consequently, new points (b_i, h_i) were generated starting from the last experimental point $(b_{\text{end}}, h_{\text{end}})$ as

$$b_i = \mu_0 \left(h_i - h_{\text{end}}\right) + b_{\text{end}}. \tag{3.33}$$

In the numerical implementation, points have been added until $b = 7$ T. Due to the intricate behaviour of the b-h curve at low field and in the medium range (Fig. 3.3(a)), no satisfying analytical

approximation has been obtained. Below $b_{\mathrm{T}} = 0.723$ T, the b-h curve exhibits a positive concavity $d^2b/dh^2 > 0$ as observed in Fig. 3.3(a), characteristic of the Rayleigh law [23]. In the rest of the curve, $d^2b/dh^2 < 0$ until the saturation regime is reached, for which yields $d^2b/dh^2 = 0$. As explained in Section 4.4, this inflexion point at $b = 0.723$ T has an impact on the stability of the linearization algorithms.

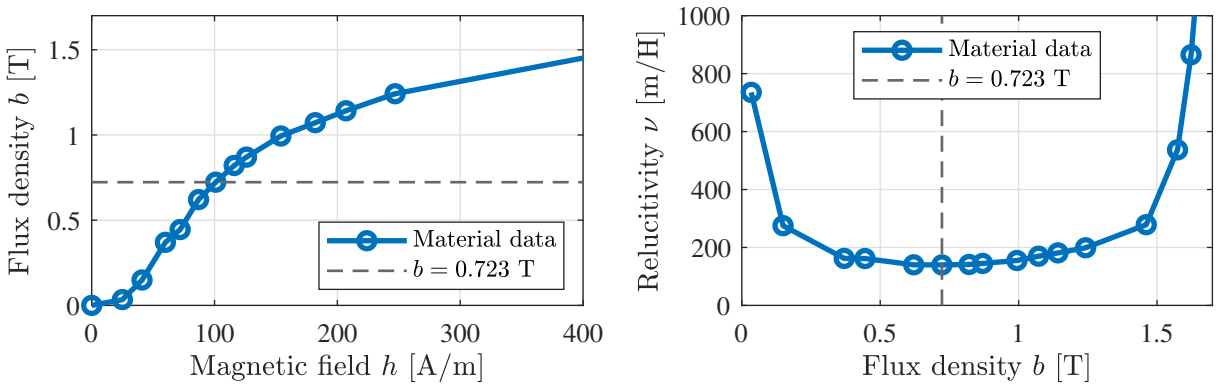

(a) (b)

Figure 3.3: (a) Experimental flux density b - magnetic field h curve of the ferromagnetic yoke and (b) reluctivity $\nu(b)$ curve, both in the low-medium field range ($b < 1.7$ T).

In Chapter 4, the cyclotron is modelled with the a-formulation (Eq. (3.24)). As a result, the reluctivity $\nu(b)$ of the yoke is required as a function of the flux density b. It is shown in Fig. 3.3(b) in the low field range. As can be observed, $d\nu/db < 0$ for $b = 0.723$ T, which will lead to numerical instabilities as described in Section 4.4. The minimal reluctivity is $\nu_{\mathrm{min}} = 140$ m/H, corresponding to a relative permeability of $\mu_{r,\mathrm{max}} = 5700$.
Numerically, the b-h curve is reconstructed directly from material data and a spline interpolation is performed in GetDP to retrieve the reluctivity $\nu(b)$ for any input flux density $b > 0$. The corresponding magnetic field is then retrieved with Eq. (3.9). For the first input point $(b_1, h_1) = (0, 0)$, the reluctivity $\nu_1 = h_1/b_1$ is not defined. It is linearly extrapolated from the second and third data points:

$$\nu(b = 0) = \nu_1 \approx \nu_2 - \frac{\nu_3 - \nu_2}{b_3 - b_2} b_2 = 871 \text{ m/H}. \tag{3.34}$$

The computation of the local magnetic energy density as a function of the flux density in the yoke $u_m(b)$ (Eq. (3.30)) is performed beforehand and tabulated, it is then passed as an input to the GetDP solver. Later in this work, the Jacobian matrix element $\partial h_i/\partial b_j$ is required for the Newton-Raphson linearization scheme. Based on the isotropic assumption, it comes successively, in index notation:

$$h_i = \nu(b) b_i \quad \Rightarrow \quad \frac{\partial h_i}{\partial b_j} = \nu(b) \frac{\partial b_i}{\partial b_j} + \frac{\partial \nu}{\partial b^2} \frac{\partial b^2}{\partial b_j} b_i = \nu(b) \delta_{ij} + \frac{\partial \nu}{\partial b^2} 2 b_j b_i. \tag{3.35}$$

3.3 Superconducting materials

The coil of the C400 cyclotron is made of Nb-Ti, a superconducting material. In this section, superconductors are first described theoretically. A more practical discussion of applied superconductors is also provided. Finally, different models encountered during the study are presented.

Below their critical temperature T_{c} [K], superconductors exhibit the unique property of having an extremely low DC resistance that cannot be measured. For mercury, it was discovered by Kamerlingh-Onnes in 1911. In 1933, the Meissner effect was observed experimentally, still for mercucy: a super-

conducting piece expels an externally applied magnetic flux [2]. At the microscopic scale, the current is carried by Cooper pairs formed by two paired electrons. Apart from its critical temperature, a superconductor can carry a maximal current density, the critical current density $\boldsymbol{j}_c$ [A/m^2]. Similarly, superconductivity occurs below some threshold magnetic field, the critical magnetic field $\boldsymbol{h}_c$ [A/m]. Together, the critical quantities form a critical surface [2], as shown in Fig. 3.4. A superconductor is in the superconducting state if it lies below the critical surface in the (j-b-T)-space. Above, it is considered as a normal conductor. In the normal conducting state, the material is usually much more resistive than copper [25].

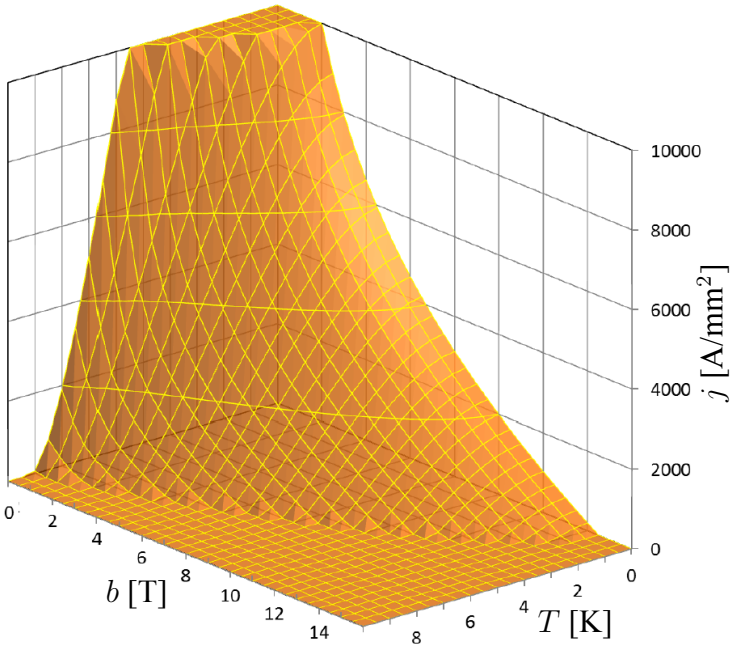

Figure 3.4: Critical surface of Nb-Ti in the (j-b-T)-space. Figure adapted from [24].

A distinction must be made between type-I and type-II superconductors. In type-I superconductors, the magnetic flux cannot enter the material, except on a small thickness λ [m], the penetration depth. The superconductor is said to be in the *Meissner state*, which is described by the first and the second London equations [2]. Type-I superconductors are not exploited much in practical applications, as their critical field is low ($\mu_0 h_c \lesssim 0.1$ T) and the current is only flowing on a thickness λ in the Meissner state.

In the C400 coil, Nb-Ti is preferred for working at larger fields. The niobium titanium alloy is a type-II superconductor. Type-II superconductors exhibit an intermediate state which is called the *mixed state*, in which magnetic flux enters the material in the form of quantum fluxoids, also called *vortices*. The (h-T) phase diagram of a typical type-II material is shown in Fig. 3.5. As observed, type-II materials are characterized by three possible states, depending on the applied magnetic field h_a [A/m]:

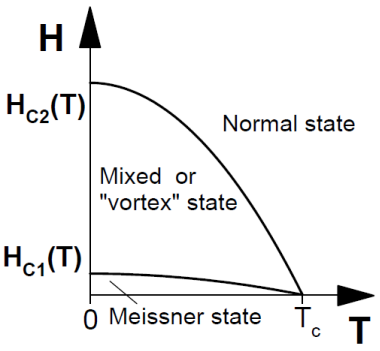

Figure 3.5: Critical surface of a type-II superconductor in the $j = 0$ plane. Figure adapted from [25].

- below $h_{c,1}$: Meissner state, no flux density inside the superconductor.
- between $h_{c,1}$ and $h_{c,2}$: mixed state, mean flux density inside the superconductor between 0 and $\mu_0 h_a$.
- above $h_{c,2}$: resistive, normal conducting state.

Note that Fig. 3.5 is not to scale: the lower critical field $\mu_0 h_{c,1} \sim 0.01$ T is much lower than the upper critical field, that can reach $\mu_0 h_{c,2} \sim 100$ T for type-II superconductors [25]. Furthermore, the Meissner state is neglected in this work.

Type-II superconductors can be subdivided into two categories. First, the low-temperature superconductors (LTS), like Nb-Ti and Nb_3Sn, have a critical temperature T_c around 9 K and 18 K, respectively [2]. Second, the high-temperature superconductors (HTS) are capable of reaching much higher temperatures while remaining in the mixed state. The most common LTS are Nb-Ti and

Nb_3Sn. Even though Nb_3Sn has a larger critical current density, Nb-Ti is often preferred as it is ductile [24]. Nb_3Sn is much more brittle and it is limited to higher field applications [26], for which Nb-Ti cannot be used. In section 3.3.1, the focus is set on the manufacturing of LTS in the form of wires and filaments. Conversely, HTS are usually manufactured as tapes. Section 3.3.1 describes the engineering view of processing Nb-Ti in the context of the C400 superconducting coil.

3.3.1 Practical considerations

When Nb-Ti crosses the critical surface represented in Fig. 3.4, it goes from the superconducting state to the normal conducting state. As a result, its resistivity suddenly increases and the corresponding Joule losses can lead to an enormous heat dissipation. Such an event is called a *quench* [3], it is sketched in Fig. 3.6. To ensure the superconductor does not break down when suffering a quench, multiple superconducting filaments are embedded in parallel in a normal conducting *matrix*, also called the stabilizer, usually made of copper. During a quench, copper can transport current to adjacent filaments while diffusing the heat generated at the local quench event [27]. The purpose of the copper matrix is to protect and to stabilize Nb-Ti. Indeed, working with fine Nb-Ti filaments embedded in copper also reduces transient losses and flux jumps in the superconductor, as well as field distortions [3]. Transient losses and field distortions are linked to the permanent magnetization of filaments, which can be reduced by decreasing the filament diameter [8]. In practice, the filaments are twisted to reduce losses in the matrix [27]. The particular issue of losses in the superconducting coil is described later in Section 3.5. A group of twisted filaments is called a *strand*. Finally, a superconducting cable is made of several strands. Please note that the term *superconducting cable* refers to a composite assembly of Nb-Ti in copper.

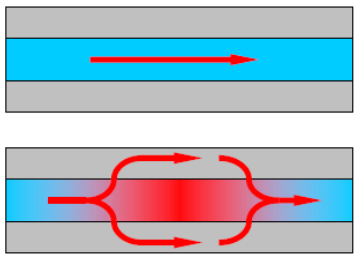

Figure 3.6: Quenching event (red zone) of a superconductor (in blue) in a normal conducting matrix (in grey). The current is in red. Figure adapted from [24].

Many different cable configurations exist, depending among other parameters on the distribution of strands, the type of the stabilizer and the superconductor to matrix ratio. The C400 coil relies on the wire-in-channel (WIC) technology, in which a composite core wire is embedded inside a copper channel as represented in Fig. 3.6.

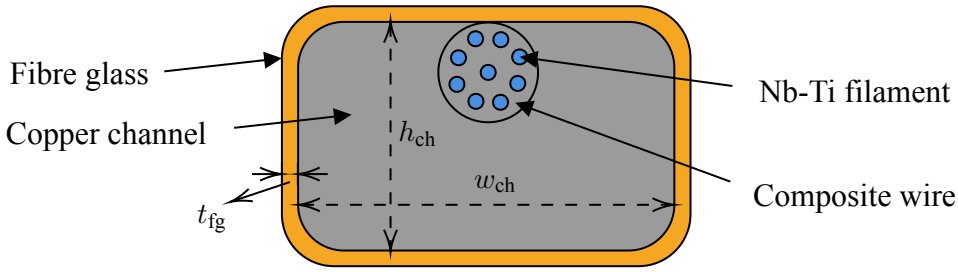

Figure 3.7: Sketch of the cross-section of a wire-in-channel superconducting cable. In orange, insulating fibre glass. In grey, copper. In blue, Nb-Ti filaments. Note that the figure is not to scale: filaments are much smaller and more closely manufactured than what is represented.

The diameter of the filaments is expected to be $d_f = 51$ µm. The number of filaments per conductor is denoted by N_f [-]. The height and the width of the channel are respectively denoted by h_{ch} [m] and width w_{ch} [m], while the thickness of the fibre glass insulation is denoted by t_{fg} [m]. One particular quantity of interest is the Nb-Ti filling factor of the cable, λ_{SC} [-]. It is defined as the ratio

of the total cross-section of the Nb-Ti filaments to the cross-section of the cable, it thus represents the volumic fraction of Nb-Ti inside the cable. It has been computed from data provided by the manufacturer:

$$\lambda_{\text{SC}} = 0.03. \tag{3.36}$$

It is required for determining losses in the coil as explained in Section 3.5. Similarly, the local Nb-Ti factor inside the composite core wire λ_{w} [-] can be retrieved from the copper-to-superconductor ratio of 1.4 in the wire:

$$\lambda_{\text{w}} = \frac{1}{1+1.4} = 0.42. \tag{3.37}$$

During operation, the current is expected to be carried almost exclusively by Nb-Ti. The local current density $\boldsymbol{j}_{\text{SC}}$ [A/m^2] in Nb-Ti is linked to the engineering current density $\boldsymbol{j}_{\text{eng}}$ [A/m^2] through:

$$\boldsymbol{j}_{\text{eng}} = \lambda_{\text{SC}}\, \boldsymbol{j}_{\text{SC}}. \tag{3.38}$$

The engineering current density is mentioned when looking at the conductor from a global point of view, without focusing on its internal structure.
The residual resistivity ratio (RRR) of copper is defined as the ratio between electrical resistivity at room temperature and the resistivity at cryogenic temperature [27]. It is an image of copper purity [20]. The expected RRR of copper in the composite conductor is 80.

3.3.2 Critical surface of Nb-Ti

For modelling superconductors, the critical current density j_{c} is required. As can be observed in the critical surface diagram of Nb-Ti (Fig. 3.4), it depends on the applied flux density and on temperature. More precisely, the critical current decreases as both the applied magnetic field and the temperature increase. In this section, the critical current j_{c} dependence on b and T is discussed.

While the critical temperature T_{c} and the critical field $h_{\text{c},2}$ of a superconductor depends on the material itself, the critical current j_{c} depends on its microstructure [2]. Physically, the critical current density is linked to the *Lorentz-like* force $\boldsymbol{f}_{\text{L}} = \boldsymbol{j} \times \boldsymbol{b}$, in [N/m^3], locally acting on flux vortices inside type-II superconductors [28]. The Lorentz-like forces tend to set the vortices in motion. The motion of vortices then leads to a flux variation, induced currents and losses in the normal-conducting core of the vortices. This is referred to as *flux flow* [25]. To counterbalance the Lorentz-like force, *pinning centers*, defects in irreversible superconductors, trap vortices by exerting a *pinning force* $\boldsymbol{f}_{\text{P}}$ [N/m^3] on them. If the pinning force overcomes the Lorentz-like force, there is no flux motion and no losses. On the opposite, if the Lorentz-like force is larger:

$$f_{\text{L}} = \|\boldsymbol{j} \times \boldsymbol{b}\| > f_{\text{P}}, \tag{3.39}$$

flux flow occurs. The critical current density or depinning current density can be retrieved by balancing Eq. (3.39).

One popular model for the critical current density dependence on flux density is Kim's law, first proposed in 1962 [29]:

$$j_{\text{c}}(b) = \frac{j_{\text{c},0}}{1 + b/b_0}, \tag{3.40}$$

in which $j_{\text{c},0}$ [A/m^2] and b_0 [T] are reference quantities. As Nb-Ti has been widely used since, many measurements are now available and more recently, Bottura [30] has proposed a specific *practical fit for the critical surface of Nb-Ti*. It is in good agreement with the description based on

the pinning force (Eq. (3.39)). It allows to retrieve the critical current as a function of flux density and temperature:

$$j_{\mathrm{c}}(b,T) = \frac{C_0}{b}\left(\frac{b}{b_{\mathrm{c},2}(T)}\right)^{\alpha_{\text{Nb-Ti}}}\left(1-\frac{b}{b_{\mathrm{c},2}(T)}\right)^{\beta_{\text{Nb-Ti}}}\left(1-\left(\frac{T}{T_{\mathrm{c},0}}\right)^{1.7}\right)^{\gamma_{\text{Nb-Ti}}}, \tag{3.41}$$

in which $\alpha_{\text{Nb-Ti}}$ [-], $\beta_{\text{Nb-Ti}}$ [-], $\gamma_{\text{Nb-Ti}}$ [-] are global fitting parameters, $T_{\mathrm{c},0} = 9.2$ K is the critical temperature at zero field and zero current and C_0 [T A/m^2] is a normalization constant depending on the particular sample. The Nb-Ti critical field dependence on temperature has been studied by Lubell [31], reading:

$$b_{\mathrm{c},2}(T) = b_{\mathrm{c},20}\left(1-\left(\frac{T}{T_{\mathrm{c},0}}\right)^{1.7}\right), \tag{3.42}$$

with $b_{\mathrm{c},20} = 14.5$ T the upper critical field at 0 K. As highlighted by experimental results on Nb-Ti strands in [32], Bottura's relationship is fairly consistent with both magnetization data at low field and transport current measurements at high field. Moreover, it has been used many times, including in the design of the superconducting magnet of the International Thermonuclear Experimental Reactor (ITER) tokamak [33]. In the present work, Bottura's relationship (Eq. (3.41)) is also used for describing the Nb-Ti critical surface.

In his paper [30], Bottura fitted his curve on several data sets. The data set corresponding the most to the present study is the Spencer data set [34], which relates to a field range from 0 T to 8 T and temperatures from 4.2 K to 9 K. In that case, Bottura obtained the following fitting parameters:

$$\alpha_{\text{Nb-Ti}} = 0.57, \quad \beta_{\text{Nb-Ti}} = 0.9, \quad \gamma_{\text{Nb-Ti}} = 1.9. \tag{3.43}$$

The normalization constant C_0 remains to be determined. Ideally, measurements should be performed on the C400 coil to provide an accurate estimation. The manufacturer of the coil provided one single critical current value, from which the constant C_0 is retrieved, assuming the current only flows in the Nb-Ti filaments:

$$I_{\mathrm{c}}(4.5\text{ T}, 4.2\text{ K}) = 2850\text{ A} \quad \Rightarrow \quad j_{\mathrm{c}}(4.5\text{ T}, 4.2\text{ K}) = 3142\text{ A/mm}^2 \tag{3.44}$$

$$\Rightarrow \quad C_0 = 6.773\times10^{10}\text{ T A/m}^2. \tag{3.45}$$

The final $j_{\mathrm{c}}(b,T)$ variation with respect to T and b implemented in the numerical model is represented in Fig. 3.8. As observed in the left graph, the critical current density decreases as temperature increases. As the flux density increases, the maximal current-sharing temperature, the maximal temperature for which Nb-Ti is superconducting, decreases. The order of magnitude is consistent with the experimental results obtained by Boutboul *et al.* [32]. For several strands from the Large Hadron Collider (LHC), they measured $j_{\mathrm{c}}(6\text{ T}, 4.2\text{ K})$ in the range $2278 \sim 2344$ A/mm^2. The fitting used in the present study yields $j_{\mathrm{c}}(6\text{ T}, 4.2\text{ K}) = 2162$ A/mm^2. The slight difference could be explained by the difference in filament diameter ($d_f = 51$ µm for the C400, against 6 µm in [32]) and the fact that j_{c} is expected to decrease when the filament diameter is increased [28].

As represented in Fig. 3.8(b), the critical current density increases as the flux density is reduced. In particular, it tends towards infinity as the flux density tends towards zero. Equation (3.41) diverges for $b = 0$ T. After having discussed the matter with Luca Bottura, the divergence itself has no physical meaning, as in practice the $b = 0$ T condition is never met for a filament in which transport current is flowing. It is at least subjected to its self-field: $0.01 - 0.1$ T. One solution to avoid this divergence is to measure the maximal critical current density $j_{\mathrm{c,self}}$ due to self-field and use an effective critical current density[1] as

$$j_{\mathrm{c,eff}} = \left(\frac{1}{j_{\mathrm{c}}} + \frac{1}{j_{\mathrm{c,self}}}\right)^{-1}, \tag{3.46}$$

[1] Private communication with Luca Bottura, 11/05/2023.

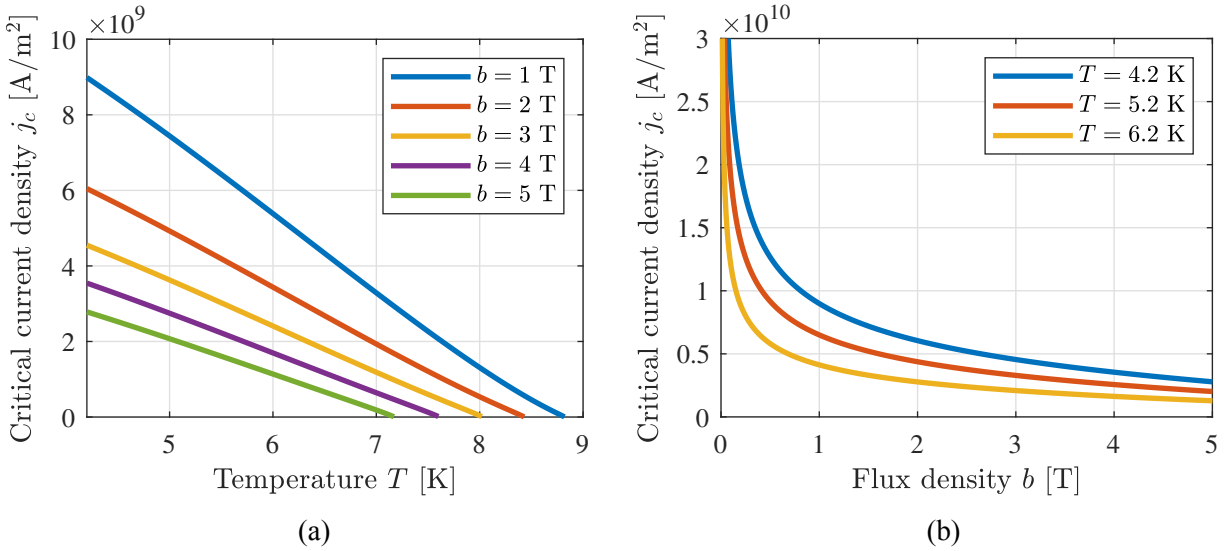

Figure 3.8: Critical current density j_c of Nb-Ti filaments in the C400 coil dependence on (a) temperature T, (b) flux density b, according to Bottura's relationship (Eq. (3.41)).

with j_c computed using Eq. (3.41).
However, when dealing with hysteresis losses in Nb-Ti filaments, the divergence of j_c at zero field is not a problem, as shown later in this work. Moreover, as the value of $j_{c,self}$ is not known, Eq. (3.41) is simply implemented and used in the next chapters. Numerically, Eq. (3.41) has been regularized by implementing it as $j_c(\max(b;\varepsilon_b),T)$ with $\varepsilon_b = 10^{-6}$ T.

3.3.3 Critical state model

In this section and in the following section, models for the $\boldsymbol{j}$-$\boldsymbol{e}$ constitutive law of superconductors are presented. The most popular model for describing the behaviour of superconductors has been introduced by Bean [35] in 1962: the *critical state model* (CSM) also referred to as Bean's model. It is valid for irreversible or hard superconductors, in which the pinning forces are strong. It assumes $h_{c,1} \to 0$ and $h_{c,2} \to \infty$, i.e. the type-II superconductor is always in the mixed state. It also assumes the dimensions are larger than the penetration depth λ [25]. In the present study, considering Nb-Ti filaments ($d_f \gg \lambda \sim 0.1$ µm [2]), these assumptions seem reasonable.
The CSM states that the norm of the current density j inside superconductors is either 0 or j_c. It is only zero in regions where the electric field has always been zero. For any finite value of the electric field $e > 0$, the current density is parallel to the electric field. When the electric field is reduced to zero, the direction of the current density remains the same as the electric field just before it vanished. Consequently, the superconducting material exhibits *hysteresis* [8]. An example of such an hysteretic behaviour is represented in Fig. 3.9, for an infinite slab.
In Section 3.5, a constant critical current density j_c is assumed for deriving analytical approximations for losses based on the CSM. These results are then extrapolated to the $j_c(b,T)$ case in the numerical implementation at the macroscopic scale. Nevertheless, the CSM is a simplified model and does not always represent reality. In practice, such a discontinuous $\boldsymbol{j}$-$\boldsymbol{e}$ constitutive law is not observed experimentally. As discussed in the following section, the discontinuity is smoothed out by the *flux creep* phenomenon.

3.3.4 Power-law model

Many experimental observations, e.g. [36], have illustrated a strongly nonlinear, yet continuous voltage-current characteristic in superconducting filaments. This behaviour can be explained by

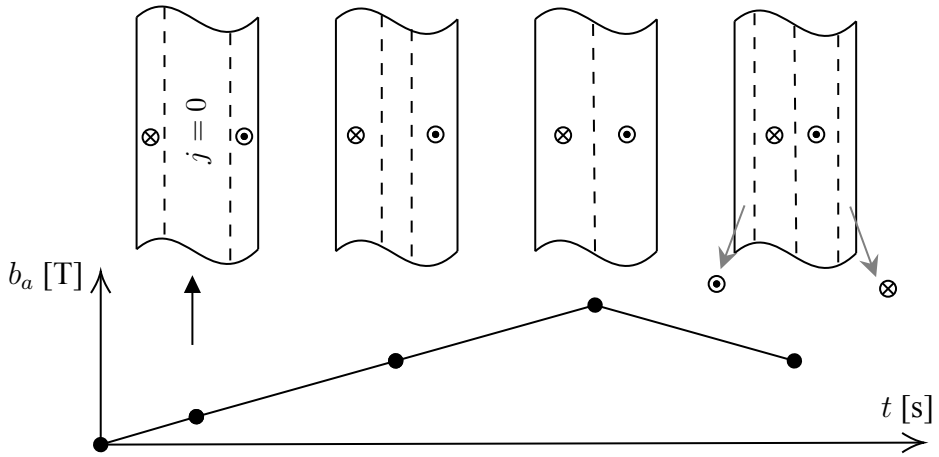

Figure 3.9: Evolution of the induced currents (at the top) in an infinite slab as a function of the external applied flux density b_a varying in time as shown in the bottom, according to the CSM. $\odot$ represents an out-of-plane current density of norm j_c, $\otimes$ in-plane.

the so-called *power-law* model:

$$\boldsymbol{e} = \frac{e_c}{j_c}\left(\frac{j}{j_c}\right)^{n-1}\boldsymbol{j} = \rho(j)\boldsymbol{j} \quad \Longleftrightarrow \quad \boldsymbol{j} = \frac{j_c}{e_c}\left(\frac{e}{e_c}\right)^{(1-n)/n}\boldsymbol{e} = \sigma(e)\boldsymbol{e}, \tag{3.47}$$

with e_c [V/m] a threshold electric field, usually chosen as $e_c = 10^{-4}$ V/m, and the n-exponent characterising the steepness of the transition [37]. Physically, it is linked to the *flux creep* phenomenon: due to thermal excitation, some vortices leave their pinning centers even for $j < j_c$, resulting in a finite resistivity and a non-vanishing electric field. The n-exponent is linked to the activation energy U_a [J] of the pinning potential well through $n = U_a/k_B T$, with $k_B = 1.38 \times 10^{-23}$ J/K the Boltzmann constant [38]. The CSM model is recovered in the asymptotic regime ($n \to \infty$) of Eq. (3.47). Strictly speaking, this model is valid until the material enters the flux flow regime [37]. The flux flow regime is neglected in the present study.
For Nb-Ti at 4.2 K, the n-exponent lies in the range $20 - 60$, n decreasing when the flux density b is increased [39]. Even though [39] provides extensive data for the n-exponent, no analytical approximation is obtained for the $n(b)$ relationship. Moreover, the n-exponent is expected to decrease as T is increased: in the limit $T > T_c$, $n \to 1$ and Ohm's law is recovered as the material is in the normal conducting state [25].
Numerically, the power-law is implemented at the filament scale, for which the h-ϕ formulation (Eq. (3.27)) is used. The nonlinear equation requires a numerical linearization scheme, based on the Jacobian matrix of Eq. (3.47). From [7], it reads using index notation:

$$\frac{\partial e_i}{\partial j_j} = \rho(j)\delta_{ij} + (n-1)\frac{\rho(j)}{j^2} j_i j_j. \tag{3.48}$$

3.4 Thermodynamics

In this study, the focus is set on the thermal study of the coil of the C400 cyclotron. The main unknown is the temperature distribution T [K] inside the coil. The liquid helium bath temperature is assumed to be at a temperature $T_{He} = 4.2$ K. The temperature distribution inside the helium flow will not be computed, as it would require to solve for the whole set of Navier-Stokes equations [40]. Thus, we will focus on the heat conduction process inside the C400 coil and liquid helium will be modelled as a convective boundary condition.

Conduction in a solid is dictated by the heat diffusion equation:

$$-\nabla \cdot \boldsymbol{q}'' + q_\text{s} = \rho_V c_p \partial_t T, \tag{3.49}$$

with $\boldsymbol{q}''$ [W/m^2] the heat flux, q_s [W/m^3] the volumetric heat source, ρ_V [kg/m^3] the density of the material and c_p [J/(kg K)] its specific heat [40]. Physically, it corresponds to the local thermal energy balance. The heat flux is generally described by Fourier's law:

$$\boldsymbol{q}'' = -\boldsymbol{\kappa} \cdot \nabla T, \tag{3.50}$$

with $\boldsymbol{\kappa}$ [W/(m K)] the thermal conductivity tensor of the material. In the most general way, $\boldsymbol{\kappa}$ is written as a tensor to allow for modelling anisotropic behaviour [40].
Before diving into the derivation of the thermal weak formulation, the expressions of the internal energy U [J] in a fixed volume Ω and its variation $\dot{U}$ [W] are recalled:

$$U = \int_\Omega \rho c_p T \, d\Omega \quad \Rightarrow \quad \dot{U} = \int_\Omega \rho c_p \partial_t T \, d\Omega. \tag{3.51}$$

Similarly, Eq. (3.49) simplifies to the global thermal energy balance equation when integrated:

$$\int_\Omega q_\text{s} \, d\Omega = \int_\Gamma \boldsymbol{q}'' \cdot \boldsymbol{n} \, d\Gamma + \dot{U} \quad \Leftrightarrow \quad Q_\text{s} = Q_\text{out} + \dot{U}, \tag{3.52}$$

with $\Gamma = \partial\Omega$, Q_s [W] the heat generation rate and Q_out [W] the net exchanged heat rate, counted positive if the heat is going from the volume Ω to its surroundings.

3.4.1 Thermal weak formulation

In this section, the thermal weak formulation is derived in its most general context. The goal is to provide a framework for future works, as Dular [7] did for magnetodynamic formulations.

Let us consider a fixed domain Ω_th with regular boundary Γ_th. Multiple boundary conditions are considered on different subsets of Γ_th:

- Dirichlet boundary conditions: the temperature $T = \bar{T}$ is imposed on Γ_th^D.
- Neumann boundary conditions: the heat flux $\boldsymbol{q}'' \cdot \boldsymbol{n} = \bar{\boldsymbol{q}}'' \cdot \boldsymbol{n}$ is imposed on Γ_th^N. The adiabatic boundary condition $\bar{\boldsymbol{q}}'' \cdot \boldsymbol{n} = 0$ corresponds to an homogeneous Neumann boundary conditions.
- Robin boundary conditions: the heat flux $\boldsymbol{q}'' \cdot \boldsymbol{n} = \bar{f}(T)$ is imposed as a function of temperature on Γ_th^R. Two particular cases are of interest:
  - Convective boundary condition: $\boldsymbol{q}'' \cdot \boldsymbol{n} = h(T - T_\infty)$, with h [W/m^2 K] the convective heat transfer coefficient and T_∞ [K] the bulk temperature of the fluid involved in the heat transfer process [40].
  - Radiative boundary condition: $\boldsymbol{q}'' \cdot \boldsymbol{n} = \varepsilon_R \sigma_R (T^4 - T_\text{sur}^4)$, with ε_R [-] the surface radiative emissivity, $\sigma_R = 5.67 \times 10^{-8}$ [W/m^2 K^4] the Stefan-Boltzmann constant and T_sur [K] the surroundings temperature [40].

The subsets Γ_{th}^D, Γ_{th}^N and Γ_{th}^R are assumed distinct and complementary subsets of Γ_{th}. In the proposed weak formulation, only Dirichlet boundary conditions are strongly imposed. They are thus referred to as essential boundary conditions. The weak formulation is obtained by seeking the temperature $T \in \mathcal{T}(\Omega_{\text{th}})$, multiplying Eq. (3.49) by some test function $T' \in \mathcal{T}_0(\Omega_{\text{th}})$ and integrating over the volume Ω_{th}. Spaces $\mathcal{T}(\Omega_{\text{th}})$ and $\mathcal{T}_0(\Omega_{\text{th}})$ are defined in Appendix A.2. The thermal weak formulation reads:

$$\boxed{\begin{array}{l}\text{From an initial solution in } t=0, \text{ find } T \in \mathcal{T}(\Omega_{\text{th}}) \text{ such that, for } t>0, \forall T' \in \mathcal{T}_0(\Omega_{\text{th}}),\\ (\rho_V c_p\, \partial_t T, T')_{\Omega_{\text{th}}} + (\boldsymbol{\kappa}\cdot\nabla T, \nabla T')_{\Omega_{\text{th}}} + \langle \bar{\boldsymbol{q}}'' \cdot \boldsymbol{n}, T' \rangle_{\Gamma_{\text{th}}^N} + \langle \bar{f}(T), T' \rangle_{\Gamma_{\text{th}}^R} = (q_{\text{s}}, T')_{\Omega_{\text{th}}}.\end{array}} \tag{3.53}$$

The full derivation of the thermal integral equation can be found in Appendix A.3. Neumann and Robin boundary conditions are weakly imposed, corresponding to natural boundary conditions.
The proposed thermal weak formulation is validated and adapted to the C400 coil geometry in Chapter 5.

3.5 Magnetothermal coupling mechanisms

Now that the magnetodynamics and the thermal physics have been discussed, let us focus on the coupling mechanisms linking the two physics. As will be shown, the time variation of the flux density in the superconducting coil will induce losses through heat dissipation. In this section, analytical approximations for volumetric losses are presented. In the coupled magnetothermal model, these losses correspond to the source term in the heat diffusion equation discussed above.
In the most general way, the volumetric losses q [W/m^3] can be computed as

$$q = \boldsymbol{j} \cdot \boldsymbol{e}, \tag{3.54}$$

which is valid both in normal conductors and in superconductors. First, Joule losses in normal conductors are discussed. Later, the focus is set on losses in superconducting cables. These have been extensively studied in the literature. The present work mainly relies on the principles detailed by Carr [8], Verweij [27] and Wilson [3, 41]. In superconducting cables, losses mainly occur through two particular mechanisms: filament hysteresis losses and inter-filament coupling losses [27, 41]. Longitudinal Joule losses in the copper matrix are neglected as the longitudinal current is mainly carried by the Nb-Ti filaments, much less resistive than the copper matrix.

3.5.1 Joule losses

Losses in normal conductors are often referred to as *Joule losses*. In the present study, it refers to the stainless steel helium vessel and the iron yoke. As Ohm's law (Eq. (3.10)) is valid in normal conductors, the ohmic heat dissipation q_{j} [W/m^3] is simply $q_{\text{j}} = \sigma \boldsymbol{e} \cdot \boldsymbol{e} = \sigma e^2$. Using the a-formulation presented in Section 3.1, it reduces to

$$q_{\text{j}} = \sigma e^2 = \sigma \|\partial_t \boldsymbol{a}\|^2, \tag{3.55}$$

which is valid in the conducting domain Ω_{c}. While the ferromagnetic yoke is assumed at room temperature, the temperature dependence of σ in the helium vessel is taken into account numerically.

3.5.2 Hysteresis losses in Nb-Ti filaments

The focus is now set on filament hysteresis losses, also called *AC losses*. In type-II superconductors in the mixed state, flux vortices can enter the material when the external magnetic field is increased.

Persisting currents are generated in order to prevent the flux density from fully penetrating the material. The motion of flux vortices and the corresponding flux density variation ($d\boldsymbol{b}/dt \neq \mathbf{0}$) induces an electric field through Faraday's law (Eq. (3.4)). Together, the currents and the induced electric field lead to local losses through Eq. (3.54). In the CSM and considering a cyclic external field applied to the superconductor, Carr [8] and Wilson [3] have shown that the losses per cycle are independent of the cycle speed in the case of an infinite cylinder and proportional to the area enclosed by the cyclic magnetization curve of the superconductor. For these reasons, the losses corresponding to persistent magnetization currents are usually referred to as *hysteresis losses*. In this section, different types of configurations are investigated and the corresponding losses are discussed.

As the longitudinal radius of curvature of filaments (diameter $d_f = 51$ µm) is in the range of meters, filaments can be approximated as infinite superconducting cylinders. Despite the composite cable being composed of multiple filaments and the field pattern between closely arranged filaments potentially being complex, the field perturbations caused by neighbouring turns will generally cancel each other out, resulting in a loss equivalent to that of an isolated cylinder [3]. Also, the magnetic field is mostly perpendicular to the filament axis and the focus is set on the transverse field loss. In this work, approximations for the hysteresis loss $q_{\text{hys,1}}$ [W/m^3] in one single filament are adapted from Carr [8]. The most common method of extrapolating filament losses to macroscopic hysteresis losses is presented in Wilson's book [3]. Taking the Nb-Ti filling factor λ_{SC} into account, the macroscopic hysteresis losses per unit volume q_{hys} [W/m^3] are retrieved as

$$q_{\text{hys}} = \lambda_{\text{SC}}\ q_{\text{hys,1}}. \tag{3.56}$$

Physically, this method distributes the filament hysteresis loss over the whole volume of the composite conductor. It is adequate when the thermal problem is solved at a scale larger than the one of a single filament, which is the case in this study.

Carr focuses on AC applied fields and on the corresponding losses per cycle (in [J/m^3]), as Wilson in [3, 41] and Verweij in [27]. However, the present study requires the instantaneous power loss per unit volume q_{hys} (in [W/m^3]), which is why the different developments from [8] are adapted here. Carr's results are based on the CSM (Section 3.3.3). In the following section, the hysteresis loss is computed as an average over the volume of one filament:

$$q_{\text{hys,1}} = \frac{4}{\pi d_f^2} \int_0^{d_f/2} \int_0^{2\pi} \boldsymbol{j} \cdot \boldsymbol{e}\ r\ dr\ d\theta. \tag{3.57}$$

Transverse field variation

In this section, the direction of the applied field is assumed constant in time.
Assuming no transport current, an uniform external magnetic field and a constant critical current density $\partial j_{\text{c}}/\partial b = 0$, Carr distinguishes two cases. The validity of these assumptions is discussed in Chapter 7 when compared to losses computed from a filament model. The $\partial j_{\text{c}}/\partial b = 0$ assumption is relaxed at the end of the section. Introducing the penetration flux density

$$b_p = \frac{\mu_0\ j_{\text{c}}\ d_f}{\pi}, \tag{3.58}$$

and the applied flux density b_a (the source of the applied flux density is considered at a scale much larger than the filament dimensions, such that the filament magnetization has no impact on the macroscopic flux density and $b_a = \mu_0\ h_a$), the distinction is made between:

- the weakly penetrated filament: $b_a \ll b_p$, for which the current density distribution is shown in the left part of Fig. 3.10,

- the fully penetrated filament: $b_a \geq b_p$, in the right part of Fig. 3.10.

There is no analytical approximation in the intermediate regime ($b_a \lesssim b_p$).
In full penetration, the magnetization of the filament is constant and the induced electric field along the filament axis is $e_z = -\dot{b}_a\, y$. The instantaneous power loss per unit volume is given [8] by

$$q_{\text{hys,1}} = \frac{2}{3\pi}\, j_\text{c}\, d_f\, \dot{b}_a. \tag{3.59}$$

This result is one particular reason for working with fine filaments [41] as mentioned in Section 3.3.1.

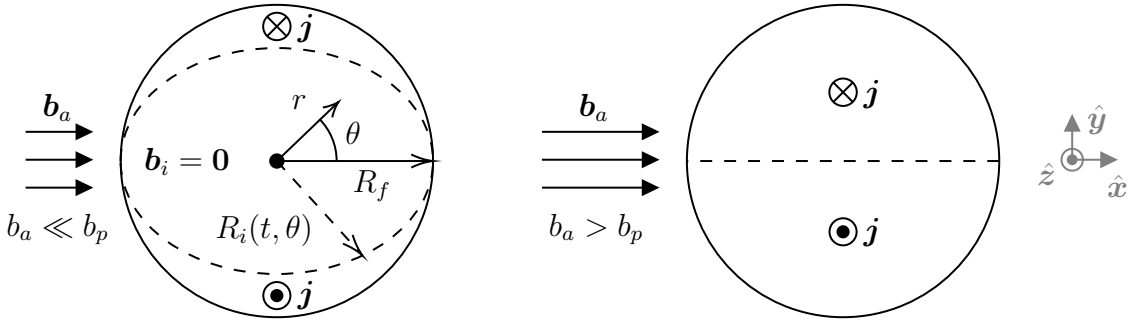

Figure 3.10: Current density $\boldsymbol{j}$ distribution in a superconducting filament of radius R_f subjected to an uniform external increasing transverse flux density $\boldsymbol{b}_a$ of constant direction, in the weak penetration regime (left) and in the full penetration regime (right). $R_i(t,\theta)$ denotes the inner radius of the evolving current shell. Adapted from [8].

In the weak penetration regime, no persistent currents are assumed in the initial state and the field ramp-up is assumed monotonic. Such assumptions are appropriate in the context of the cyclotron ramp-up. When the external field increases, shielding currents are induced in the external part of the filament to prevent the flux density to enter the material. Adapting the development of Carr [8] in a ramp-up context, the filamentary hysteresis loss in weak penetration is

$$q_{\text{hys,1}} = \frac{64}{3\pi j_\text{c} \mu_0^2 d_f}\, b_a^2\, \dot{b}_a, \tag{3.60}$$

for which the full development is given in Appendix A.7. The fact that j_c diverges at zero field (cf. Section 3.3.2) simply induces no hysteresis loss.
Carr [8] has proposed an approximation for the cyclic transverse loss over the full range of applied field. The idea is to interpolate both limiting regimes ($b_a \ll b_p$) and ($b_a > b_p$) and it has been adapted to the instantaneous hysteresis loss as

$$\boxed{q_{\text{hys,1}} = \frac{2 j_\text{c}\, d_f\, b_a^2\, /3\pi}{j_\text{c}^2\, \mu_0^2\, d_f^2\, /32 + b_a^2}\, \dot{b}_a,} \tag{3.61}$$

which tends towards Eq. (3.60) for $b_a \to 0$ and towards Eq. (3.59) for $b_a \gg b_p$. In first approximation, Eq. (3.61) is assumed valid for $\partial j_\text{c}/\partial b \neq 0$ and is interpreted as involving $j_\text{c}(b_a, T)$.

Transverse rotating field

In this section, the amplitude of the external field b_a is assumed to be constant in time and larger than the penetration field b_p given by Eq. (3.58). Let the applied flux density, assumed uniform, be described by:

$$\boldsymbol{b}_a(t) = b_a \left(\cos\left(\omega t + \phi\right) \hat{\boldsymbol{x}} + \sin\left(\omega t + \phi\right) \hat{\boldsymbol{y}}\right), \tag{3.62}$$

in which ω [rad/s] denotes the instantaneous rotation speed of the external field, ϕ [rad] some phase shift, $\hat{\boldsymbol{x}}$ and $\hat{\boldsymbol{y}}$ [-] the orthogonal unit vectors in the plane perpendicular to the axis $\hat{\boldsymbol{z}}$ of the cylinder.

According to Carr [8], still in the Bean approximation, the resulting current distribution can be retrieved from the right part of Fig. 3.10, considering this time the symmetry axis of $\boldsymbol{j}$ is aligned with $\dot{\boldsymbol{b}}_a$ and not with $\boldsymbol{b}_a$. The previous subsection considered the particular case for which $\dot{\boldsymbol{b}}_a$ and $\boldsymbol{b}_a$ were parallel. Moreover, the instantaneous power loss over the volume of the filament, neglecting any macroscopic transport current and assuming a constant critical current [8], is given by

$$q_{\text{hys,1}} = \frac{2}{3\pi}\, j_{\text{c}}\, d_f\, \omega\, b_a. \tag{3.63}$$

This expression is similar to Eq. (3.59), considering that ω can be retrieved from Eq. (3.62) as

$$\omega = \frac{1}{b_a}\left\|\frac{d\boldsymbol{b}_a}{dt}\right\| \neq \frac{1}{b_a}\frac{d}{dt}\left(\|\boldsymbol{b}_a\|\right) = 0. \tag{3.64}$$

The last result shows that Eq. (3.59) involves the norm of the time derivative of the flux density and not the time derivative of its norm. This result is extrapolated to the weak penetration range and the macroscopic hysteresis losses per unit volume are thus obtained as

$$\boxed{q_{\text{hys}} = \lambda_{\text{SC}}\, \frac{2 j_{\text{c}}\, d_f\, b_a^2\,/3\pi}{j_{\text{c}}^2\, d_f^2\, \mu_0^2\,/32 + b_a^2} \left\|\frac{d\boldsymbol{b}_a}{dt}\right\|,} \tag{3.65}$$

which is valid either in a rotating field or in an increasing field of constant direction. In this work, it is also assumed valid for a combination of both cases, i.e. for any $\dot{\boldsymbol{b}}_a : \|d\boldsymbol{b}_a/dt\| > 0$. Equation (3.65) is used in Chapter 6 with the $j_{\text{c}}(b,T)$ dependence taken into account via Bottura's relationship described in Section 3.3.2. The validity of the underlying assumptions in Eq. (3.65) is evaluated with a single filament model in Chapter 7.

Impact of transport current

In the previous section, the transport current I_{t} [A] inside filaments has been neglected and only induced currents were considered. Literature [8, 27, 3] provides results for the transverse field loss inside a fully penetrated filament considering a fixed DC transport current. Carr [8] has shown, again based on the CSM and assuming a constant j_{c} value, that the transport current simply shifts the symmetry axis of the current distribution in the filament (right part of Fig. 3.10) by some value y_1 [m] along the $\hat{\boldsymbol{y}}$-axis, with $y_1 > 0$ if $I_{\text{t}} > 0$ along $\hat{\boldsymbol{z}}$. The shift y_1 corresponds to a net transport current and depends on the transport current ratio $i = I_{\text{t}}/I_{\text{c}}$. According to Carr, the transverse hysteresis loss is then

$$\begin{aligned} q_{\text{hys,1}} &= \frac{2}{3\pi}\, j_{\text{c}}\, d_f\, \dot{b}_a \cdot g(i), \quad \text{with} \quad g(i) = \left(1 - \frac{4y_1^2}{d_f^2}\right)^{3/2} + \frac{3\pi}{2}\frac{y_1}{d_f} i \\ &\text{and} \quad i = \frac{2}{\pi}\left(\frac{2y_1}{d_f}\sqrt{1 - \frac{4y_1^2}{d_f^2}} + \sin^{-1}\frac{2y_1}{d_f}\right). \end{aligned} \tag{3.66}$$

On the other hand, Wilson [3] has derived a relative loss increase of $(1 + i^2)$ for the cyclic loss in a fully penetrated infinite slab, also based on the CSM. Verweij [27] also mentions a relative loss increase of $(1 + i^2)$ for a fully penetrated filament:

$$q_{\text{hys,1}} = \frac{2}{3\pi}\, j_{\text{c}}\, d_f\, \dot{b}_a \cdot \left(1 + i^2\right). \tag{3.67}$$

Physically, the loss increase is due to the work done by the current source to maintain the net transport current despite the induced persistent currents [3]. Moreover, the three authors agree that the impact of transport current is more complex to quantify if the filament is not fully penetrated and Wilson [3] has shown the impact in weak penetration is significant in the case of a slab. Also, as the transport current in the coil increases linearly with time, an additional loss component related to the varying self-field must be considered [27]. In the C400, the transport current ratio is quite low ($i < 0.28$) and the $g(i)$ or $(1 + i^2)$ factors are quite small (below 1.073 and 1.078 respectively). Hence, the impact of transport current on the hysteresis loss is neglected in first approximation. It is investigated in more detail in Chapter 7 and it is also taken into account in Chapter 8.

3.5.3 Inter-filament coupling losses

Even though the longitudinal current can be neglected in the copper matrix, some losses still occur inside the matrix. Their physical origin stems from the variation of the magnetic flux density over several filaments inducing transverse eddy currents inside the matrix and between the filaments. The longitudinal eddy currents are carried by the superconducting filaments and their contribution is already taken into account in the filamentary hysteresis loss.
Similarly to the case of a pair of normal wires, the coupling currents are strongly reduced by twisting the filaments [41]. For this reason, the conductor described in Section 3.3.1 is made of twisted filaments. It can be quantified by the twist length or *twist pitch*, denoted as p_L [m]. The twist pitch represents the longitudinal distance over which the twisted wires complete one full rotation around each other. Verweij [27] mentions the local coupling loss q_c [W/m^3] as

$$q_\mathrm{c} = \frac{1}{\rho_\mathrm{eff}} \left(\frac{p_L}{2\pi}\right)^2 \left\| \frac{d\boldsymbol{b}_l}{dt} \right\|^2, \tag{3.68}$$

with ρ_eff [Ω m] the effective transverse resistivity of the matrix and $\dot{\boldsymbol{b}}_l$ [T/s] the local flux density variation between filaments. In a slowly changing magnetic field, which is a valid assumption in the context of the cyclotron ramp-up of 2 hours, the shielding effect of induced currents at the periphery of the composite wire is negligible. Thus, the local flux density variation $\dot{\boldsymbol{b}}_l$ within the matrix is simply the macroscopic applied flux density variation $d\boldsymbol{b}_l/dt = d\boldsymbol{b}_a/dt$ [41]. Similarly, Carr [8] claims that the total eddy current loss in the matrix of a composite wire of radius R_c [m] is

$$q_\mathrm{c} = \frac{1}{\rho_\mathrm{eff}} \left[\left(\frac{p_L}{2\pi}\right)^2 + \frac{R_c^2}{4} \right] \left\| \frac{d\boldsymbol{b}_a}{dt} \right\|^2, \tag{3.69}$$

also in the case of a small rate of applied field variation. For the C400 conductor presented in Section 3.3.1, the second term in Eq. (3.69) is negligible as the radius $R_c \sim 1$ mm of the core wire is much smaller than the twist pitch $p_L \sim 100$ mm. The twist pitch value provided by the manufacturer is implemented in the code, but not mentioned in this manuscript for confidentiality purposes. The effective transverse resistivity depends on the matrix transverse resistivity, the local Nb-Ti filling factor of the wire and on whether or not transverse currents flow across the Nb-Ti filaments [3, 27, 8]. As the contact resistance at the matrix-filament interface is usually large due to intermetallic layers formed during fabrication heat treatment [3], the effective resistivity is determined [8] by

$$\rho_\mathrm{eff} = \rho_\mathrm{Cu} \frac{1 + \lambda_\mathrm{w}}{1 - \lambda_\mathrm{w}}, \tag{3.70}$$

in which care must be taken to use the local Nb-Ti filling ratio λ_w [26]. The resistivity of copper at $T_\mathrm{He} = 4.2$ K is linked to the resistivity at room temperature ($\rho_\mathrm{Cu}(T = 293\ \mathrm{K}) = 1.68 \times 10^{-8}$ Ωm, [42]) through the RRR coefficient (cf. Section 3.3.1).

At T_{He}, the effective resistivity of the copper matrix is 5.1×10^{-10} Ωm.
Finally, since the inter-filament coupling losses occur within the central wire of the conductor shown in Fig. 3.7 and not in the whole volume of the composite conductor, their volume average can be expressed as

$$\boxed{q_{\text{c}} = \frac{\lambda_{\text{SC}}}{\lambda_{\text{w}}} \frac{1}{\rho_{\text{eff}}} \left(\frac{p_L}{2\pi}\right)^2 \left\| \frac{d\boldsymbol{b}}{dt} \right\|^2 .} \tag{3.71}$$

Magnetoresistance

The presence of magnetic field inside the coil results in an increase in copper resistivity. While the effect is relatively small at room temperature, magnetoresistance becomes significant at lower temperatures and must be consistently considered [41]. Verweij [27] mentions a linear relationship between the relative resistivity increase and the flux density. Simon *et al.* [43] provide a more detailed empirical relation for the magnetoresistive effect on copper at cryogenic temperatures:

$$\begin{aligned} \rho_{\text{Cu}}(b) &= \rho_{\text{Cu}}(b=0)\,(1+\Delta\rho)\,, \\ \text{with} \quad \log(\Delta\rho) &= -2.66 + 0.317\beta + 0.623\beta^2 - 0.184\beta^3 + 0.0183\beta^4 \\ \text{and} \quad \beta &= \log\left(\frac{\rho_{\text{Cu}}(T=273\text{ K})\cdot b}{\rho_{\text{Cu}}}\right) \approx \log(RRR\cdot b)\,, \end{aligned} \tag{3.72}$$

in which $\Delta\rho$ [-] denotes the fractional resistivity increase and $RRR = 80$ the residual resistivity ratio introduced in Section 3.3.1. In this context, the ρ_{Cu}-b relation is almost linear for $b > 0.1$ T. At $b \sim 5$ T, the copper resistivity is doubled. As shown in [41], the validity of the empirical relation has been confirmed on effective transverse resistivity measurements in different magnetic fields. Consequently, Eq. (3.72) is implemented in the code for computing the copper resistivity involved in the effective transverse resistivity (Eq. (3.70)).

CHAPTER 4
MAGNETIC MODEL

In this chapter, the magnetic model of the C400 cyclotron is described. The different choices performed during the study are discussed. The magnetic results, both in steady-state and during ramp-up, are then presented and interpreted.
First, results are computed based on the simplified axisymmetric model of the cyclotron, allowing for lower computing times while capturing the main physical mechanisms at play. Among others, the impact of the helium vessel on magnetodynamics is investigated. Later, results in the full three-dimensional geometry are presented.

Solving the magnetic problem in the complete range from the Nb-Ti filament scale to the full scale of the cyclotron is not possible from a computational point of view. It would require meshing the superconducting coil with a mesh size at least 5 times lower than the filament diameter (~ 10 µm). Considering the cross-section of the coil is around 4×10^{10} µm^2, it would require at least 4×10^8 degrees of freedom (DOFs) to mesh the coil cross-section.
As a consequence, the coil is approximated as a stranded conductor. The validity of such an assumption is discussed in Appendix A.5. From a numerical point of view, the coil is thus homogenized and a source current density $\boldsymbol{j}_{\text{s}}$ is imposed in the volume of the coil as the engineering current density $\boldsymbol{j}_{\text{eng}}$. A more subtle approach taking the filament response into account is presented in Chapter 8.
In the present chapter, as well as in Chapter 6, the a-formulation (Eq. (3.24)) is used to solve the equations numerically with the finite element method. The steady-state configuration refers to the weak formulation of Eq. (3.29). No section is dedicated to the validation of the weak formulation implemented in GetDP as it has already proven to be accurate in previous works [6, 7].

4.1 Symmetry and boundary conditions

The three-dimensional geometry of the cyclotron is represented in Fig. 2.2. The magnetic domain of study is $\Omega = \{(x, y, z) : x \geq 0, y \geq 0, z \leq 0\} = \{(r, y, \theta) : r \geq 0, y \geq 0, \theta \in [-\pi/2; 0]\}$ and its boundary is Γ. The Cartesian coordinate system and the the particular cylindrical coordinate system used in this study are shown in Appendix A.6. The median plane boundary is Γ_{xz} and the four-fold rotational symmetric planes, ($z = 0$) and ($x = 0$), are respectively Γ_{xy} and Γ_{yz}. The remaining part of Γ, the outer boundary, is denoted by Γ_{out}. The distinct sets involved in the weak formulation of Eq. (3.24) are respectively constituted of:

- Ω_{c}: the helium vessel and the ferromagnetic yoke.
- Ω_{s}: the two superconducting sub-coils.

- $\Omega_c^C \backslash \Omega_s$: the air, the vacuum and the liquid helium which is considered as vacuum.

In sub-coil i, the imposed current density is

$$\boldsymbol{j}_s = \begin{cases} \boldsymbol{0}, & \text{for } t < 0, \\ \dfrac{I_i}{h_{\text{coil}} w_{\text{coil}}/2} \dfrac{t}{T_{\text{up}}} \cdot (\sin(\theta)\, \hat{\boldsymbol{x}} - \cos(\theta)\, \hat{\boldsymbol{z}})\,, & \text{for } 0 \leq t \leq T_{\text{up}}, \\ \dfrac{I_i}{h_{\text{coil}} w_{\text{coil}}/2} \cdot (\sin(\theta)\, \hat{\boldsymbol{x}} - \cos(\theta)\, \hat{\boldsymbol{z}})\,, & \text{for } t > T_{\text{up}}, \end{cases} \tag{4.1}$$

where $h_{\text{coil}} w_{\text{coil}}/2$ is the cross-sectional area of each of the two sub-coils shown in Fig. 2.3(b).
Due to the reflection symmetry on Γ_{xz}, the median plane magnetic field must be along the $\hat{\boldsymbol{y}}$-axis. Thus $\bar{\boldsymbol{h}} \times \boldsymbol{n} = \boldsymbol{0}$ on the median plane Γ_{xz}. It corresponds to an homogeneous natural boundary condition. Furthermore, a periodic boundary condition must be applied to Γ_{yz} as:

$$\boldsymbol{a}(\underbrace{0, y, z}_{\in \Gamma_{yz}}) = \begin{pmatrix} \cos(-\pi/2) & 0 & -\sin(-\pi/2) \\ 0 & 1 & 0 \\ \sin(-\pi/2) & 0 & \cos(-\pi/2) \end{pmatrix} \cdot \boldsymbol{a}(\underbrace{-z, y, 0}_{\in \Gamma_{xy}}) = \begin{pmatrix} 0 & 0 & 1 \\ 0 & 1 & 0 \\ -1 & 0 & 0 \end{pmatrix} \cdot \boldsymbol{a}(\underbrace{-z, y, 0}_{\in \Gamma_{xy}}), \tag{4.2}$$

with $\boldsymbol{x} = (0, y, z) \in \Gamma_{yz}$. This boundary condition is strongly imposed through the function space $\mathcal{A}(\Omega)$. Finally, a homogeneous essential boundary condition $\bar{\boldsymbol{b}} \cdot \boldsymbol{n} = 0$ is applied to the outer boundary of the domain $\Gamma_{\text{out}} \in \Gamma_e$. Ideally, this boundary condition should be applied at infinity, meaning the numerical domain should be unbounded. Numerically, an infinite shell transformation [44] is applied to map the unbounded region into a numerical domain of finite size. The spherical shell is shown in Fig. 4.1 with an inner radius of 10 m and an outer radius of 20 m. The size of the computational domain is further discussed in Section 4.6.

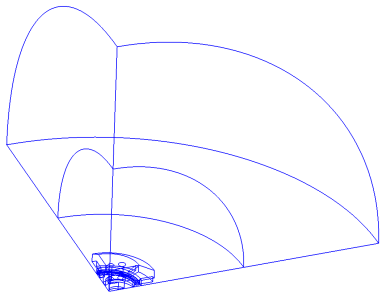

Figure 4.1: Magnetic computational domain. The outer shell is used as an infinite spherical shell transformation.

Axisymmetric geometry

In the simplified axisymmetric geometry, the problem can be solved in two dimensions (2D). In this case, the numerical computational domain corresponds to a slice of one radian of the total geometry. Care must be taken to use an appropriate Jacobian transformation for numerical integration. The simplified axisymmetric geometry is shown in Fig. 2.3. The different physical groups are the same as those presented for the full geometry, except for the periodic boundary conditions. They are replaced by an homogeneous boundary condition $\bar{\boldsymbol{b}} \cdot \boldsymbol{n} = 0$ on the $\hat{\boldsymbol{y}}$-axis of rotational symmetry, in red in Fig. 2.3.

4.2 Material properties

As can be observed in the weak formulation (Eq. (3.24)), the reluctivity ν is required in the whole domain and the electrical conductivity σ is required in Ω_c.
The reluctivity of the ferromagnetic yoke is retrieved from material data as discussed in Section 3.2. The yoke is the only part of the domain in Ω_{NL}. In all other parts of the cyclotron, the reluctivity is assumed constant. In first approximation, neglecting magnetization in Nb-Ti filaments, the reluctivity in Ω_s is simply $\nu = 1/\mu_0$ as the relative permeability of copper is 1 in very good approximation. The relative permeability of the SS304L helium vessel is $\mu_r = 1.035$ [45]. Thus, in $\Omega_{\text{L}} = \Omega \backslash \Omega_{\text{NL}}$,

the reluctivity is $\nu = 1/\mu_0$, except in the helium vessel for which it is $\nu = 1/(1.035\mu_0)$.
From [46], the electrical resistivity of SS304L does not vary more than 0.5% around $\rho = 0.485 \times 10^{-6}$ Ωm in the range $1 \sim 50$ K. The variation of the vessel conductivity around 2.062×10^6 S/m is thus neglected. The electrical conductivity of iron is 10^7 S/m at room temperature [47].
Therefore, the electric and magnetic properties required for the magnetodynamic computation of the cyclotron do not depend on temperature.

4.3 Space and time discretization

This section only introduces basic concepts required for understanding the finite element method in the context of magnetodynamics. For a complete description and a detailed analysis, please refer to the works of P. Dular [21], Geuzaine [6] and J. Dular [7].

4.3.1 Space discretization

As usual when dealing with the finite element method, the computational domain is discretized by means of mesh generation. In the a-formulation, the main unknown is the vector potential $\boldsymbol{a}$. In three dimensions (3D), the vector potential is approximated by a linear combination of edge functions and the degrees of freedom (DOFs) are thus associated to the circulation of $\boldsymbol{a}$ along the different edges of the mesh. Without diving into the concept of Whitney forms, such a discretization ensures the continuity of the normal component of $\boldsymbol{b}$ across facets and it is thus referred to as b-conform [6]. The gauging issue is addressed in Section 4.5. In this work, shape functions of the lowest order are chosen.
In the simplified axisymmetric geometry, the flux density is parallel to the two-dimensional plane of study. Thus, the vector potential is perpendicular to the plane and it is approximated by a linear combination of perpendicular edge functions associated to the nodes of the 2D mesh. The DOFs are associated to the flux of $\boldsymbol{b}$ across edges incident to the different nodes of the mesh. In cylindrical coordinates, the vector potential is simply $\boldsymbol{a} = a_\theta(r, y)\hat{\boldsymbol{\theta}}$ and there is no need for gauging as $\boldsymbol{a}$ is divergence free and it thus satisfies an implicit Coulomb gauge [7].

4.3.2 Time discretization

Again without going too much into details, the numerical integration of the spatially discretized weak formulation leads to a system of N_{DOF} equations, with N_{DOF} degrees of freedom $\boldsymbol{u} \in \mathbb{R}^N$ depending on time as unknowns. It can be written under the semi-discrete form

$$\boldsymbol{M}(\boldsymbol{u}, t)\frac{d\boldsymbol{u}}{dt}(t) + \boldsymbol{K}(\boldsymbol{u}, t)\boldsymbol{u}(t) = \boldsymbol{g}(t), \tag{4.3}$$

with $\boldsymbol{g} \in \mathbb{R}^N$ and $\boldsymbol{M}, \boldsymbol{K} \in \mathbb{R}^{N\times N}$. The successive discrete time steps at which the solution is sought are denoted t_n and the initial solution is provided in $t_0 = 0$. In this work, the numerical time integration of Eq. (4.3) is performed using the backward Euler method, also referred to as the implicit Euler method. At time step t_n, Eq. (4.3) is reduced to a system of the form:

$$\boldsymbol{M}(\boldsymbol{u}; t_n)\frac{\boldsymbol{u}(t_n) - \boldsymbol{u}(t_{n-1})}{t_n - t_{n-1}} + \boldsymbol{K}(\boldsymbol{u}; t_n)\boldsymbol{u}(t_n) = \boldsymbol{g}(t_n) \quad \Rightarrow \quad \boldsymbol{A}(\boldsymbol{u}; t_n)\boldsymbol{u}(t_n) = \boldsymbol{p}(\boldsymbol{u}; t_n), \tag{4.4}$$

in which $\boldsymbol{A} \in \mathbb{R}^{N\times N}$ and $\boldsymbol{p} \in \mathbb{R}^N$ can be retrieved from Δt, $\boldsymbol{M}$, $\boldsymbol{K}$, $\boldsymbol{g}$ and $\boldsymbol{u}(t_{n-1})$. Thus, the system of Eq. (4.4) must be solved at each time step. For the macrosopic resolution at the cyclotron scale, a fixed time step $\Delta t = t_n - t_{n-1}$ [s] is considered.

4.4 Linearization algorithms

Due to the yoke reluctivity dependence on flux density (cf. Section 3.2), Eq. (4.4) is nonlinear through $\boldsymbol{K}$ and thus through $\boldsymbol{A}$. The two most common iterative methods used for dealing with such a nonlinearity are the Picard method and the Newton-Raphson method. In this section, they are first introduced before describing their practical implementation in the context of the cyclotron. Please refer to [7] for an extended description of those methods.
Let us focus on one resolution of the system described by Eq. (4.4), at one specific time step. In this work, the initial estimate $\boldsymbol{u}_0$ of the iterative method is chosen as the solution at the previous time step (or as the initial solution in the case of the first time step). The approximate solution at iteration i is denoted by $\boldsymbol{u}_i$. The residual $\boldsymbol{r}_i$ of the discrete system is

$$\boldsymbol{r}_i = \boldsymbol{p}(\boldsymbol{u}_i) - \boldsymbol{A}(\boldsymbol{u}_i)\boldsymbol{u}_i, \tag{4.5}$$

which is equal to zero if $\boldsymbol{x}_i$ is the exact solution of the system. The convergence criterion used in this study is based on the relative residual: convergence is assumed if $\|\boldsymbol{r}_i\|/\|\boldsymbol{r}_1\| \leq \varepsilon_{\text{rel}}$, with $\|\boldsymbol{r}_i\|$ the 2-norm of the residual at iteration i, $\boldsymbol{r}_1$ the residual after the first iteration and ε_{rel} the relative tolerance. The tolerance strongly depends on the considered problem. In the present context, its most suitable value has been determined to be $\varepsilon_{\text{rel}} = 10^{-10}$. The relative tolerance is particularly small to ensure robustness when the magnetic flux is established inside the cyclotron yoke, in the first part of the ramp-up. The nonlinear algorithm is stopped once either the condition on the relative residual is met or a maximal number of 50 iterations has been reached.
One Picard iteration and one Newton-Raphson iteration respectively read

$$\boldsymbol{A}(\boldsymbol{u}_i)\boldsymbol{u}_{i+1} = \boldsymbol{p}(\boldsymbol{u}_i) \quad \text{and} \quad \boldsymbol{A}(\boldsymbol{u}_i)\boldsymbol{u}_i + \boldsymbol{J}(\boldsymbol{u}_i)\left(\boldsymbol{u}_{i+1} - \boldsymbol{u}_i\right) = \boldsymbol{p}(\boldsymbol{u}_i), \tag{4.6}$$

with $\boldsymbol{J}(\boldsymbol{u})$ the Jacobian matrix linked to the Jacobian of the magnetic constitutive law given earlier (Eq. (3.35)). The Newton-Raphson iteration is based on a first-order Taylor development and exhibits a faster rate of convergence than the Picard method when the estimate is sufficiently close to the solution.

4.4.1 Practical implementation

In steady-state conditions, the Newton-Raphson (NR) algorithm exhibits fast and monotonic convergence of the residual norm, whereas the Picard algorithm does not converge and instead shows cycles. This can be attributed to the concavity of the h-b curve of the yoke, as discussed in Section 3.2. Such divergent behaviour has previously been observed by Dular [7] using the Picard method for ferromagnets in the a-formulation. As a consequence, the Newton-Raphson algorithm is adopted in the present study.

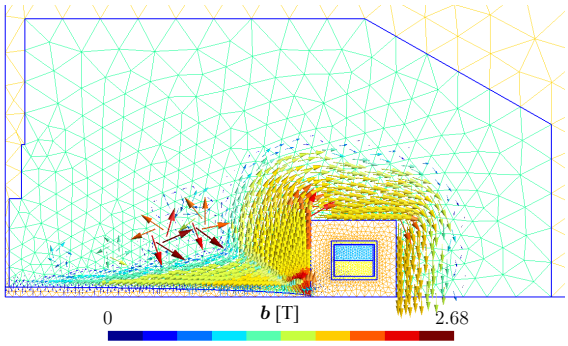

Figure 4.2: Flux density $\boldsymbol{b}$ at $t_1 = 200$ s obtained in the axisymmetric geometry with the NR linearization scheme. Global mesh size $s = 0.8$.

However, certain issues still arise when solving the transient problem. For the sake of clarity, the next results are obtained in the simplified axisymmetric geometry. As shown in Fig. 4.2, non-physical spurious rotational components of the flux density $\boldsymbol{b}$ are observed when the magnetic field is established in the ferromagnetic yoke. The spurious flux vortices are due to cycles appearing in the NR algorithm, which does not converge. Indeed, as illustrated in Fig. 4.3, the relative residual of the NR linearization scheme exhibits these cycles. Dular [7] also observed such cycles with the NR method in the a-formulation for a constitutive law

of opposite concavity. Thus, the iteration cycles may be explained by the opposite concavity of the yoke h-b curve below the threshold flux density $b_{\mathrm{T}} = 0.723$ T (cf. Section 3.2).
One first solution is proposed in the present work: an hybrid iterative method, locally based on the Picard iteration if $b < b_{\mathrm{T}}$ and based on the classical NR iteration if $b \geq b_{\mathrm{T}}$. Numerically, the choice of the method depends on the numerical value of the flux density at the considered Gauss point. As shown in Fig. 4.3, this hybrid method does converge.
A second solution is proposed by numerically setting the reluctivity at $\nu = \nu_{\mathrm{min}} = 140$ m/H below b_{T}. As a consequence, $\partial\nu/\partial b = 0$ for $b \leq b_{\mathrm{T}}$ and the concavity of the h-b curve is not problematic anymore when using the NR scheme. As observed in Fig. 4.3, the modified reluctivity method provides the fastest convergence rate as twice less iterations needed. This is expected as the final scheme is exclusively based on the NR iteration.

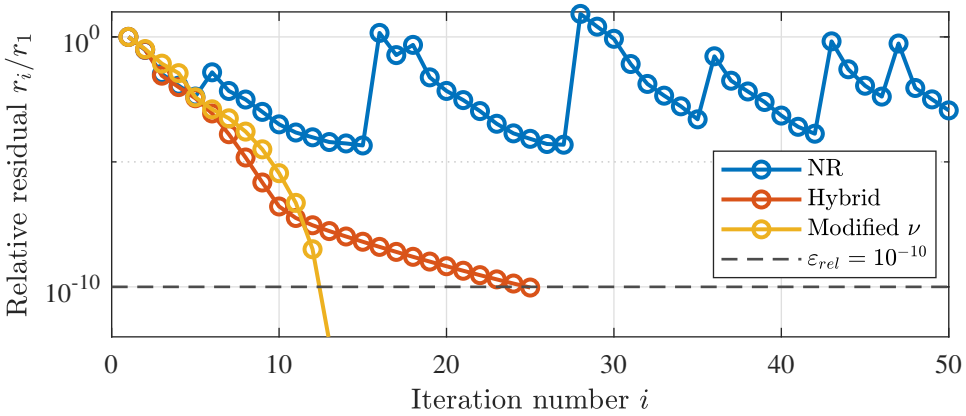

Figure 4.3: Evolution of the relative residual as a function of the iteration number for the axisymmetric geometry, at the first time step $t_1 = \Delta t = 200$ s. Global mesh size $s = 1$. Comparison between the naive NR, the hybrid and the modified reluctivity schemes.

The difference between the numerical results obtained using the hybrid method and the modified reluctivity method is not significant. At $t = 200$ s, the relative difference in magnetic energy contained within the domain is 0.033 %. Additionally, both methods yield identical results under nominal operating conditions as the flux density in the yoke exceeds b_{T}. Given that the present study primarily focuses on the superconducting coil itself, the modified reluctivity method is employed throughout the next parts of the study to benefit from its faster convergence rate. However, it is important to note that the code still includes the implementation of the hybrid method with the material h-b curve, providing the user with the option to choose it if desired.

4.5 Gauge condition

As already mentioned earlier, the vector potential $\boldsymbol{a}$ is not uniquely defined in $\Omega_{\mathrm{c}}^{\mathrm{C}}$ when working in 3D. Thus, a so-called *gauge condition* must be applied to the $\boldsymbol{a}$ field in $\Omega_{\mathrm{c}}^{\mathrm{C}}$. In the magnetostatics case, the gauge condition must be applied in the whole domain. This section briefly presents the two most common gauge conditions, the Coulomb gauge and the co-tree gauge, before comparing their performance in the case of the C400 cyclotron. Please refer to [21, 6] for the rigorous mathematical description of these gauges and their impact on the discretization of the vector potential.
The most common gauge condition is the Coulomb gauge:

$$\nabla \cdot \boldsymbol{a} = 0, \tag{4.7}$$

which can be imposed weakly through the use of a Lagrange multiplier [48]. A more abstract condition is the co-tree gauge condition [48], which reduces the number of DOFs from one per mesh

edge to one per mesh facet. This is done by setting the degrees of freedom associated to the edges of a spanning tree on Ω_c^C (starting with a complete spanning tree on $(\partial\Omega_c \cap \partial\Omega_c^C) \cup \Gamma_e$) to zero, thus focusing only on the egdes of the complementary tree [7, 49]. In the present case, the complete spanning tree surface corresponds to the union of the surfaces Γ_{xy}, Γ_{yz} and Γ_{out} with the interface between the conducting domain (the yoke and the helium vessel) and the surrounding air. In the magnetostatic case, it reduces to the union of Γ_{xy}, Γ_{yz} and Γ_{out}.
The magnetic vector potential fields obtained in steady-state with the two different gauges are represented in Fig. 4.4. As observed, the vector potential is much more regular using the Coulomb gauge. However, the corresponding flux density $\boldsymbol{b}$ (shown in Section 4.8.2) is the same with both gauges. The magnetic energy contained within the domain is $E_m = 3.38771 \times 10^7$ J in both cases. The main difference lies in the number of DOFs: $N_{\text{DOF}} = 43400$ for the Coulomb gauge compared to $N_{\text{DOF}} = 32100$ for the co-tree gauge, resulting in a 69 % increase in computation time. For taking advantage of its efficiency, the co-tree gauge is considered in the next parts of this study.

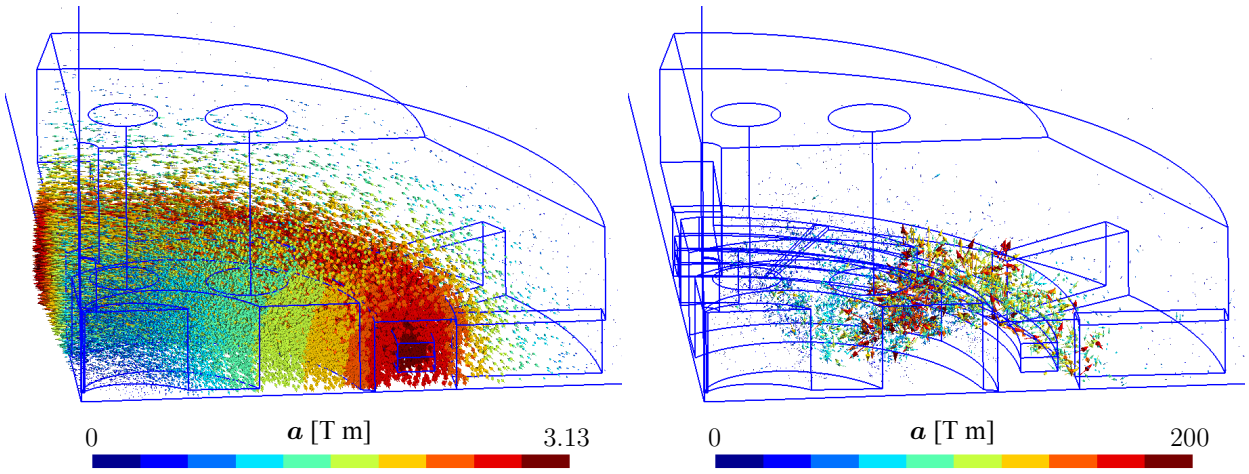

Figure 4.4: Vector potential $\boldsymbol{a}$ field obtained in the magnetostatics case with the Coulomb gauge (at left) and the co-tree gauge (at right). Global mesh size $s = 1$.

4.6 Computational domain

Before diving into the description of the mesh, let us first focus on the appropriate size of the numerical domain. As a reminder, an infinite shell transformation [44] has been used to apply the homogeneous essential boundary condition at infinity, as represented in Fig. 4.1. The outer radius of the numerical domain is denoted by r_{out} [m]. Even though it takes a finite value, the transformation is supposed to represent an unbounded theoretical domain. The evolution of the total magnetic energy as a function of the domain size is represented in Fig. 4.5. As observed, the magnetic energy does not vary significantly when the shell transformation is applied numerically. In this case, the magnetic energy relative variation is 0.019 % between $r_{\text{out}} = 10$ m and $r_{\text{out}} = 100$ m.

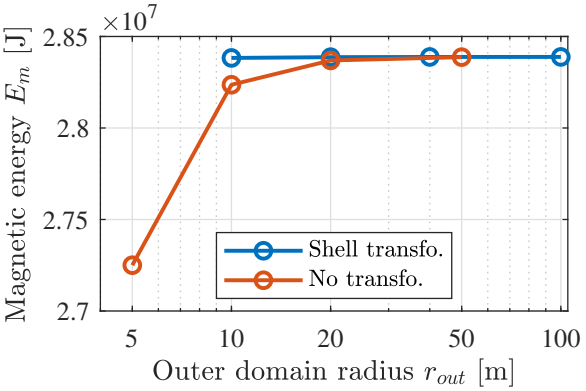

Figure 4.5: Total magnetic energy E_m [J] in the domain as a function of its outer radius r_{out} [m]. Results obtained in axisymmetric magnetostatics with global mesh size $s = 0.5$.

Figure 4.5 emphasizes the necessity of using an infinite shell transformation. The results are also shown for the case where the essential boundary condition is simply applied to the outer boundary of

the domain without any shell transformation. In this case, the boundary condition has a significant impact on the results, leading to a decrease in magnetic energy compared to the shell transformation case. For the following analysis, an outer domain radius of $r_{\text{out}} = 20$ m is chosen, with an infinite shell transformation with an inner radius of 10m.

4.7 Axisymmetric geometry

In a first step, the focus is set on the simplified axisymmetric geometry represented in Fig. 2.3. The two-dimensional problem allows for a significant reduction in the computing time (CPU time) required for the numerical computation. It thus allows to perform preliminary studies such as mesh convergence or selecting the optimal time step in transient analysis. The mesh structure can also be described more easily in 2D.

4.7.1 Mesh convergence

As explained in Section 4.3.1, the magnetic weak formulation is solved numerically by discretizing the domain using a mesh. The final mesh structure, shown in Fig. 4.6, is the result of numerous attempts to find the most suitable mesh structure for the problem. Note that the represented mesh structure is the final one, not its size, which is discussed in next section. Only the final mesh structure is discussed in this report. The main idea is to refine the mesh in regions where the flux density varies the most. Therefore, the mesh is refined near the helium vessel and the pole ends. All the results presented in this subsection are obtained in the magnetostatic configuration.
The global mesh size s [-] is introduced as the global factor multiplying the local mesh size, which is quantified by a local mesh scaling factor p_{mesh} [mm]. A global mesh size of $s = 1$ corresponds to a minimal local mesh size of 20 mm. The mesh size scaling factors p_{mesh} assigned to each of the green, black and red boundaries in Fig. 4.6, as well as to the internal and external boundaries of the infinite shell transformation, are gathered in Tab. 4.1. These factors allow to compute the local mesh size as $p_{\text{mesh}} \cdot s$. Note that the configuration without helium vessel allows for a coarser mesh inside the coil as the surrounding geometry is less intricate.

	p_{mesh} [mm]	
Boundary	Vessel	No vessel
Infinite spherical shell (external)	3500	3500
Infinite spherical shell (internal)	1500	1500
Yoke (external)	300	300
Yoke (internal) and vacuum median plane	60	60
Coil (and helium vessel)	20	45

Table 4.1: Scaling factors p_{mesh} attributed to the different boundaries of the axisymmetric geometry, considering the cases with and without the helium vessel modelled around the coil.

As represented in orange in Fig. 4.6(c), the bottom tip of the yoke is located 6 mm above the median plane of the cyclotron. The scaling factor is locally refined to $p_{\text{mesh}} = 20$ mm to avoid distorded triangles in the mesh between the tip and the symmetry plane, which could lead to numerical inaccuracies. Ensuring the regularity of the mesh elements is particularly important near the median plane, as the flux density in the median plane is necessary for any beam dynamics computation.
The relation between the number of DOFs N_{DOF} [-] and the global mesh size s is represented in Fig. 4.7(a). N_{DOF} corresponds to the size of the linear system that must be solved at each iteration of the linearized algorithm introduced in Section 4.4. As highlighted, the total CPU time required

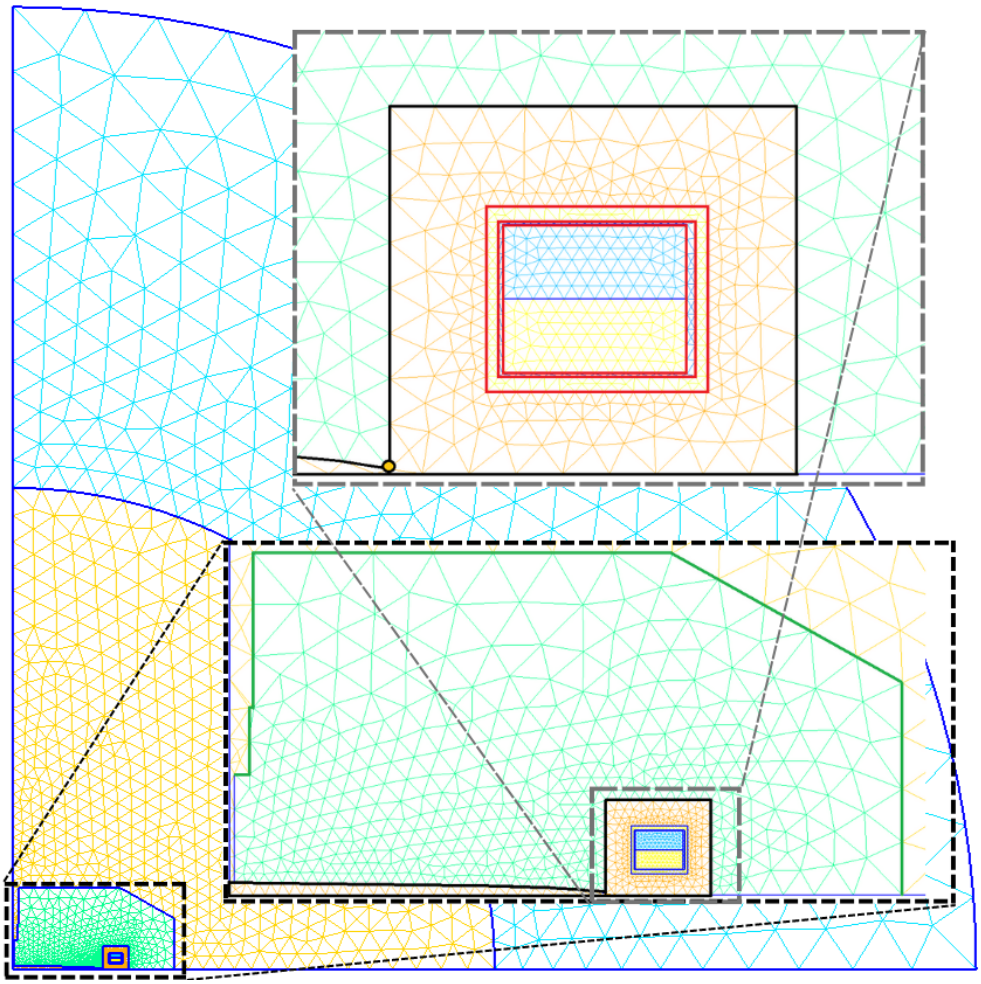

Figure 4.6: Final mesh structure of the axisymmetric model. The represented global mesh size is $s = 1$ and the corresponding minimal mesh size is 20 mm. The external boundary of the yoke is represented in green and its internal boundary in black. The median plane in vacuum is also in black. The boundaries of the helium vessel and of the coil are in red. The point at the tip of the yoke (at 6 mm above the median plane) is represented in orange.

for convergence of the nonlinear algorithm increases greatly with the number of DOFs. In particular, it must be kept in mind that these results are obtained in the magnetostatic configuration (one single step) and that the goal of this study is to perform transient simulations, involving tens or hundreds of time steps. A mesh leading to a CPU time of 1000 s in statics might not be suited for magnetodynamic computations. Note that the number of NR iterations required for reaching convergence also increases when the mesh is refined.

For studying the convergence of the results as the mesh is refined, the focus is set on the magnetic energy defined in Section 3.1.2. As illustrated in Fig. 4.8(a), the magnetic energy within the domain converges towards an asymptotic value as the mesh is refined. The relative difference between the asymptotic values with and without the vessel is 0.13 %.

To highlight the degree of accuracy of the obtained results, the relative error on the total magnetic energy is represented in Fig. 4.8(b). The relative error is computed with respect to the results obtained with global mesh size $s = 0.04$. As observed, the accuracy is greatly increased as the mesh is refined and the convergence is similar in the two configurations. Nevertheless, there is a trade-off between accuracy and speed of execution and the mesh cannot be refined indefinitely. Two different thresholds are set: a relative error of 0.1 % is assumed satisfying for rapid computations, corresponding to a global mesh size of $s_1 = 0.64$. The threshold is set to 0.002 % for the most

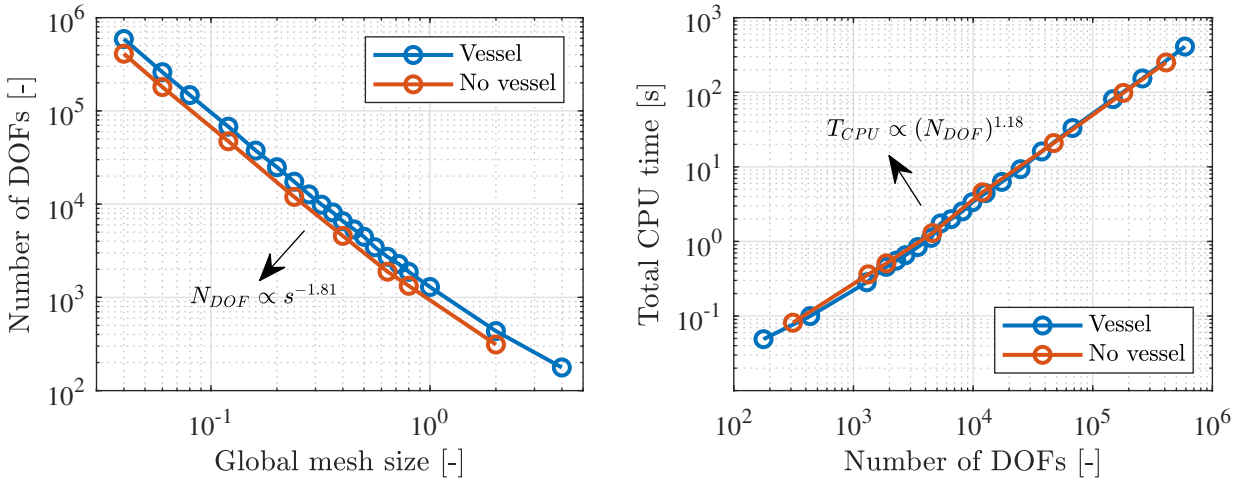

Figure 4.7: Evolution of the number of degrees of freedom as a function of the global mesh size s and corresponding evolution of the total CPU time. Results shown with and without helium vessel.

precise analysis, which corresponds to a global mesh size of $s_2 = 0.12$. However, such a refined mesh cannot be used in 3D and most of the presented results are obtained with global mesh size s_1. Approximating the ramp-up as one quarter of a sine period as done in Appendix A.5, it can be shown that the skin depth, both in the helium vessel and in the iron yoke, is much larger than the corresponding local mesh size. The optimal mesh size derived in this section is therefore considered to be valid in magnetodynamics.

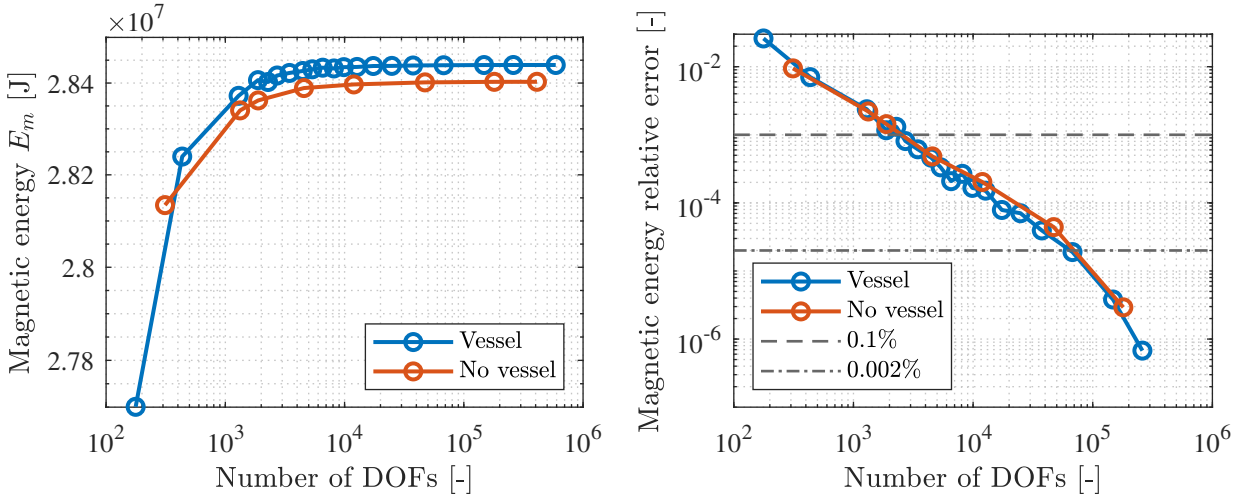

Figure 4.8: Evolution of the total magnetic energy E_m and its relative error as a function of the number of degrees of freedom. Both results shown with and without helium vessel.

4.7.2 Impact of the time step

Now that the impact of the spatial discretization on results has been discussed, let us explore the impact of the time step on transient results. As a reminder, the backward Euler method is used for the time integration of the spatially discretized problem. The time step of the numerical scheme has been varied between $\Delta t = 10$ s and $\Delta t = 500$ s, the total ramp-up time is $T_{\text{up}} = 7200$ s and the total simulation time is 9000 s. In particular, two global quantities are studied. The total Joule loss Q_{j} [W] in the ferromagnetic yoke due to eddy currents, obtained by integrating Eq. (3.55) over the volume of the yoke, is linked to the establishment of the magnetic flux inside the yoke. Second, as

the thermal study focuses on the coil itself, the magnetic energy E_m inside the superconducting coil is also retrieved.

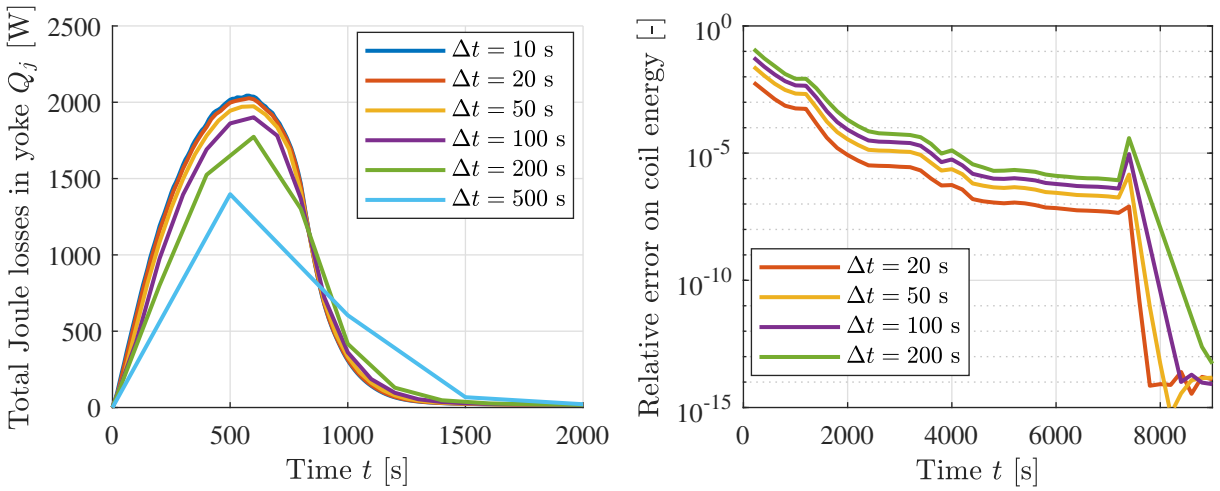

(a) (b)

Figure 4.9: (a) Evolution of the total Joule losses Q_{j} in the yoke, and (b) the relative error on the magnetic energy in the superconducting coil, for various time steps Δt. Relative error computed with respect to the results for $\Delta t = 10$ s. Results obtained with global mesh size $s = 0.64$ and without helium vessel.

As can be observed in Fig. 4.9(a), the time step has a significant impact on the total Joule loss in the ferromagnetic yoke. The yoke Joule losses are the largest for $t < 1200$ s, which corresponds to the time required for the magnetic flux to establish itself inside the yoke during ramp-up. Once it is established in the complete yoke, the induced currents are much lower. This phenomenon is discussed in next section. The main conclusion is that the time step should not exceed $\Delta t = 100$ s for obtaining a relatively accurate representation of the flux penetration in the ferromagnetic yoke. The relative error on the magnetic energy inside the conductor is shown in Fig. 4.9(b). It is computed at intervals of 200 s, comparing the results to those obtained with a time step of $\Delta t = 10$ s. As observed, the relative error decreases over time. Notably, there is a significant drop in the error for $t > 7200$ s, suggesting the steady-state regime is reached due to the constant injected current. The relatively larger error for $t < 1200$ s may be attributed to the flux penetration in the yoke. As expected, refining the time step leads to a reduction in the relative error. However, this comes at the cost of a substantial increase in the total number of iterations required for solving the linear systems, rising from 196 for $\Delta t = 200$ s to 2360 for $\Delta t = 10$ s. Hence, there is again a trade-off between accuracy and computation time. The determination of the optimal time step is not universal and will be further discussed in Chapter 6 when considering the coupled thermal problem. For now, a time step of $\Delta t = 20$ s is selected as it yields a relative error of less than 1 % at all times.

4.7.3 Main results

For clarity, the mesh is no more represented along physical results. As already mentioned in previous section, the magnetodynamics in the cyclotron are mostly dictated by the establishment of the flux density in the ferromagnetic yoke. The magnetic problem is thus strongly nonlinear. The evolution of the flux density during ramp-up is shown in Fig. 4.10.

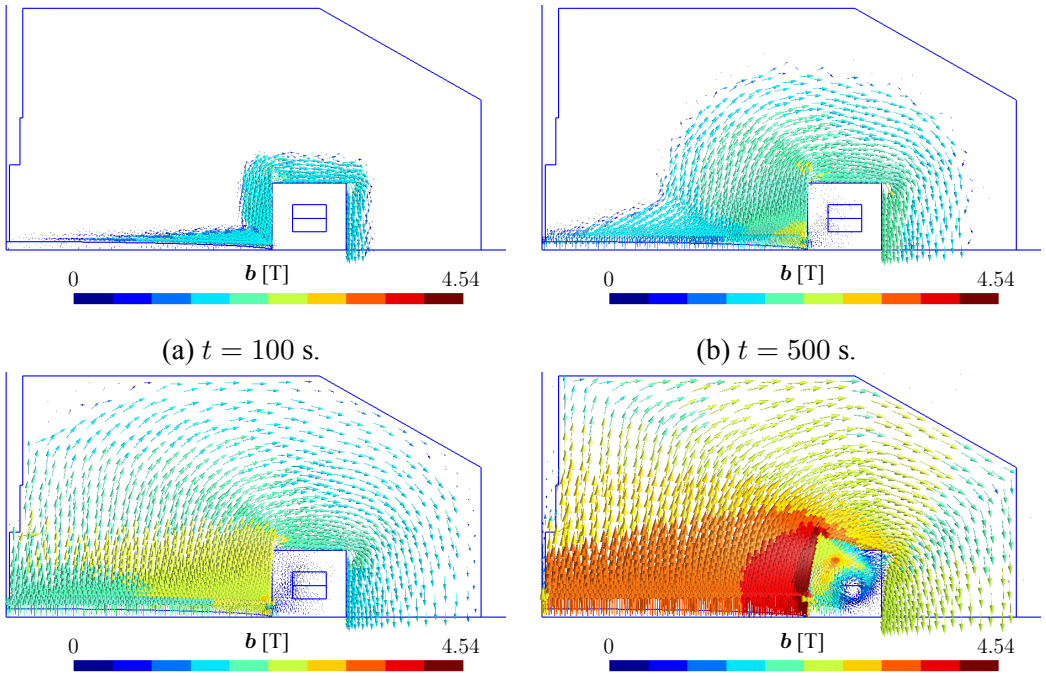

(a) $t = 100$ s. (b) $t = 500$ s.

(c) $t = 1000$ s. (d) $t = 9000$ s.

Figure 4.10: Flux density $\boldsymbol{b}$ at different instants. Results obtained with global mesh size $s = 0.64$, $\Delta t = 20$ s and without helium vessel.

As can be observed, the flux density enters the yoke through its inner boundary. Then, it progresses until the complete yoke is penetrated around $t = 1200$ s. Once the flux has entered the yoke, the saturation regime (at $b \sim 2.2$ T, cf. Section 3.2) is quickly reached. At $t = 9000$ s, the cyclotron is in steady-state and the field in Fig. 4.10(b) corresponds to the field obtained with a magnetostatic resolution. The ferromagnetic yoke channels the flux lines and the leakage flux is negligible. The flux density is maximal in the yoke, close to the median plane. The magnetostatic results have been confirmed using the *Opera* software at IBA.
The establishment of magnetic flux within the yoke induces an electric field and results in the generation of eddy currents, as shown in Fig. 4.11. The correlation with Fig. 4.10(a-c) is remarkable. Once the flux has fully penetrated the yoke, the intensity of eddy currents significantly decreases, leading to a corresponding reduction in total Joule loss, as highlighted in Fig. 4.9(a).

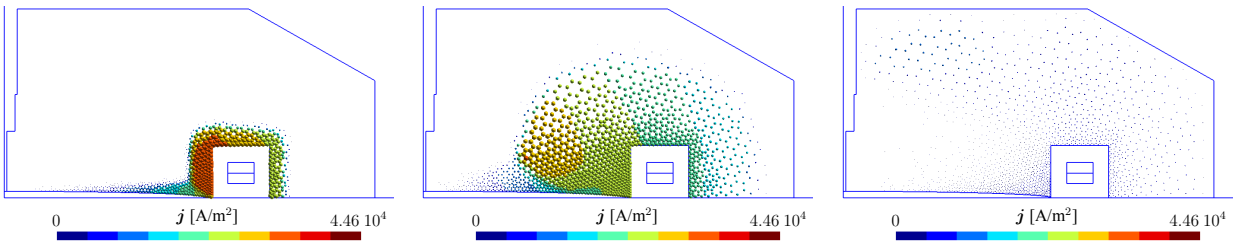

(a) $t = 100$ s. (b) $t = 500$ s. (c) $t = 1000$ s.

Figure 4.11: Out-of-plane induced current density $\boldsymbol{j}$ in the yoke at different instants. Results obtained with global mesh size $s = 0.64$, $\Delta t = 20$ s and without helium vessel.

Additionally, as the ferromagnetic yoke gradually saturates, the magnetic field rotates around the conductor, as illustrated in Fig. 4.12. The various sections of the coil do not experience the same variation in flux density. This is a direct result of the nonlinear magnetic behaviour of the yoke, which affects the magnetic field within the entire cavity. It should be noted that the position of the

central region of low field moves downward over time. Such a behaviour can have an impact on AC loss, as mentioned in Chapters 6 and 8.

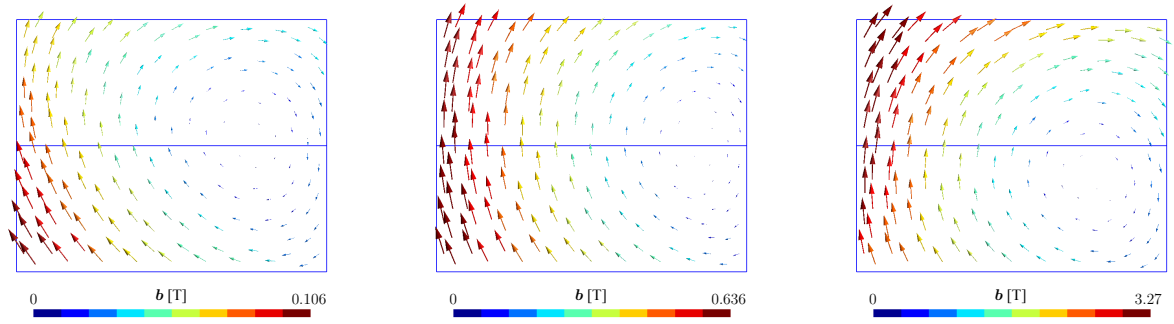

(a) $t = 200$ s. (b) $t = 1200$ s. (c) $t = 9000$ s.

Figure 4.12: Flux density $\boldsymbol{b}$ in the conductor at different instants. Results obtained with global mesh size $s = 0.64$, $\Delta t = 20$ s and without helium vessel. For clarity, the color scale has been adapted to each instant.

4.7.4 Impact of the helium vessel

As already mentioned in Section 4.7.1, the relative difference in total magnetic energy is 0.13 % between the two configurations, with and without the helium vessel.

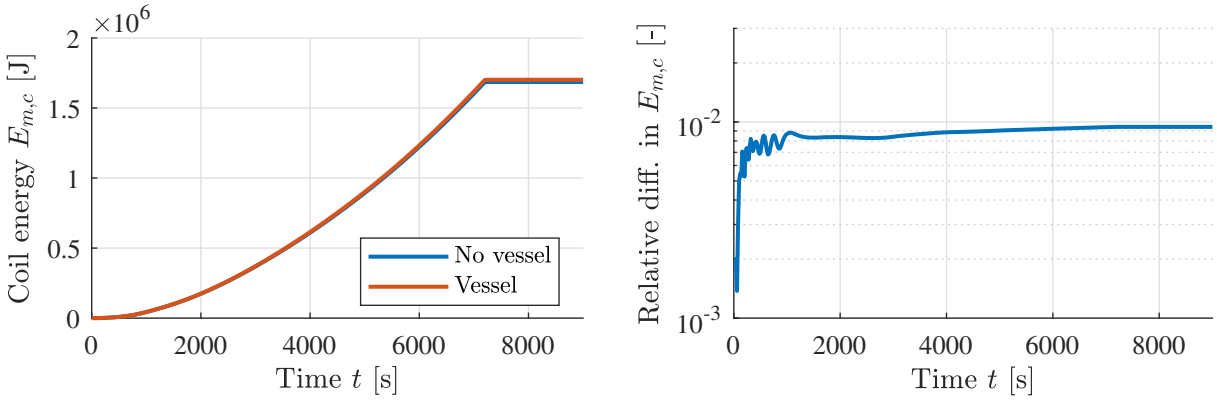

Figure 4.13: Evolution of the coil magnetic energy $E_{m,c}$ with and without vessel and the corresponding relative difference. Results obtained with global mesh size $s = 0.64$ and $\Delta t = 20$ s.

As the thermal study will focus on the coil, let us examine the impact of the helium vessel on the magnetic energy of the conductor during ramp-up. As highlighted in Section 3.5, the coil losses primarily depend on the flux density and its variation. Therefore, the magnetic energy of the coil, which represents the volume integral of a quadratic form of the local flux density, serves as an appropriate quantity for evaluating the influence of the vessel on magnetodynamics. As shown in Fig. 4.13, the magnetic energy stored in the coil is only minimally affected when the vessel is added to the system, despite the presence of opposing eddy currents in the vessel due to flux variation. However, due to the small thickness of the helium vessel, the impact of these eddy currents on the magnetic energy within the conductor is negligible. The relative difference in energy between the two configurations is less than 1 % at any given moment. The magnetic energy is slightly higher when the vessel is included, which can be attributed to the vessel's relative permeability of $\mu_r =$

1.05. It should be noted that the magnetic energy curve does not follow a quadratic relationship. Instead, it evolves as $E_{m,c} \propto t^{1.74}$. This behaviour may be attributed to the nonlinearity of the ferromagnetic yoke. The helium vessel is neglected in the next parts of this chapter.

4.7.5 Magnetic time constant

When coupling two different physics, it is convenient to compare their respective characteristic time constants. In this context, a current step of nominal amplitude is injected in the coil. The evolution of the total magnetic energy is shown in Fig. 4.14. As observed, it cannot be fitted easily as an exponential as the behaviour of the system is strongly nonlinear. Still, the magnetic time constant τ_m [s] can be estimated by assuming $E_m \sim E_0(1-\exp(-t/\tau_m))$ with E_0 [-] the steady-state magnetic energy, in which case it is given by $\tau_m = 13.23$ s.

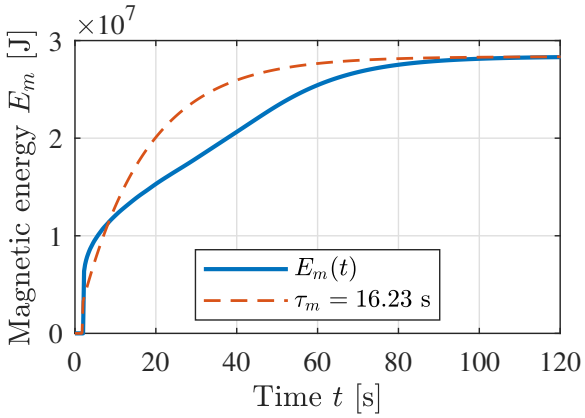

Figure 4.14: Evolution of the total magnetic energy E_m after a step of nominal current imposed at $t = 2$ s. Results obtained with global mesh size $s = 0.64$ and $\Delta t = 0.25$ s.

4.7.6 Three-dimensional axisymmetry

Finally, let us highlight the equivalence between the results obtained from a 2D axisymmetric model and those obtained from a 3D model of the axisymmetric geometry. The steady-state flux density is represented in Fig. 4.15(a) and is very similar to what has been obtained in Fig. 4.10(d). Consequently, the flux density b_y in the median plane is also nearly identical, as shown in Fig. 4.15(b). The staircase shape of the 2D result may be due to the specific discretization adopted in 2D, with nodes instead of edges as in 3D. Additionally, the 3D mesh consists of tetrahedra rather than triangles. The total magnetic energy is $E_m = 2.844 \times 10^7$ J in 2D compared to $E_m = 2.831 \times 10^7$ J in 3D. However, the number of DOFs is 1947 in 2D and 344100 in 3D, resulting in a computing time approximately 5000 times longer in 3D (~ 4200 s).
The positive field index for $r < R_v$, satisfying the isochronism condition introduced in Section 1.2, is observed in Fig. 4.15(b). R_v [m] denotes the radius of the poles. The positive field index is a direct consequence of the elliptic pole gap.

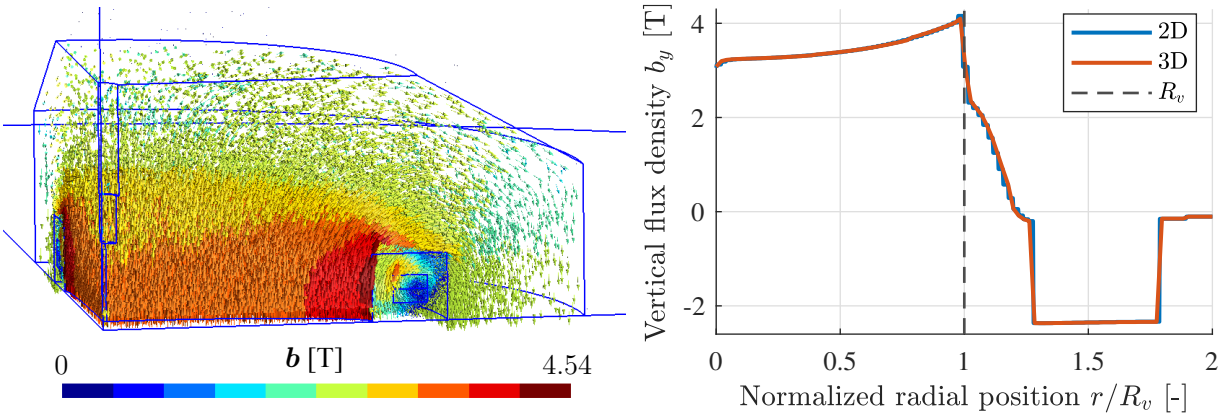

Figure 4.15: (a) Steady-state flux density $\boldsymbol{b}$ field computed in 3D and (b) median plane flux density compared to the 2D axisymmetric model result. Results obtained with global mesh size $s = 0.64$.

4.8 Complete three-dimensional geometry

Let us now discuss the magnetic results obtained with a complete three-dimensional model of the C400 cyclotron as introduced in Fig. 2.2. In this section, all results are presented without the helium vessel. As the thermal coupling is not introduced yet, the focus is mainly set on the magnetic results under steady-state operating conditions. Nevertheless, some dynamic results are also presented.

4.8.1 Mesh convergence

The structure of the mesh used for discretizing the 3D model is more complex as the one discussed in Section 4.7.1 as the 3D geometry includes the spiralized poles, the off-center holes in the yoke and the extraction channels. The 3D mesh structure is shown in Appendix B.1. Compared to the axisymmetric mesh, the mesh has been refined in the spiral ends and in the median plane.

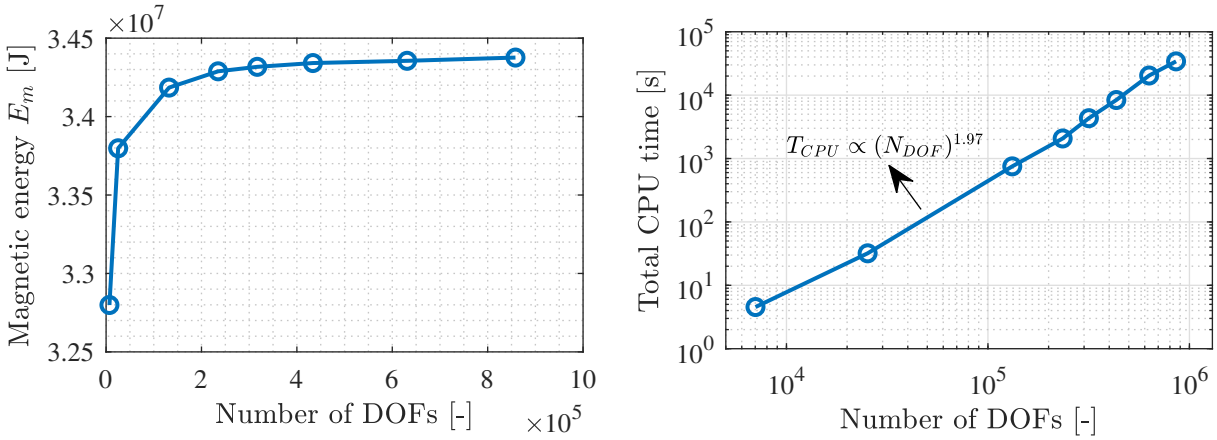

Figure 4.16: Evolution of the magnetic energy E_m and the total CPU time against the number of DOFs in 3D magnetostatics. Global mesh size s varied between 4 and 0.5.

As highlighted in Fig. 4.16(a), convergence of the magnetic energy is also observed in the complete geometry. However, the number of DOFs is much larger in 3D than in 2D: 132400 DOFs in 3D compared to 939 in 2D for a global mesh size of $s = 1$. Consequently, the total computing time has dramatically increased as shown in Fig. 4.16(b).
For a global mesh size of $s = 0.64$, the CPU time is 8400 s, which is appropriate for magnetostatics. However, in the context of magnetodynamic simulations with multiple hundreds of time steps, the mesh refinement level must be decreased. A reasonable value is $s = 1$, which corresponds to $N_{\text{DOF}} = 1.3 \times 10^5$ and results in a relative magnetic energy difference of 0.58 % compared to the most refined mesh. It is worth noting that in 3D the total computing time scales as $T_{\text{CPU}} \propto N_{\text{DOF}}^{1.97}$, while the number of DOFs scales as $N_{\text{DOF}} \propto s^{-2.73}$. Therefore, the total CPU time varies as $T_{\text{CPU}} \propto s^{-5.38}$. Reducing the mesh size by half yields a 4000 % CPU time increase.

4.8.2 Static results

The steady-state flux density is represented in Fig. 4.17. The maximal flux density has increased with respect to the axisymmetric geometry, even though parts of the yoke have been removed. Similarly, the total magnetic energy has increased from 2.84×10^7 J to 3.43×10^7 J. The flux density is maximal in the spiral ends, where the vertical magnetic flux is channeled in a slab of decreasing thickness. Notably, the spiralized poles have a significant impact on the flux density in the median plane. The flux density outside of the cyclotron quickly tends towards zero. Consequently, the flux

density in the modified extraction channels is also negligible. In the outer return part of the yoke, the flux density is in the opposite direction compared to the inner cavity, as expected.

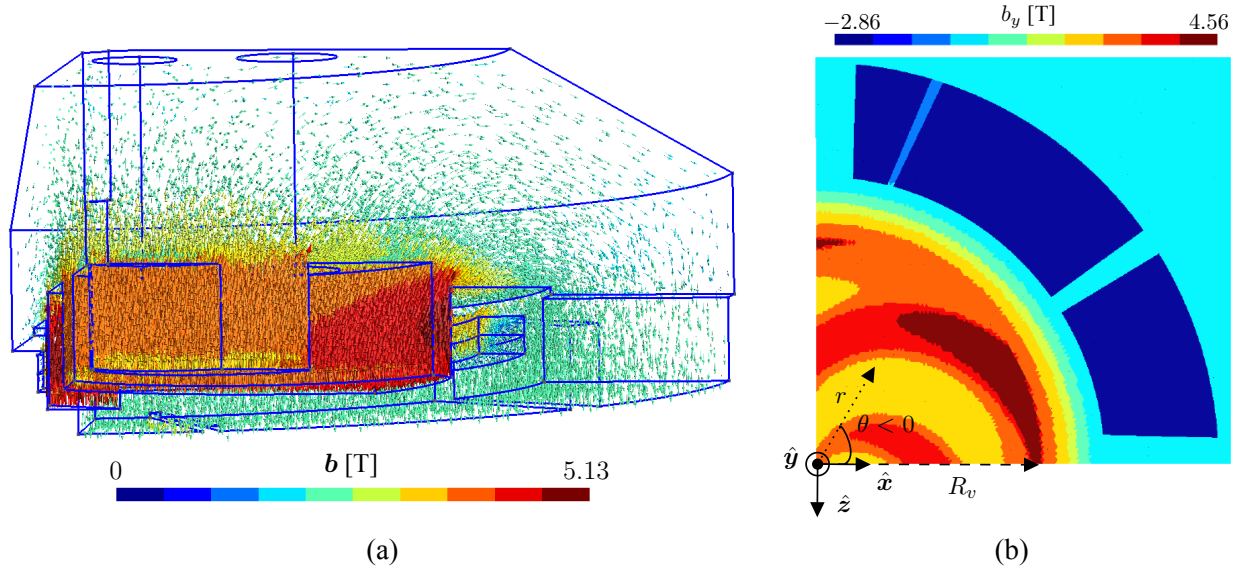

(a) (b)

Figure 4.17: Steady-state flux density $\boldsymbol{b}$, (a) in the ferromagnetic yoke and in the conductor, and (b) in the median plane (top view). Results obtained with global mesh size $s = 0.64$.

The maximal flux density on the conductor is $b_{\text{c,max}} = 3.58$ T, which corresponds to a Nb-Ti critical current density $j_{\text{c}} = 3928$ A/mm^2 at $T_{\text{He}} = 4.2$ K. It corresponds to a conductor critical current of $I_{\text{c}} = 3563$ A, thus leading to a maximal transport current ratio of $i = 0.28$. Next, the influence of the spiralized poles on the median plane flux density is further investigated.

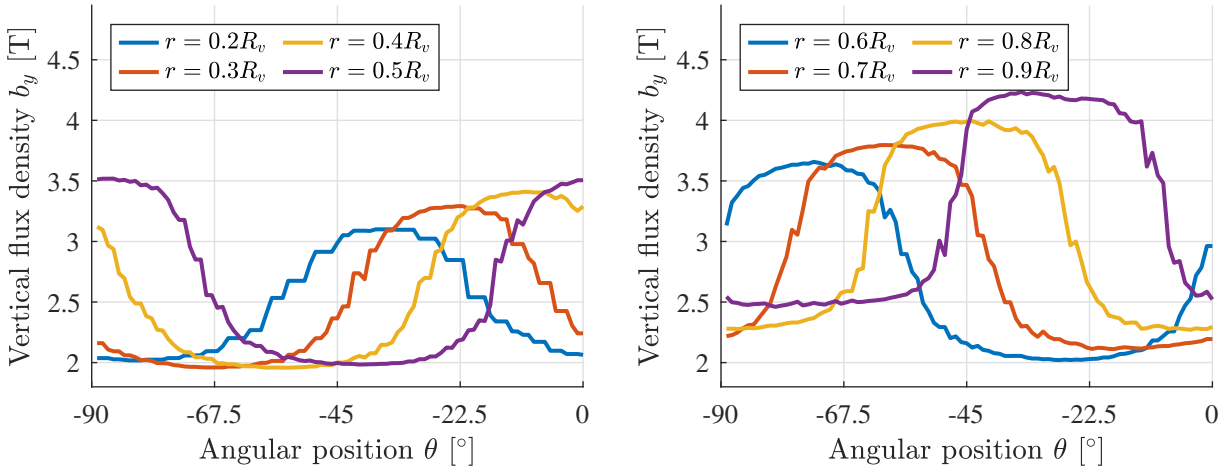

Figure 4.18: Evolution of the median plane flux density b_y along the azimuthal coordinate θ for various radii r, fractions of the pole radius R_v. Results obtained with global mesh size $s = 0.64$.

The evolution of the flux density b_y along circular paths of various radii is shown in Fig. 4.18. The reference of the azimuthal coordinate θ is represented in Fig. 4.17(b). For each separate curve, the flux density is larger between yoke poles and lower between valleys. As expected, all curves are periodic. Further, the pole and valley flux densities are respectively denoted by b_{pol} [T] and b_{val} [T]. As the radial coordinate increases, the pole flux density becomes larger. This behaviour is highlighted in Fig. 4.19 and is desired for an isochronous cyclotron. The quantities b_{pol} and b_{val} were determined as the maximum and minimum values, respectively, obtained from the median flux

density curves shown above. These curves have now been filtered using a moving average over a $5°$ range to reduce noise. As observed, the pole flux density nearly doubles from the center of the cyclotron to the pole edge. Remarkably, the pole flux density matches the valley flux density as the radius tends towards zero. Such a behaviour is expected as the circular path reduces to the central point of the cyclotron. For $r/R_v > 0.5$, the valley flux density also increases with r.

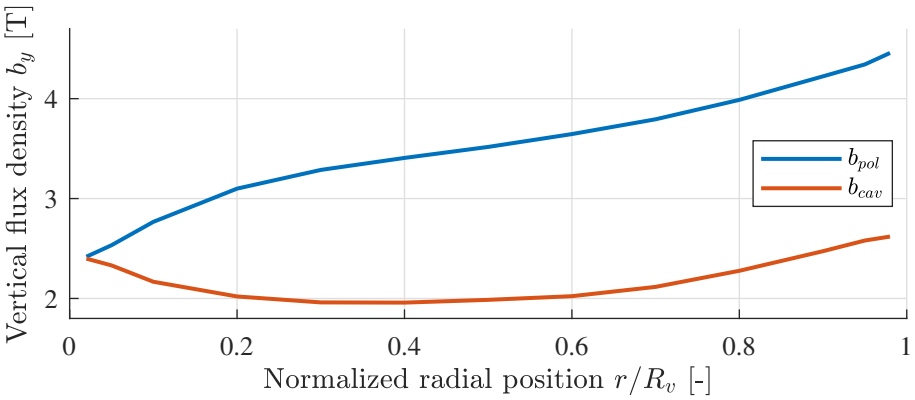

Figure 4.19: Evolution of the pole b_{pol} and cavity b_{cav} flux densities along the radial coordinate r normalized by the pole radius R_v. Results obtained with global mesh size $s = 0.64$.

The influence of the extraction channels and the off-center yoke holes on the field distribution is also assessed. As can be observed in Fig. 4.20(a), the median plane pole flux density is increased as the holes are filled. Such a result is expected as parts of the yoke are added while keeping the same spiralized poles. The impact of the holes is thus significant and they must be included in the complete model.

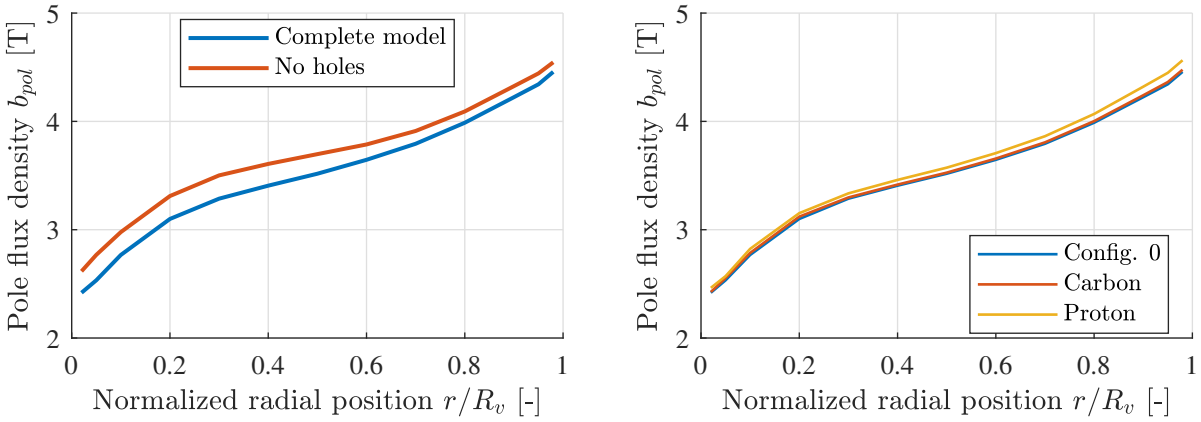

(a) (b)

Figure 4.20: Pole flux density b_{pol} along the normalized radial coordinate r/R_v (a) compared to the model without the off-center holes and the extraction channels, and (b) compared to the different nominal current conditions gathered in Tab. 2.1. Results obtained with global mesh size $s = 0.64$.

Finally, the pole flux density is also represented in Fig. 4.20(b) for the carbon and proton configurations introduced in Tab. 2.1. The two carbon configurations produce the same $b_{\text{pol}}(r)$ variations and a similar behaviour has been observed for the two proton configurations. Thus, one single curve is shown for each configuration. The proton configuration exhibits a larger field near extraction, at the end of the poles. It is expected as the injected current is higher for the proton configurations compared to the carbon ones. The carbon configuration is very similar to the default configuration (Config. 0) that has been studied so far.

4.8.3 Dynamic results

In 3D, the saturation of the yoke does not occur at the same rate as in axisymmetric conditions. At $t = 1200$ s, the axisymmetric yoke is already fully penetrated by the magnetic flux. However, the real yoke, as highlighted in Fig. 4.21(a), has not reached full penetration yet. Similarly, the total yoke Joule losses, resulting from the magnetic flux entering the yoke, are lower in 3D but occur over a longer time scale compared to 2D, as shown in Fig. 4.21(b). This can be attributed to the spiralized poles, which prevent the azimuthal flow of eddy currents in the bottom part of the yoke. As expected, the magnetic behaviour is more complex in 3D than in axisymmetric conditions.

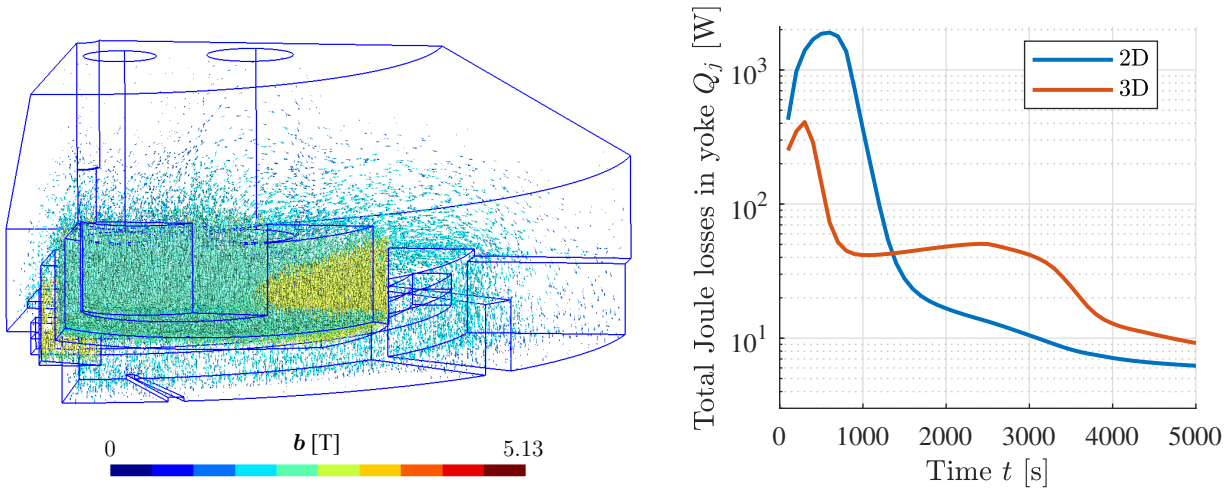

(a) (b) .

Figure 4.21: (a) Flux density $\boldsymbol{b}$ in the ferromagnetic yoke and in the conductor at $t = 1200$ s, and (b) total yoke Joule losses Q_{j}, for $\Delta t = 100$ s. Results obtained with global mesh size $s = 1$.

As emphasized in this chapter, the magnetic behaviour of the C400 cyclotron has been thoroughly investigated. The numerical methods involved in the resolution of the magnetic problem have been discussed and various numerical parameters have been fine-tuned for optimal efficiency. The complexity of the model has been increased step by step, starting from the 2D axisymmetric geometry, showing the equivalence of the 3D axisymmetric model and finally modelling the complete geometry of the cyclotron. The spiralized poles have a significant impact on the flux density within the whole cyclotron. In particular, the effect of the poles on the mean plane flux density was presented. In addition, the need to include the off-center vertical holes in the yoke and the extraction channels in the final model was demonstrated, as they also modify the flux density distribution.
Before focusing on the coupling between magnetodynamics and thermodynamics in Chapter 6, the thermal solver is discussed in the next chapter.

CHAPTER 5

THERMAL MODEL

In this chapter, the thermal model of the coil is described. First, the thermal formulation is validated in a reference geometry. Then, the thermal numerical domain and the corresponding boundary conditions are discussed. As mentioned in the beginning of Chapter 4, the coil has been homogenized. The effective thermal properties are thus derived and their temperature dependence is also described. As the properties depend on temperature, the discretized formulation is nonlinear and an iterative procedure must be used for solving the system of equations. Before coupling the thermal solver with the magnetodynamic solver presented in the previous chapter, the thermal time constant of the homogenized coil is briefly discussed.

5.1 Validation of the weak formulation

The reference geometry proposed for the thermal modelling validation is an infinite cylinder. This geometry has been extensively studied in [40]. As represented in Fig. 5.1, only its cross-section is modelled. The cylinder is considered isotropic and its thermal conductivity is thus a scalar. The thermal dependence of all material properties is neglected. A convective boundary condition is applied to the cylinder boundary. Considering an uniform volumetric heat source of $q_\mathrm{s} = 500$ W/m^3, the steady-state temperature field is [40]

$$T(r) = \frac{q_\mathrm{s} R^2}{4\kappa}\left(1 - \left(\frac{r}{R}\right)^2\right) + \frac{q_\mathrm{s} R}{2h} + T_\infty. \qquad (5.1)$$

As shown in Fig. 5.2(a), the temperature field is accurately retrieved using a coarse mesh of characteristic size 0.1 m.

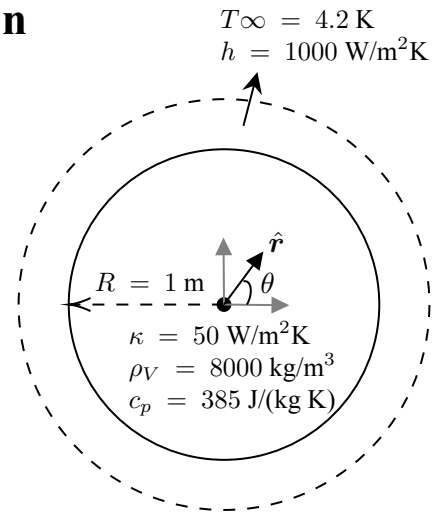

Figure 5.1: Reference geometry for the thermal validation case and corresponding material properties.

A transient conduction problem without heat generation is considered next. The cylinder, initially at temperature $T_i = 8$ K, is suddenly immersed in the convective bath at $T_\infty = 4.2$ K. From [40], the temperature field is given in the form of an infinite series:

$$\frac{T - T_\infty}{T_i - T_\infty} = \sum_{n=1}^{\infty} \frac{2}{\xi_n} \frac{J_1(\xi_n)}{J_0^2(\xi_n) + J_1^2(\xi_n)} \exp\left(\frac{-\xi_n^2 \kappa t}{\rho_V c_p R^2}\right) J_0\left(\xi_n \frac{r}{R}\right), \text{ with } \xi_n \frac{J_1(\xi_n)}{J_0(\xi_n)} = \frac{hR}{\kappa}, \qquad (5.2)$$

J_0 and J_1 denoting Bessel functions of first kind. As shown in Fig. 5.2(b), the numerical solution ($\Delta t = 100$ s) accurately captures the transient behaviour of the cylinder at different locations. In

conclusion, the proposed weak formulation (Eq. (3.53)) appropriately incorporates heat generation, transient conduction, and convective boundary conditions.

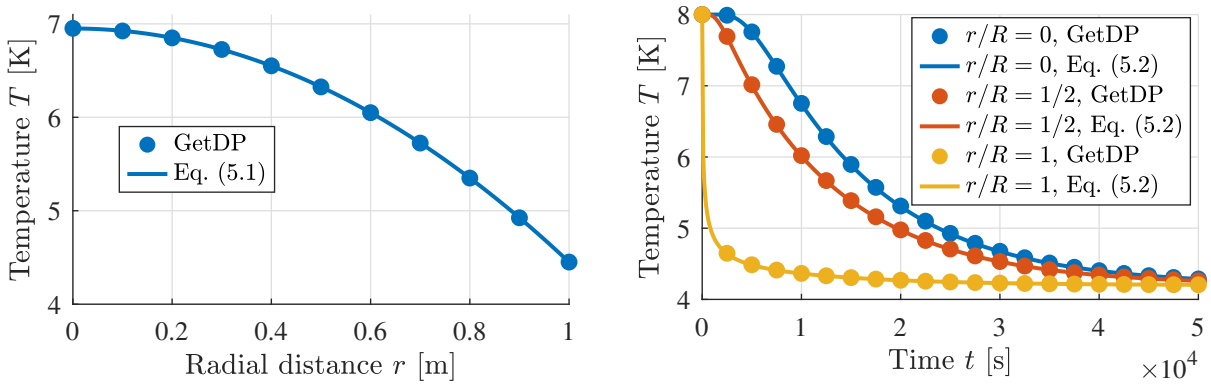

Figure 5.2: Comparison of the temperature distribution obtained with the numerical model (GetDP) and the theoretical distribution in the reference geometry. Static and dynamic results.

5.2 Thermal domain and boundary conditions

In the thermal study, the focus is set on the cold mass of the cyclotron. More precisely, the goal is to determine the temperature distribution inside the superconducting coil. The model implemented in the present study also allows the temperature distribution to be retrieved in the helium vessel.

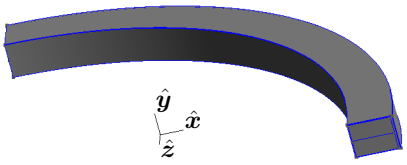

Figure 5.3: Global view of the thermal domain composed of the coil and the vessel.

Numerically, the thermal domain Ω_{th} is composed of two sub-domains: the superconducting coil denoted by $\Omega_{\text{th},1}$ and the helium vessel $\Omega_{\text{th},2}$. A global view of the thermal domain is shown in Fig. 5.3. One cross-section of the two sub-domains is represented in Fig. 5.4.

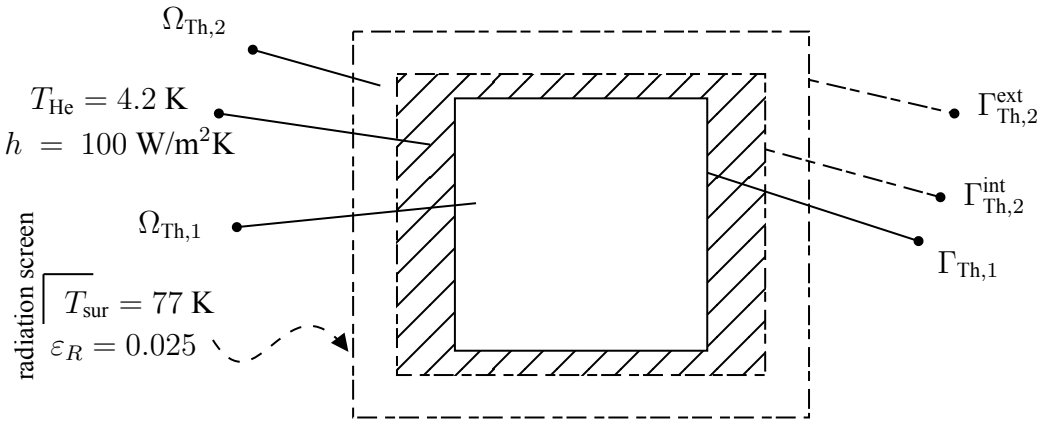

Figure 5.4: Cross-section of the thermal computational domain Ω_{Th} composed of the superconducting coil $\Omega_{\text{Th},1}$ and the helium vessel $\Omega_{\text{Th},2}$. Liquid helium flows between the two thermal subdomains. The thermal boundary conditions are as follows: convective cooling on the boundary $\Gamma_{\text{Th},1}$ of the coil. Similar convective cooling on the vessel interior boundary $\Gamma^{\text{int}}_{\text{Th},2}$ and radiative heat transfer on its exterior boundary $\Gamma^{\text{int}}_{\text{Th},2}$.

The determination of the temperature distribution inside the flowing helium requires solving Navier-Stokes equations, which goes beyond the scope of the present study. The heat capacity of the helium

bath is assumed infinite, meaning its temperature remains constant at $T_{\text{He}} = 4.2$ K. Consequently, the two thermal sub-domains are thermally decoupled, resulting in a natural domain decomposition. This decomposition allows for the separate solution of the two systems, reducing the size of the discretized system that needs to be solved. The two sub-domains and the corresponding boundary conditions are discussed next. The material properties are presented in the following section.

Coil thermal domain

The coil has one single lateral boundary $\Gamma_{\text{Th},1}$, on which a convective boundary condition must be applied. The coil cryostat has been designed to maintain cooling conditions corresponding to an *effective* convective heat transfer coefficient of $h = 100$ W/m^{2}K. Theoretically, the convective coefficient depends on many parameters, such as the interface temperature, the channel geometry or the helium velocity, among others [40]. The grooves on the horizontal plates above and below the coil are designed to optimize the cooling conditions. In the following, the effective heat transfer coefficient is assumed uniform on the surface of the coil. Its impact on the thermal behaviour of the coil is discussed in Section 6.4.1. The numerical value of $h = 100$ W/m^{2}K is considered to be conservative, as Bottura [50] reported larger convective coefficients in his report on cable stability when using liquid helium as a coolant.
In the coil, the volumetric heat source is

$$q_{\text{s}} = q_{\text{hys}} + q_{\text{c}}, \tag{5.3}$$

with q_{hys} the macroscopic hysteresis loss and q_{c} the inter-filament coupling loss, respectively given by Eq. (3.65) and Eq. (3.71). No Neumann boundary conditions and no Dirichlet boundary conditions are considered in the weak formulation of the coil domain. Hence, the thermal weak formulation only involves transient conduction, convective heat transfer and volumetric heat generation.

Vessel thermal domain

A similar convective boundary condition is applied to the inner boundary of the helium vessel, while a radiative boundary condition is applied to its outer boundary. The radiative heat flux is incoming from a radiation screen, which is cooled down with liquid nitrogen at a temperature of $T_{\text{sur}} = 77$ K. The surface of the helium vessel has been treated so that its emissivity can be assumed to be $\varepsilon_R = 0.025$ in first approximation.
In the vessel, the volumetric heat source is

$$q_{\text{s}} = q_{\text{j}}, \tag{5.4}$$

with q_{j} the Joule loss given by Eq. (3.55). As for the coil, the helium vessel domain only involves Robin boundary conditions.

Periodic boundary conditions

As one quarter of the bottom part of the cyclotron is modelled in this study, a specific boundary condition must be applied to the planes Γ_{xy} and Γ_{yz} introduced in Chapter 4. The temperature being a scalar quantity, the periodic boundary condition simply reads

$$T(\underbrace{0, y, z}_{\in \Gamma_{yz}}) = T(\underbrace{-z, y, 0}_{\in \Gamma_{xy}}), \tag{5.5}$$

with $\boldsymbol{x} = (0, y, z) \in \Gamma_{yz}$. This periodicity condition is applied to the corresponding boundaries of the two thermal sub-domains.

5.3 Material properties

For solving the thermal problem as stated in this study, three material properties are required: the thermal conductivity κ, the density ρ_V and the specific heat c_p. The effective thermal properties of the homogenized coil are derived from an equivalent model of the conductor. The numerical values of all mentioned properties are taken from the National Institute of Standards and Technology (NIST) database [51] and are gathered in Appendix B.2.

5.3.1 Coil effective thermal properties

The coil is made of 1344 conductor turns. The conductor cross-section has been described in Fig. 3.7. In this section, the Nb-Ti filling factor of the cable is neglected. Only the copper channel and the fibreglass insulation are considered here. Neglecting Nb-Ti, their respective filling factors are $\lambda_{\text{Cu}} = 0.72$ and $\lambda_{\text{fg}} = 0.28$. Let us respectively denote by ρ_{Cu} [kg/m^3] and ρ_{fg} [kg/m^3] the densities of copper and fibreglass. For respecting mass conservation, the effective density ρ_{eff} [kg/m^3] of the coil must satisfy

$$\rho_{\text{eff}} = \lambda_{\text{Cu}}\rho_{\text{Cu}} + \lambda_{\text{fg}}\rho_{\text{fg}}. \tag{5.6}$$

Similarly, the internal energy of the homogenized coil must be equivalent to the internal energy of its components. Considering the case of an homogeneous temperature T and denoting by V [m^3] the total coil volume, by V_{Cu} [m^3] and V_{fg} [m^3] the total copper and total fibreglass volumes, the effective specific heat $c_{p,\text{eff}}$ [J/(kg K)] must satisfy

$$V\rho_{\text{eff}}c_{p,\text{eff}}T = V_{\text{Cu}}\rho_{\text{Cu}}c_{p,\text{Cu}}T + V_{\text{fg}}\rho_{\text{fg}}c_{p,\text{fg}}T \quad \Rightarrow \quad c_{p,\text{eff}} = \frac{\lambda_{\text{Cu}}\rho_{\text{Cu}}c_{p,\text{Cu}} + \lambda_{\text{fg}}\rho_{\text{fg}}c_{p,\text{fg}}}{\rho_{\text{eff}}}. \tag{5.7}$$

For deriving the effective thermal conductivity tensor of the coil, let us consider a simplified rectangular cross-section of one conductor as illustrated in Fig. 5.5. Moreover, as the radius of the coil ($\gtrsim$ 2 m) is much larger than the dimensions of the conductor, the conductor radius of curvature is neglected. Copper is assumed isotropic with conductivity κ_{Cu} [W/(m K)], while fibreglass is anisotropic as its thermal conductivity $\kappa_{\text{fg,w}}$ [W/(m K)] along the cable $\hat{\boldsymbol{\eta}}_3$-axis (warp direction) is larger than in the perpendicular (normal) direction $\kappa_{\text{fg,n}}$ [W/(m K)] [51].
Let us first derive the conductor conductivity tensor in the local system of axis shown in Fig. 5.5. Considering a steady-state configuration without heat generation, the heat rate q [W] through a wall of thickness t_{w} [m], cross-section A_{w} [m^2] and thermal conductivity κ_{w} [W/m K], submitted to a temperature difference ΔT [K], is

$$q = \frac{\kappa_{\text{w}}A_{\text{w}}}{t_{\text{w}}}\Delta T = \frac{\Delta T}{R}, \tag{5.8}$$

with R [K/W] the thermal resistance of the plane wall, concept introduced in [40] for studying composite materials. Working with resistances allows to tackle the problem using electrical circuits modelling. The equivalent resistive circuits of the conductor along its $\hat{\boldsymbol{\eta}}_1$-axis and its $\hat{\boldsymbol{\eta}}_2$-axis are shown in Fig. 5.5, with the per-unit-length thermal resistances:

$$\begin{aligned} R'_{\text{fg,10}} &= \frac{t_{\text{fg}}}{\kappa_{\text{fg,n}}(h_{\text{ch}} + 2t_{\text{fg}})}, \quad R'_{\text{fg,11}} = \frac{w_{\text{ch}}}{\kappa_{\text{fg,n}}t_{\text{fg}}}, \quad R'_{\text{Cu,1}} = \frac{w_{\text{ch}}}{\kappa_{\text{Cu}}h_{\text{ch}}}, \\ R'_{\text{fg,20}} &= \frac{t_{\text{fg}}}{\kappa_{\text{fg,n}}(w_{\text{ch}} + 2t_{\text{fg}})}, \quad R'_{\text{fg,21}} = \frac{h_{\text{ch}}}{\kappa_{\text{fg,n}}t_{\text{fg}}}, \quad R'_{\text{Cu,2}} = \frac{h_{\text{ch}}}{\kappa_{\text{Cu}}w_{\text{ch}}}. \end{aligned} \tag{5.9}$$

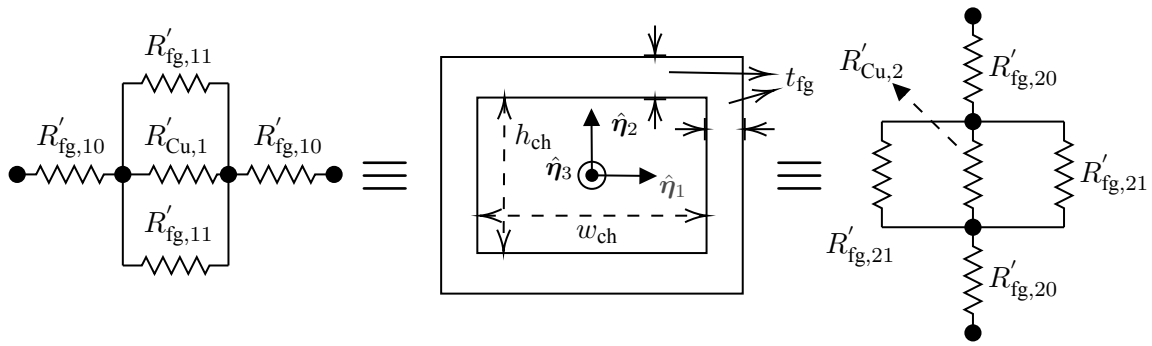

Figure 5.5: Simplified conductor cross-section with local coordinate system and equivalent thermal resistive circuits along the $\hat{\boldsymbol{\eta}}_1$-axis and the $\hat{\boldsymbol{\eta}}_2$-axis.

The effective thermal conductivities κ_1 [W/(m K)] and κ_2 [W/(m K)] along the $\hat{\boldsymbol{\eta}}_1$-axis and the $\hat{\boldsymbol{\eta}}_2$-axis can thus be derived as

$$\begin{aligned}\kappa_1 &= \frac{w_{\text{ch}} + 2t_{\text{fg}}}{R'_{\text{eq},1}(h_{\text{ch}} + 2t_{\text{fg}})} = \frac{w_{\text{ch}} + 2t_{\text{fg}}}{h_{\text{ch}} + 2t_{\text{fg}}} \left[2R'_{\text{fg,10}} + \left(\frac{1}{R'_{\text{Cu,1}}} + \frac{2}{R'_{\text{fg,11}}} \right)^{-1} \right]^{-1}, \\ \kappa_2 &= \frac{h_{\text{ch}} + 2t_{\text{fg}}}{R'_{\text{eq},2}(w_{\text{ch}} + 2t_{\text{fg}})} = \frac{h_{\text{ch}} + 2t_{\text{fg}}}{w_{\text{ch}} + 2t_{\text{fg}}} \left[2R'_{\text{fg,20}} + \left(\frac{1}{R'_{\text{Cu,2}}} + \frac{2}{R'_{\text{fg,21}}} \right)^{-1} \right]^{-1}.\end{aligned} \tag{5.10}$$

Along the $\hat{\boldsymbol{\eta}}_3$-axis, a similar development yields two thermal resistances in parallel and the effective thermal conductivity κ_3 [W/(m K)] is given by

$$\kappa_3 = \frac{(w_{\text{ch}} + 2t_{\text{fg}})(h_{\text{ch}} + 2t_{\text{fg}})}{\kappa_{\text{fg,w}} 2t_{\text{fg}}(h_{\text{ch}} + w_{\text{ch}} + 2t_{\text{fg}}) + \kappa_{\text{Cu}} h_{\text{ch}} w_{\text{ch}}}, \tag{5.11}$$

taking this time the warp thermal conductivity of fibreglass into account. The temperature dependence of the effective thermal conductivity is quantified in Appendix B.2 and represented in Fig. 5.6. As highlighted, the conductivity is the largest along the axis of the conductor. Such a behaviour is expected as copper is much more thermally conductive than fibreglass. The electrical insulating layer around the conductors also acts as a thermal insulator. Consequently, the transverse effective conductivity of the coil is mostly dictated by the fibreglass normal conductivity.

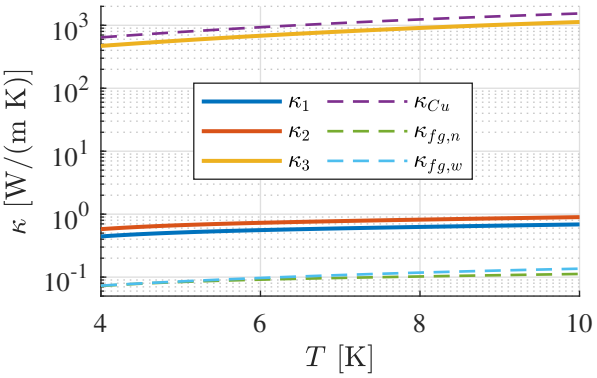

Figure 5.6: Temperature dependence of the coil effective thermal conductivity, together with $\kappa_{\text{Cu}}(T)$, $\kappa_{\text{fg,n}}(T)$ and $\kappa_{\text{fg,w}}(T)$.

From a macroscopic point of view, the local coordinate system of the conductor corresponds to the cylindrical coordinate system, so that the anisotropic effective thermal conductivity tensor is

$$\boldsymbol{\kappa} = \begin{pmatrix} \kappa_r & 0 & 0 \\ 0 & \kappa_y & 0 \\ 0 & 0 & \kappa_\theta \end{pmatrix} = \begin{pmatrix} \kappa_1 & 0 & 0 \\ 0 & \kappa_2 & 0 \\ 0 & 0 & \kappa_3 \end{pmatrix}. \tag{5.12}$$

Numerically, the conductivity tensor is implemented in Cartesian coordinates as

$$\boldsymbol{\kappa} = \begin{pmatrix} \kappa_x & 0 & 0 \\ 0 & \kappa_y & 0 \\ 0 & 0 & \kappa_z \end{pmatrix} = \begin{pmatrix} \kappa_r \cos^2(\theta) + \kappa_\theta \sin^2(\theta) & 0 & (\kappa_r - \kappa_\theta)\cos(\theta)\sin(\theta) \\ 0 & \kappa_y & 0 \\ (\kappa_r - \kappa_\theta)\cos(\theta)\sin(\theta) & 0 & \kappa_r \sin^2(\theta) + \kappa_\theta \cos^2(\theta) \end{pmatrix}. \tag{5.13}$$

The change of coordinate system is discussed in Appendix A.6. It is worth noting that due to the anisotropy of the homogenized coil, some non-diagonal terms appear in the expression of the thermal conductivity tensor.

5.3.2 Vessel thermal properties

All thermal properties of the vessel and their thermal dependence are gathered in Appendix B.2.

5.4 Numerical implementation

In this section, the numerical implementation of the thermal weak formulation and the corresponding nonlinear procedure is briefly discussed.

Discretization

The main unknown of the thermal problem is temperature. Numerically, the temperature field is approximated by a linear combination of nodal shape functions and the corresponding DOFs are thus associated to the temperature at the different nodes of the mesh. The time integration of the spatially discretized formulation is performed using a backward Euler method as for the magnetodynamic resolution.

Nonlinear procedure

As the thermal properties involved in the weak formulation depend on temperature, the discretized system is nonlinear. The iterative procedure used for numerical computations is the Picard algorithm, which was introduced in Section 4.4. This iterative procedure is performed at each time step until the relative norm of the thermal residual is lower than $\varepsilon_{\text{rel,th}} = 10^{-10}$. The convergence of the thermal iterative method was observed to be more regular and much faster compared to the magnetodynamic method. This is expected as the nonlinearity of the thermal properties is less pronounced than that observed for ferromagnets or superconductors. To avoid unnecessary iterations when the relative residual reaches an asymptotic value, the maximal number of thermal iterations is set to 10.

5.5 Thermal time constant

The magnetic time constant of the cyclotron has been characterized in Chapter 4. Let us now briefly discuss the thermal time constant of the coil. Three phenomena are at play: heat generation, convection and thermal diffusion through conduction. The heat exchange with liquid helium results from a balance between convection and conduction along the $\hat{\boldsymbol{\eta}}_1$ and $\hat{\boldsymbol{\eta}}_2$ axes of the coil. At T_{he}, $\kappa_1 = 0.46$ W/(m K) $\sim \kappa_2 = 0.6$ W/(m K) ~ 0.5 W/(m K). The Biot number of the coil is thus

$$Bi = \frac{hL_c}{\kappa} \sim 10, \tag{5.14}$$

with the characteristic length $L_c = 0.053$ m chosen as the ratio of the coil volume to its lateral surface. Such a large Biot number implies that spatial temperature variations inside the coil cannot be neglected. In that context, there is no direct analytical estimation for the thermal time constant [40]. Nevertheless, the thermal time constant τ_{th} [s] of the coil is estimated numerically by applying a step of volumetric heat source $q_{\text{s}} = 1$ W/m^3 in the whole volume of the coil $\Omega_{\text{th},1}$. The evolution of the coil internal energy is represented in Fig. 5.7. For clarity, the results do not involve any coupling with magnetodynamics for now. As can be observed, the convective coefficient has a significant

impact on the coil thermodynamics. Assuming an exponential behaviour, the thermal time constant is respectively given by $\tau_{\text{th}} = 16.85$ s, $\tau_{\text{th}} = 8.64$ s and $\tau_{\text{th}} = 7.85$ s for $h = \{10; 100; 1000\}$ W/m^{2}K. The thermal time constant seems to reach some asymptotic value for large Biot numbers. In that context, assuming the thermodynamics is mostly related to the balance between the conduction and the internal energy variation terms, the thermal time constant can be estimated from dimensional analysis as

$$\tau_{\text{th}} \sim \frac{\rho_{\text{eff}} c_{p,\text{eff}} L_c^2}{\kappa} \sim 10 \text{ s}, \tag{5.15}$$

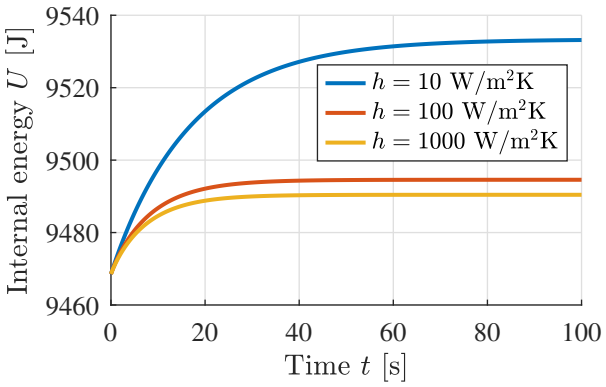

Figure 5.7: Evolution of the coil internal energy $U(t)$ after a step of $q_s = 1$ W/m^3 for various convective coefficients h. Results obtained with $s = 0.64$ and $\Delta t = 0.5$ s.

with $\kappa \sim 0.5$ W/(m K) as previously, $\rho_{\text{eff}} = 6950$ kg/m^3 and $c_{p,\text{eff}} = 0.267$ J/(kg K). The order of magnitude is very similar to the numerical results, which further validates the numerical implementation of the thermal problem.

Comment on numerical errors linked to the anisotropic conductivity tensor

The anisotropy of the conductor effective thermal conductivity tensor (Eq. (5.13)) is extremely pronounced. It introduces numerical errors, with excessive heat flux components along the azimuthal axis of the coil. It may be linked to the fact that the heat equation is satisfied weakly and not strongly. In the configuration of the last section, the heat source q_s is uniform throughout the coil. Since the coil is axisymmetric, the temperature field is expected to be independent of the azimuthal coordinate: $\partial_\theta T = 0$ and the 3D simulation should give the same results as the 2D axisymmetric solution. With the effective conductivity tensor as given in Eq. (5.13), the final internal energy in the coil is $U = 9480.5$ J in 3D, which is much lower than the 2D results. As has been observed by experimenting with the thermal model, a much finer spatial discretization is required to accurately model such an anisotropy. However, as the unstructured 3D mesh is shared between the magnetodynamic and the thermal solvers, the mesh size in the coil is on the order of centimeters and cannot be sufficiently refined. To avoid these numerical errors and to match the 2D results, the azimuthal conductivity is set to $\kappa_\theta^* = \kappa_r$. In this case the thermal conductivity is isotropic in the horizontal plane, but still anistropic with respect to the vertical axis.

Brief chapter conclusion

This chapter has described the thermal model, focusing on the thermal boundary conditions and the domain separation between the coil and the helium vessel. The effective thermal properties of the coil have also been derived and presented. The thermal time constant has been evaluated numerically and validated using dimensional analysis. As emphasized, the liquid helium cooling mechanism ensures a large Biot number regime, which will have a significant impact on the magnetothermal behaviour of the coil during ramp-up, as will be shown in Chapter 6.

CHAPTER 6

MAGNETOTHERMAL BEHAVIOUR DURING RAMP-UP

In this chapter, the magnetodynamic model described in Chapter 4 is coupled with the thermal model introduced in Chapter 5. The magnetothermal behaviour of the superconducting coil is characterized during ramp-up. First, the scheme used to couple the magnetic and thermal solvers numerically is presented and discussed. As explained in Section 3.5, hysteresis losses in the Nb-Ti filaments and inter-filament coupling losses in the copper matrix lead to heat generation inside the coil. The magnetothermal results are first discussed in the simplified axisymmetric geometry. Again, the reduced computational time allows some preliminary studies to be carried out while understanding the physical concepts involved. Results are then presented in the full three-dimensional geometry. The differences with respect to axisymmetric results are highlighted and their physical explanation is provided. Finally, several physical parameters are varied and their impact on the maximal temperature rise within the coil is assessed.

6.1 Magnetothermal coupling scheme

As emphasized in Chapter 4, the magnetic properties involved in the magnetodynamic formulation are almost independent of temperature in the considered temperature range. In this study, their temperature dependence is neglected. Consequently, the magnetodynamic resolution does not depend on the thermal resolution, resulting in a one-way coupling. Note that this reasoning is valid as long as the temperature increase in the coil does not lead to a quench event. Modelling a quench propagation phenomenon would require modelling the magnetothermal behaviour of the coil at the filament scale, which is beyond the scope of this work. The coupling scheme implemented in this study is shown in Fig. 6.1.
The magnetodynamic solver represented in the left part of Fig. 6.1 has been discussed in Chapter 4. At each time step, the volumetric heat source in the coil $\Omega_{\text{th},1}$ is computed locally, as a function of the magnetic flux density and its variation over time. The filamentary hysteresis loss also depends on the temperature through the critical current density $j_{\text{c}}(b,T)$. The thermal formulation allows the temperature in the coil to be retrieved from the hysteresis loss q_{hys} and the inter-filament coupling loss q_{c}. Similarly, the temperature can be computed in the helium vessel $\Omega_{\text{th},2}$, where the source term is the Joule loss q_{j}.

As shown in Chapter 4, the impact of the helium vessel in magnetodynamics is negligible. In the final implementation of the code, it is up to the user whether or not to include the vessel. In the first part of this chapter, the helium vessel is not included. It is specifically discussed in Section 6.2.3.

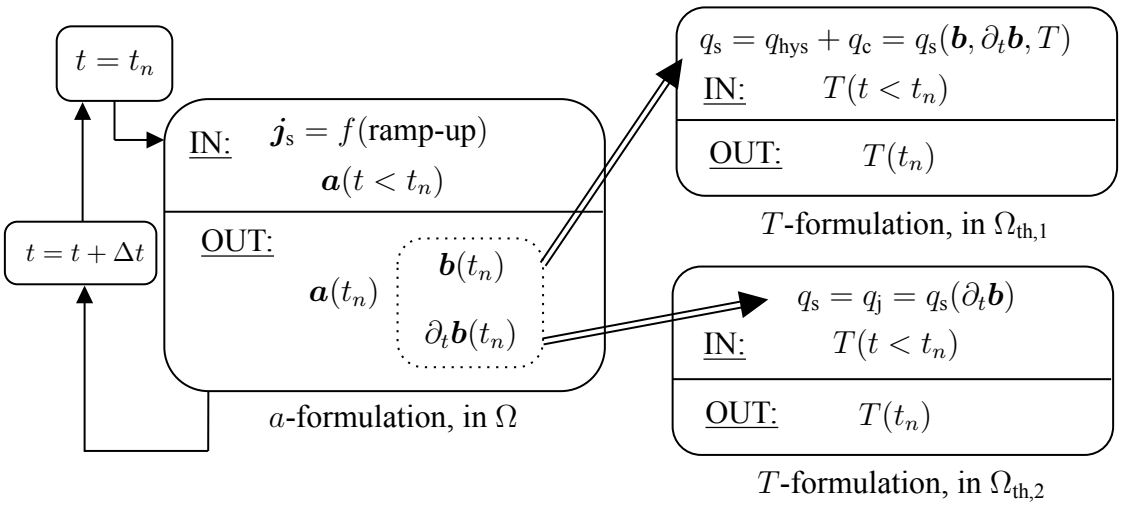

Figure 6.1: One time step of the magnetothermal coupling scheme implemented between the magnetodynamic solver in Ω and the two thermal solvers in $\Omega_{th,1}$ and $\Omega_{th,2}$. All solvers are nonlinear and each system is solved iteratively at all time steps.

6.2 Results in the axisymmetric geometry

As a reminder, the axisymmetric geometry neglects the spiralized poles and the extraction holes. Nevertheless, it allows to perform some preliminary study. First, the choices for the time step and the global mesh size are discussed.

6.2.1 Sensitivity to numerical parameters

Impact of the time step

The evolution of the mean temperature increase ΔT_m [K] during ramp-up is represented in Fig. 6.2 for various time steps. It is computed as $\Delta T_m = T_m - T_{\text{He}}$, with T_m [K] the mean temperature in the coil. For now, let us focus on the impact of the time step on the results. The shape of the curves and the corresponding order of magnitude are discussed later. As highlighted, the mean temperature increase is underestimated for large time steps. As observed in Chapter 4, the time step should not exceed $\Delta t = 100$ s, for which the relative difference in maximal mean temperature increase is 1.2 % higher than that calculated for $\Delta t = 10$ s and 1.5 % higher than that calculated for $\Delta t = 1$ s. For clarity, the curves for $\Delta t < 10$ s are not shown in Fig. 6.2 as they are all similar. A time step of $\Delta t = 100$ s is adopted for all 3D simulations, while a time step of $\Delta t = 20$ s is used for the following axisymmetric simulations. It corresponds to a total CPU time of 189 s and a total number of 1861 nonlinear iterations.

Impact of the mesh size

Although the effect of the global mesh size has been investigated in Chapter 4, let us check the convergence of thermal results with mesh refinement. As highlighted in Fig. 6.3, the mean temperature increase in the coil becomes slightly larger as the mesh is refined. Such a behaviour can be explained by the fact that the magnetic energy within the whole domain increases as the global mesh size is refined (cf. Section 4.7.1). Consequently, the average flux density and its time variation are also slightly increased, leading to greater heat dissipation and temperature rise in the coil. The relative difference in the maximal mean temperature increase compared to $s = 0.012$ is summarized in Tab. 6.1. The thermal results do converge as the mesh is refined, at the expense of CPU time. As the computing time is reasonable in 2D, a mesh size of $s = 0.12$ is adopted in next section.

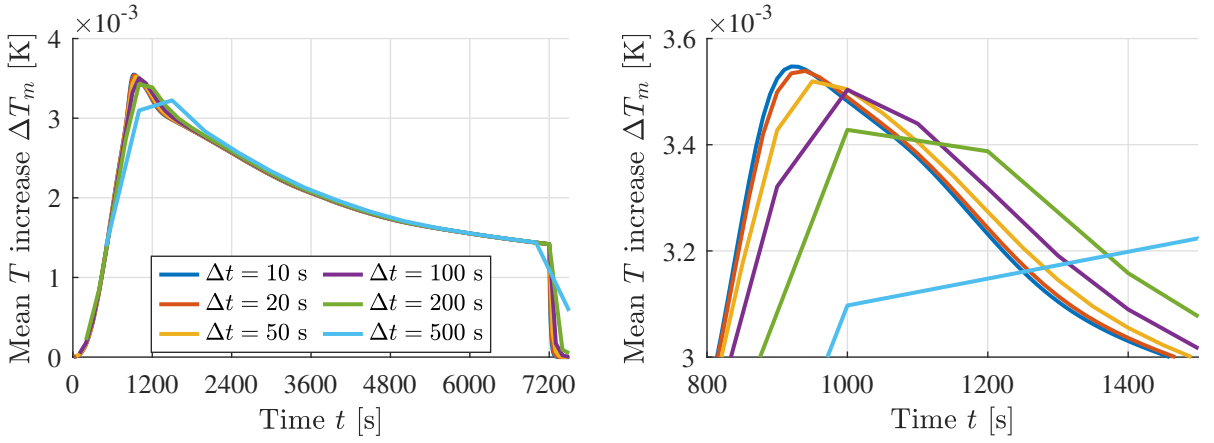

Figure 6.2: Evolution of the mean temperature increase ΔT_m in the coil for various time steps. (a) global view, (b) focus on the peak around $t \sim 900$ s. Global mesh size $s = 0.64$.

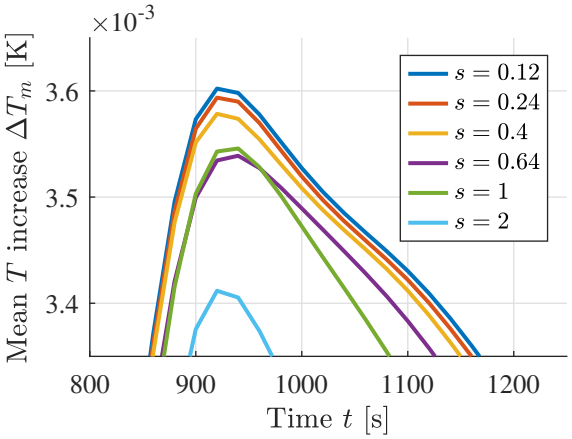

Figure 6.3: Evolution of the mean temperature increase ΔT_m in the coil for various mesh sizes s. Focus on the peak around $t \sim 900$ s. $\Delta t = 20$ s.

s	$\max(\Delta T_m)$ [K]	$\varepsilon_{\text{rel},s=0.12}$	T_{CPU} [s]
0.12	0.00360	-	5980
0.24	0.00359	0.23 %	1353
0.40	0.00358	0.65 %	471
0.64	0.00354	1.75 %	189
1	0.00354	1.56 %	88
2	0.00341	5.28 %	32

Table 6.1: Maximal mean temperature increase ΔT_m in the coil for various mesh sizes s, corresponding relative difference compared to $s = 0.12$ and total CPU time T_{CPU}. $\Delta t = 20$ s.

6.2.2 Main results

Before going further, please note that all global quantities such as losses (in [W]) are expressed for the complete cyclotron, rather than just one half (or one eighth in 3D).
The temperature evolution at different points of the coil is shown in Fig. 6.4, along with the maximal temperature observed in the coil. The evolution of the mean temperature has already been shown in Fig. 6.2. As highlighted, the temperature is larger in the left (internal) part of the coil, which is closer to the center of the cyclotron. The temperature is the lowest in the bottom right part, which is expected as the flux density is also the lowest in this area (as observed in Fig. 4.12). Consequently, the flux density variation and corresponding heat dissipation are relatively lower in this region. Remarkably, all temperature curves exhibit some very short quasi-quadratic rise before increasing quasi-linearly until $t = 900$ s. The temperature then reaches its local maximal before decreasing smoothly. At $t = 7200$ s, the nominal current is reached and the magnetothermal behaviour of the cyclotron is rapidly stabilized. The time scale of such a stabilisation process is similar to τ_{th}.
Moreover, the temperature increase in the coil is extremely low: $\Delta T_{\text{max}} = 0.0084$ K. It highlights the cooling efficiency of liquid helium. Note that ΔT_{max} is still much larger than the discretization

error of $\sim 10^{-5}$ K deduced from Tab. 6.1. The expected order of magnitude of the temperature increase is discussed at the end of this section.

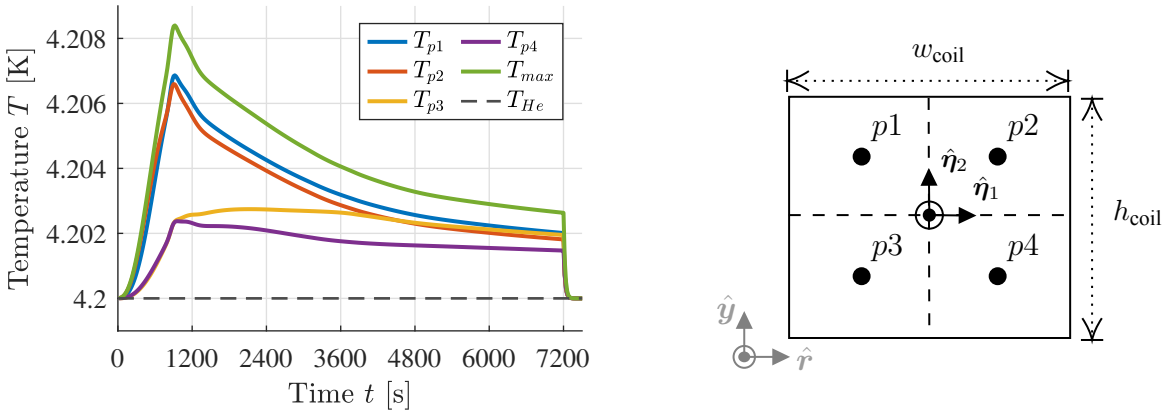

Figure 6.4: Evolution of the temperature T at different points of the coil (represented at right). $\Delta t = 20$ s, $s = 0.12$.

To understand the shape of the temperature curves, the evolution of losses in the coil is discussed. The integrated filamentary hysteresis loss and inter-filament coupling loss are respectively denoted by Q_{hys} [W] and Q_{c} [W]. The corresponding curves are represented in Fig. 6.5. Hysteresis losses are nearly 1000 times larger than coupling losses. This ratio of hysteresis loss to coupling loss is confirmed when applying basic dimensional analysis as emphasized further at the end of this section. The main conclusion to be drawn here is that the hysteresis loss dictates the thermal behaviour of the coil. The striking similarity between the temperature curves and the hysteresis loss curve further reinforces this conclusion. The hysteresis loss also exhibits a quadratic evolution at first before increasing linearly until reaching its peak around $t = 900$ s. Most losses occur in the left part of the coil, as highlighted in Fig. 6.6(a). The losses are larger because the corresponding flux density variations are greater as shown in Fig. 6.6(b). Note that the coil flux density almost evolves linearly over time. Remarkably, the flux density in the bottom right part of the coil remains very low, which can be explained by the fact that the central region of low field moves downward over time until reaching the bottom right part of the coil as shown in Fig. 4.12. The corresponding hysteresis loss is particularly small as the flux density variation is limited.

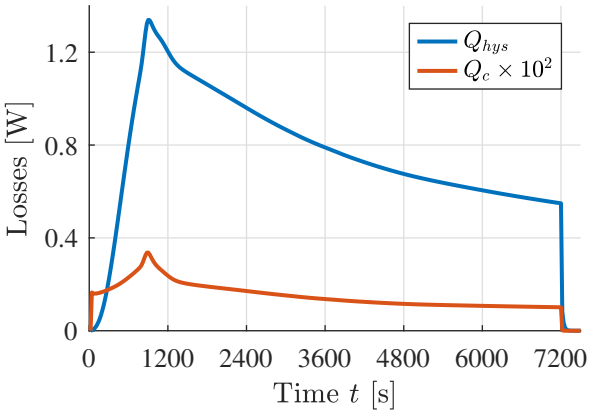

Figure 6.5: Evolution of integrated losses inside the coil. $\Delta t = 20$ s, $s = 0.12$.

The particular shape of the local hysteresis loss curves can be explained by discussing Eq. (3.61):

$$q_{\text{hys},1} = \frac{2 j_{\text{c}}\, d_f\, b^2\, /3\pi}{j_{\text{c}}^2\, \mu_0^2\, d_f^2\, /32 + b^2}\, \dot{b},$$

which has been derived as an interpolation between the low field regime (Eq. (3.60)) and the high field regime (Eq. (3.59)). It is a strongly nonlinear equation in the flux density, as it is a rational function of b, while the critical current density j_{c} also depends on b through Bottura's relationship. The corresponding single filament hysteresis loss is shown in Fig. 6.7, where it has been normalized by the flux density variation to highlight the effect of the flux density norm on the loss amplitude. As a consequence of Eq. (3.60), the hysteresis loss evolves quadratically in low field.

As the filament becomes more penetrated, the hysteresis loss tends towards Eq. (3.59), which is a decreasing function of the flux density through $j_c(b)$. Since the critical current density diverges at low field, Eq. (3.59) also diverges, highlighting the need to derive a more refined approximation in weak penetration, as done in Appendix A.7. As a global consequence of this nonlinear behaviour of the hysteresis loss, the normalized loss is maximal around $b \sim 0.38$ T. Quite remarkably, the norm of the flux density in the left part of the coil reaches this particular value between $t \sim 750$ s and $t \sim 1000$ s, which explains the peak in hysteresis loss around $t \sim 900$ s.
Furthermore, Fig. 6.7 illustrates the quadratic behaviour of the hysteresis loss at low field and thus the quasi-quadratic evolution of the global hysteresis loss at the beginning of the ramp-up process. Since the time scale of the ramp-up is much larger than the thermal time constant τ_{th}, the temperature in the coil also follows the same shape as the heat source in the form of hysteresis losses. The main conclusion here is the central role played by filament hysteresis losses in the thermal behaviour of the coil. In Chapter 7, hysteresis losses are studied in detail using a single filament numerical model and the validity of the underlying assumptions in Eq. (3.61) is discussed.

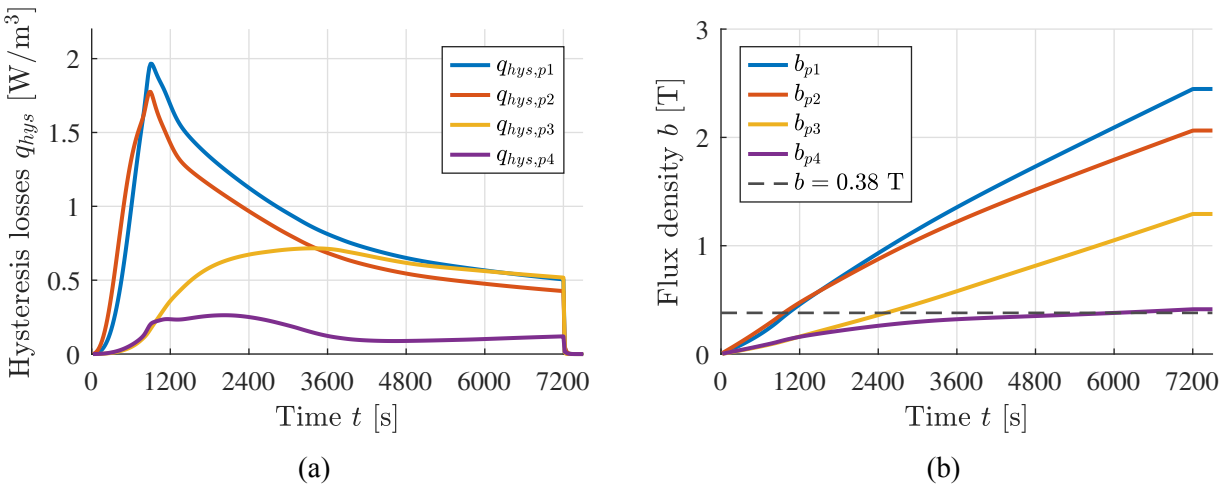

(a) (b)

Figure 6.6: Evolution of (a) the local filamentary hysteresis loss q_{hys} at different points of the coil and (b) corresponding flux density norm b. The position of the points is shown in Fig. 6.4. $\Delta t = 20$ s, $s = 0.12$.

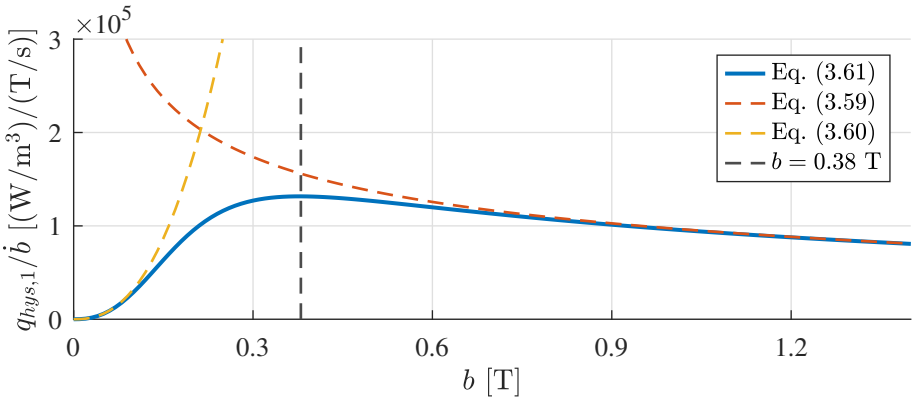

Figure 6.7: Theoretical single filament hysteresis loss $q_{\text{hys,1}}$ normalized by the flux density variation $\dot{b}$, as a function of the flux density b at $T_{\text{He}} = 4.2$ K. The interpolated Eq. (3.61) implemented in the code is shown along the weakly penetrated (Eq. (3.60)) and the fully penetrated regimes (Eq. (3.59)).

The temperature field is shown in Fig. 6.8. The color scale is adapted to the different instants. As observed, the hottest point in the coil moves from the bottom left upward, then moves towards the center of the coil. The maximal temperature is $T_{\text{max}} = 4.2084$ K at $t = 900$ s. The temperature

increase in the coil is very small and there is no risk of a quench. As represented in Fig. 6.9, the heat flux is always directed from the hot region towards the boundary of the coil, where convective heat transfer takes place. The heat flux is maximal at $t = 900$ s, its norm being $q = 0.111$ W/m^2 corresponding to a peak coil surface temperature of $T - T_{\text{He}} = 0.0011$ K. The temperature difference in the coil itself is much larger than in the liquid helium, which is a direct consequence of the large Biot number regime.

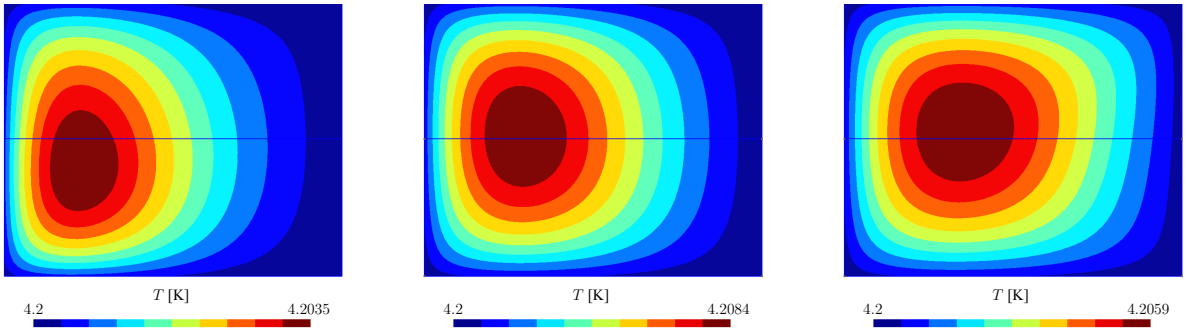

(a) $t = 500$ s. (b) $t = 900$ s. (c) $t = 2000$ s.

Figure 6.8: Temperature T [K] in the conductor at different instants. $\Delta t = 20$ s, $s = 0.12$. For clarity, the color scale has been adapted to each instant.

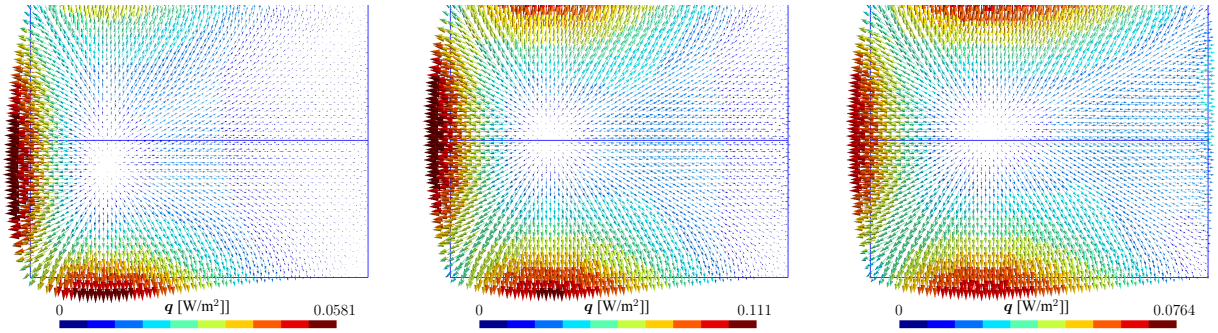

(a) $t = 500$ s. (b) $t = 900$ s. (c) $t = 2000$ s.

Figure 6.9: Heat flux $\boldsymbol{q}$ [W/m^2] in the conductor at different instants. $\Delta t = 20$ s, $s = 0.12$. For clarity, the color scale has been adapted to each instant.

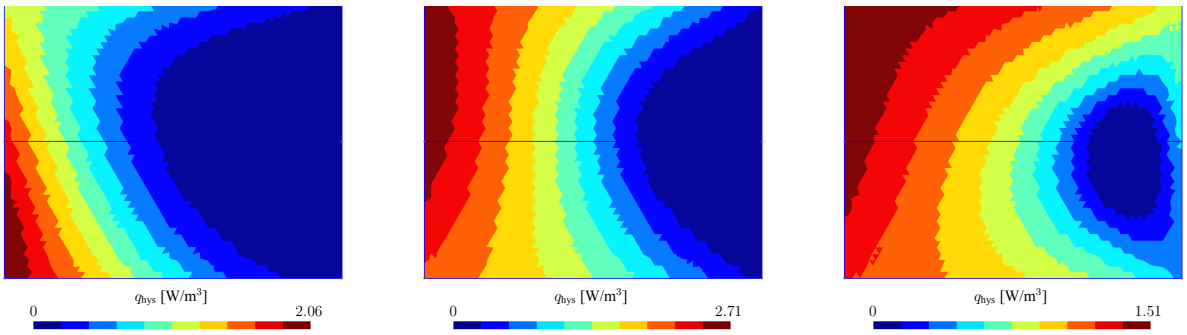

(a) $t = 500$ s. (b) $t = 900$ s. (c) $t = 2000$ s.

Figure 6.10: Filament hysteresis loss q_{hys} [W/m^3] in the conductor at different instants. $\Delta t = 20$ s, $s = 0.12$. For clarity, the color scale has been adapted to each instant.

The local hysteresis loss is represented in Fig. 6.10. At first, the loss mostly occurs in the bottom left part of the coil. Once again, the loss is maximal at $t = 900$ s. In the second part of the ramp-up process, the loss mainly occurs in the top left part of the coil. It is directly linked to the flux density evolution in the coil discussed in Chapter 4 and shown in Fig. 4.12.
The temperature profiles along horizontal and vertical cuts is shown in Fig. 6.11, highlighting the larger temperature difference $T - T_{\text{He}}$ within the coil compared to the temperature difference between the surface of the coil and the liquid helium. Once again, such a behaviour is explained by the cooling efficiency of liquid helium and a corresponding large Biot number.

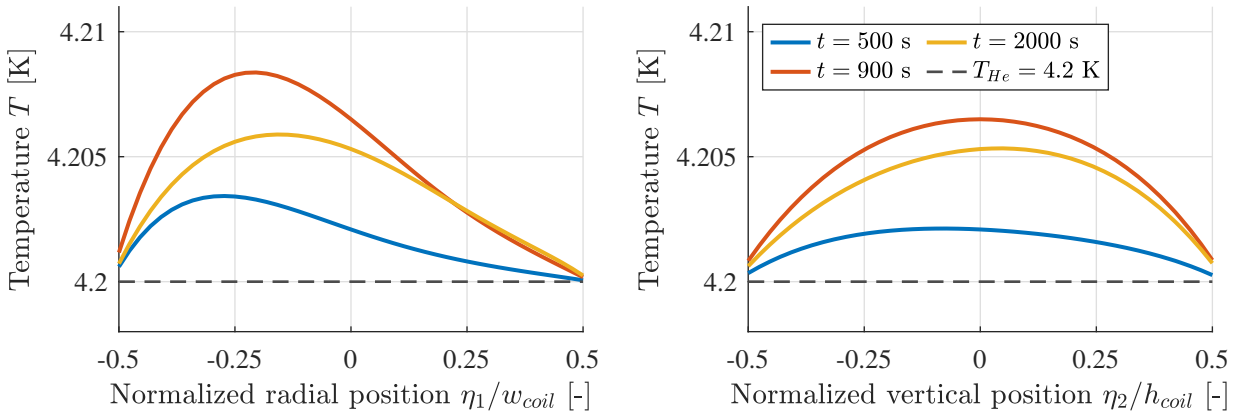

(a) (b)

Figure 6.11: Temperature profiles at different instants (a) along the radial axis of the coil and (b) along its vertical axis. The cuts and the axes are shown in Fig. 6.4(b). $\Delta t = 20$ s, $s = 0.12$.

Orders of magnitude

As observed, the maximal temperature increase in the coil is $T_{\text{max}} = 0.0084$ K. Let us estimate if such an increase can be expected from dimensional analysis. In a regime characterized by a large Biot number, the temperature variations are most pronounced within the coil itself as mentioned previously. Hence, the total temperature difference in the coil can be roughly estimated as $\Delta T = T - T_{\text{He}}$, and it is primarily influenced by the diffusion mechanism within the coil. Indeed, the limit $h \to \infty$ simply corresponds to a Dirichlet condition $T = T_{\text{He}}$ on the surface of the coil. As the time scale of the ramp-up process is much larger than the thermal time constant τ_{th}, a steady-state balance between conduction and heat source is assumed. Using again $\kappa \sim 0.5$ W/(m K), it comes from dimensional analysis:

$$q_{\text{s}} \sim \frac{\kappa \Delta T}{L_c^2} \Rightarrow \Delta T \sim \frac{q_{\text{s}} L_c^2}{\kappa} \sim 0.01 \text{ K}, \tag{6.1}$$

assuming the same characteristic length $L_c = 0.053$ m as in Chapter 5 and a heat source of $q_{\text{s}} = 2$ W/m^3. The order of magnitude is similar to what has been obtained numerically.
Similarly, let us check the order of magnitude of the filamentary hysteresis loss and inter-filament coupling loss. Let us apply dimensional analysis on Eq. (3.59) and Eq. (3.71) respectively. Assuming $j_{\text{c}} \sim 5 \times 10^9$ A/m^2 and $\dot{b} \sim 2$ T$/T_{\text{up}}$, it comes (all quantities expressed in SI units):

$$q_{\text{hys}} \sim \lambda_{\text{SC}} d_f j_{\text{c}} \, \dot{b} \sim 0.03 \cdot 5 \times 10^{-5} \cdot 5 \times 10^9 \cdot 2/7200 \sim 2 \text{ W/m}^3, \tag{6.2}$$

$$q_{\text{c}} \sim \frac{\lambda_{\text{SC}}}{\lambda_{\text{w}}} \frac{1}{\rho_{\text{eff}}} \left(\frac{p_L}{2\pi} \right)^2 \dot{b}^2 \sim 6.67 \times 10^{-2} \cdot 2 \times 10^9 \cdot (10^{-2})^2 \cdot (2/7200)^2 \sim 10^{-3} \text{ W/m}^3, \tag{6.3}$$

which is also similar to the numerical results. The orders of magnitude retrieved with the magnetothermal model are thus in good agreement with dimensional analysis, which further validates the results and the previous physical interpretation.

Finally, let us check if the coil has crossed the critical surface, in which case Nb-Ti filaments would have gone out of the superconducting state. During the whole ramp-up process, the minimal local critical current density $j_c(b,T)$ (taking b and T contributions into account) is $j_c = 3917$ A/mm^2 at $t = 7200$ s, which corresponds to the end of the ramp-up procedure. The impact of temperature on j_c is negligible with respect to the impact of the flux density. The corresponding transport current ratio is $i = I_t/I_c = \|\boldsymbol{j}_t\|/j_c = 0.281$ and the coil effectively remains in the superconducting state.

6.2.3 Modelling the helium vessel

In this section, the helium vessel $\Omega_{th,2}$ is included in the thermal resolution. The two different heat sources act on the vessel, namely the Joule losses and the radiation incoming from the radiation shield, are shown in Fig. 6.12. The radiative heat rate remains stable at $Q_{rad} \sim 1.39$ W. The Joule loss Q_j is maximal at the beginning of the ramp-up process (around $t \sim 100$ s) and then quickly decreases below the radiative heat rate. Consequently, its impact on the temperature field inside the vessel rapidly becomes negligible.

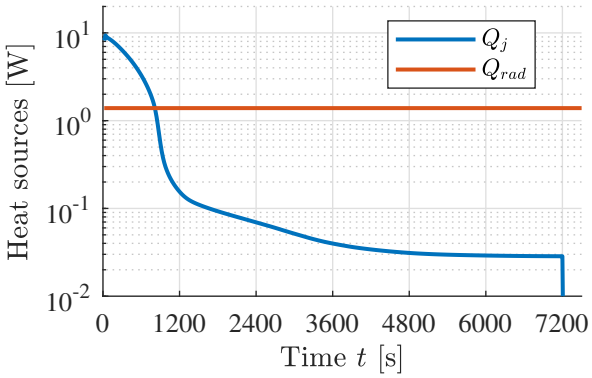

Figure 6.12: Evolution of integrated Joule losses Q_j and radiative heat rate Q_{rad} in the helium vessel. $\Delta t = 20$ s, $s = 0.12$.

The temperature field is shown in Fig. 6.13(a-b). As observed, the maximal temperature in the vessel is $T = 4.235$ K. The temperature increase is small because the liquid helium cooling is very efficient on the inner boundary of the vessel. The temperature field at $t = 2000$ s is very similar to the steady-state temperature field as it is mainly determined by the radiative heat rate. The steady-state maximal temperature in the vessel is $T = 4.209$ K. As highlighted in Fig. 6.13(c), the Joule dissipation is larger in the left part of the vessel, which can be explained by the larger flux density variation as was already the case for the hysteresis losses in the coil.

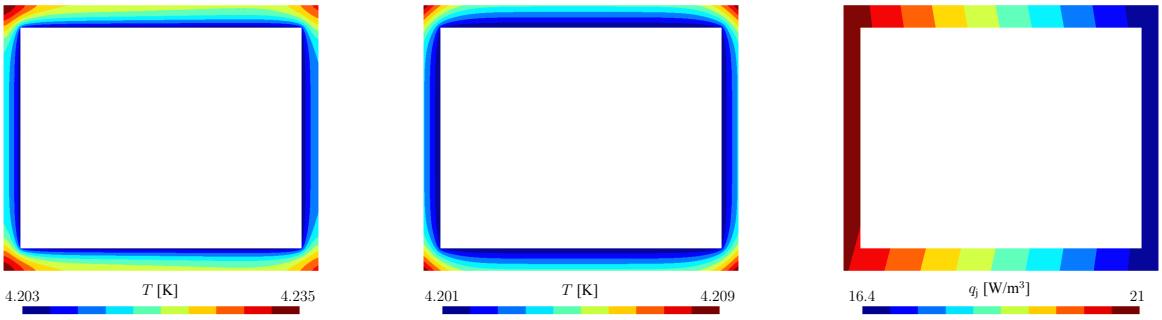

(a) $t = 100$ s. (b) $t = 2000$ s. (c) $t = 100$ s.

Figure 6.13: Temperature T field in the helium vessel at (a) $t = 100$ s and (b) $t = 2000$ s, as well as the local Joule loss q_j at $t = 100$ s. $\Delta t = 20$ s, $s = 0.12$.

As already highlighted in Section 4.7.4, the impact of the helium vessel on the magnetic energy in the coil is negligible. As a consequence, the effect of the helium vessel eddy currents on the flux variation within the composite conductor is also negligible. In fact, the maximal temperature increase in the coil during ramp-up is $T_{max} - T_{He} = 0.00843$ K with the vessel included, to be compared to 0.00840 K without the vessel. The relative difference of 0.36 % is not significant. Consequently, the helium vessel is neglected in the next parts of the study. Nevertheless, the helium vessel is still implemented in the final version of the code (also in 3D) and the user can still choose to include it before starting the full magnetothermal resolution.

6.3 Results in the three-dimensional geometry

The aim of this section is to discuss the magnetothermal behaviour of the coil in three dimensions. The geometry considered is the complete geometry, including the off-center holes, but excluding the helium vessel. The results presented in Fig. 6.14 are obtained from a magnetothermal simulation with global mesh size $s = 0.84$ and time step $\Delta t = 100$ s, for a total CPU time of 23 hours. Note that the 2D axisymmetric results are slightly different from those presented in the previous section as the numerical parameters have been set to $s = 0.84$ and $\Delta t = 100$ s to allow comparison with the 3D results.
As can be seen in Fig. 6.14(a), the mean and maximal temperature curves in the coil are smoothed out compared to the 2D axisymmetric resolution. The maximal temperature is now reached around $t \sim 1200$ s. On the other hand, the maximal temperature in the 3D coil in the intermediate regime is higher than that obtained in 2D. Nevertheless, the maximal temperature increase is similar as it is $\Delta T_{\text{max}} = 0.0074$ K in 3D and $\Delta T_{\text{max}} = 0.0083$ K in 2D with the considered set of numerical parameters. Consequently, working in the axisymmetric geometry provides a conservative approach of studying the magnetothermal behaviour, as the predicted maximal temperature increase is slightly overestimated. As discussed in the previous section, the temperature increase is mainly caused by the hysteresis loss in the Nb-Ti filaments. As observed in Fig. 6.14(b), the integrated hysteresis loss has also been smoothed out compared to axisymmetric results, which explains the shape of the temperature curves.

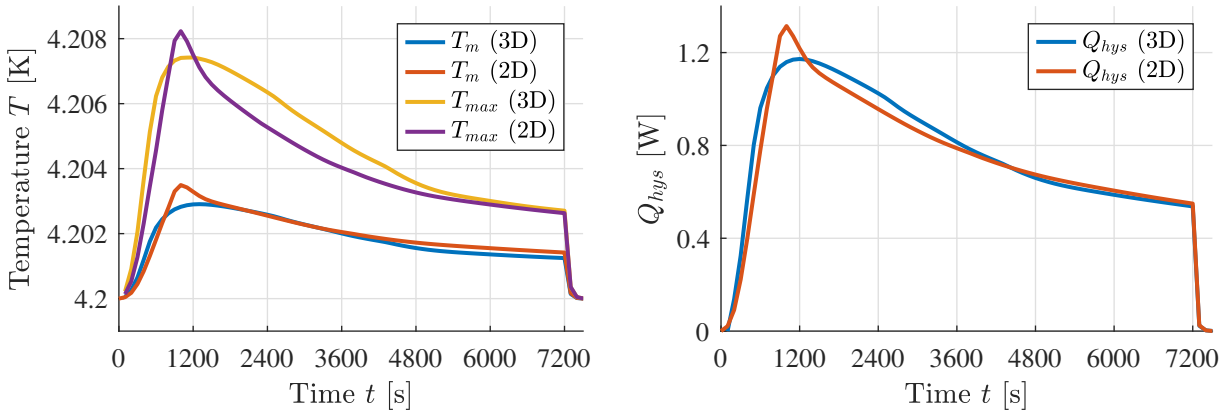

(a) (b)

Figure 6.14: Evolution of (a) the mean T_m and maximal T_{max} temperatures in the coil and (b) integrated hysteresis loss Q_{hys}. 3D results are compared to axisymmetric results. $\Delta t = 100$ s, $s = 0.84$.

The hysteresis loss in the coil is further investigated. A possible explanation for the peculiar shape of the hysteresis loss curve is the fact that unlike in the axisymmetric geometry, the flux density and the corresponding local hysteresis loss also depend on the angular position in the coil. As mentioned in Section 6.2.2, most losses occur in the upper central part of the coil. Fig. 6.15 compares the local hysteresis loss in different angular positions θ. Please refer to Fig. 4.17(b) for the definition of the angular position with respect to the spiralized poles. As may be observed, the hysteresis loss peak does not occur at the same instant depending on the angular position. In particular, the peak is reached sooner for the parts of the coil which are close to the poles ($\theta = \{-25, -10, -85\}$ °) and the corresponding hysteresis loss is larger. It may be explained by the proximity of the ferromagnetic poles, increasing the flux density (and its variation) in some parts of the coil. On the other hand, the region of the coil which is closer to a cavity ($\theta = \{-70, -55, -40\}$ °) experiences a smaller flux variation and the loss peak is reached later. Consequently, the hysteresis loss integrated over the volume of the coil may be smoothed out by the angular variation of the local losses. Please note

that this is *one* possible explanation for the observed behaviour of the integrated loss curve. As the geometry is complex and the magnetic response of the system is nonlinear, many different physical phenomena are involved and the previous discussion covers only a small part of these phenomena.

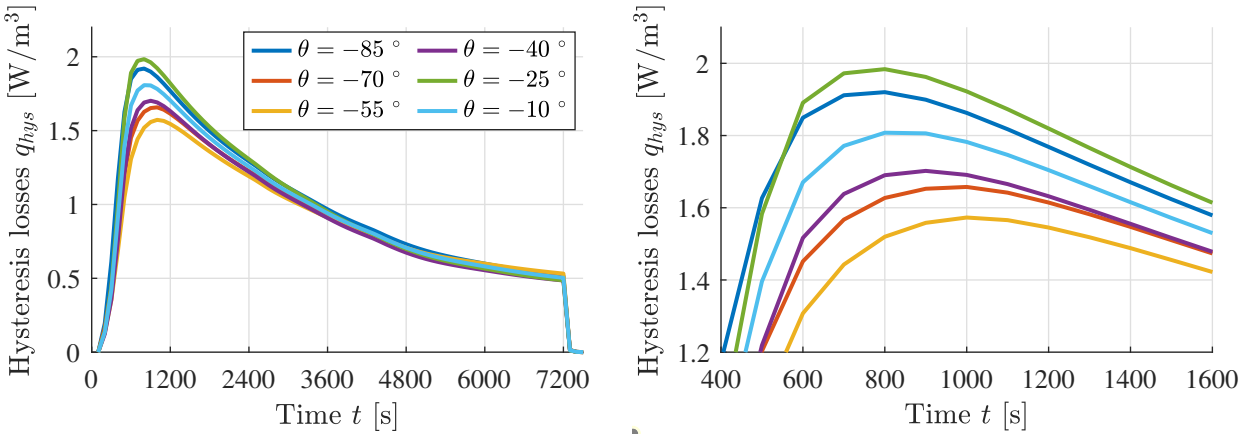

Figure 6.15: Evolution of the local hysteresis loss q_{hys} at the point p1 displayed in Fig 6.4(b) for different angular positions θ. $\Delta t = 100$ s, $s = 0.84$.

6.4 Parametric studies

In this section, multiple physical parameters are varied and their impact on the maximal temperature within the coil is assessed. The default configuration of the cyclotron is recalled: $h = 100$ W/m^{2}K, $T_{\text{up}} = 7200$ s and $f_f = 51$ µm. The studies are mostly performed in the three-dimensional geometry, for which the numerical parameters are $s = 0.84$ and $\Delta t = 100$ s. In some cases, the results are also discussed in the axisymmetric geometry, which allows for a simpler interpretation while providing a conservative approach to the problem as discussed previously. The axisymmetric simulations are performed with $s = 0.12$ and $\Delta t = 20$ s.

6.4.1 Impact of the convective heat transfer coefficient

As mentioned in Chapter 5, the value of the convective heat transfer coefficient $h = 100$ W/m^{2}K used in the previous sections is considered conservative as larger coefficients have been reported for liquid helium. Nevertheless, its impact on the maximal temperature within the coil is shown in Fig. 6.16. As may be observed, even for an excessively small value of $h = 0.1$ W/m^{2}K, the maximal temperature increase is $\Delta T_{\text{max}} = 0.389$ K. In that case, considering the worst case of the maximal flux density $b_{\text{c,max}} = 3.58$ T, the critical current density of Nb-Ti is $j_{\text{c}} = 3525$ A/mm^2 corresponding to a conductor critical current of $I_{\text{c}} = 3197$ A which is still much larger than the maximal conductor current of 1002 A. As may be observed in Fig. 6.16(a), decreasing the convective coefficient introduces some delay in the system. Once again it can be explained using dimensional analysis. For $h < 1$ W/m^{2}K, the Biot number is small: $Bi < 0.1$, from Eq. (5.14). In that case, the temperature gradients in the coil can be neglected [40] and the thermal time constant is given by:

$$\tau_{\text{th}} = \frac{\rho_{\text{eff}} c_{p,\text{eff}} L_c}{h} \sim \frac{100}{h}, \tag{6.4}$$

which is retrieved numerically when looking at the cooling down after the ramp-up is completed, i.e. $t > 7200$ s. On the other hand, further increasing the convective coefficient above $h = 100$ W/m^{2}K does not affect the thermal behaviour of the coil. Such a behaviour is expected because the thermal

time constant does not depend on h for a large Biot number, as discussed in Chapter 5. Furthermore, the maximal temperature rise in the coil is independent of h in the theoretical limit of $h \to \infty$ as highlighted in Eq. (6.1). It is therefore of no practical interest to further increase the cooling efficiency of the coil cryostat, as this would mean increasing the velocity of the liquid helium and hence the power consumption of the cryogenic equipment.

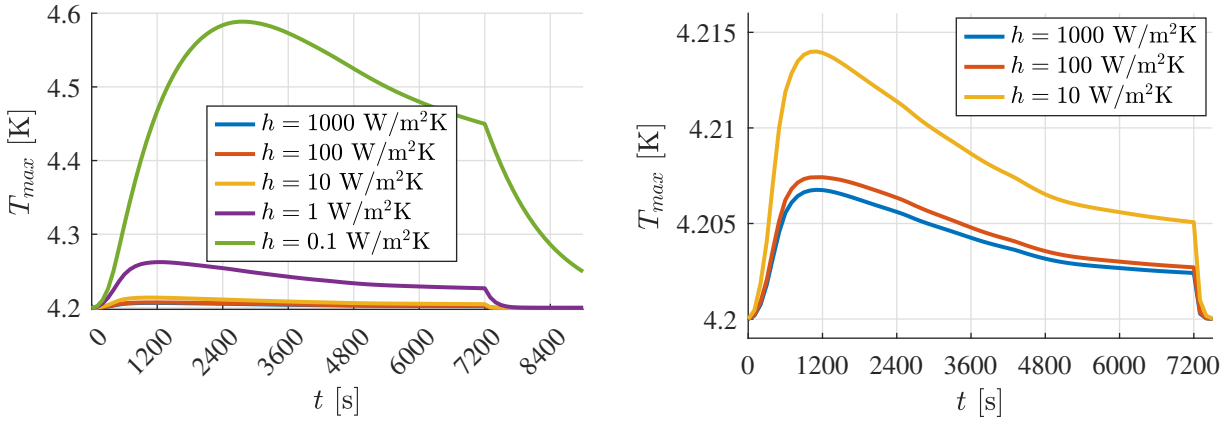

Figure 6.16: Evolution of the maximal temperature T_{max} in the coil for various convective heat transfer coefficients h. 3D results.

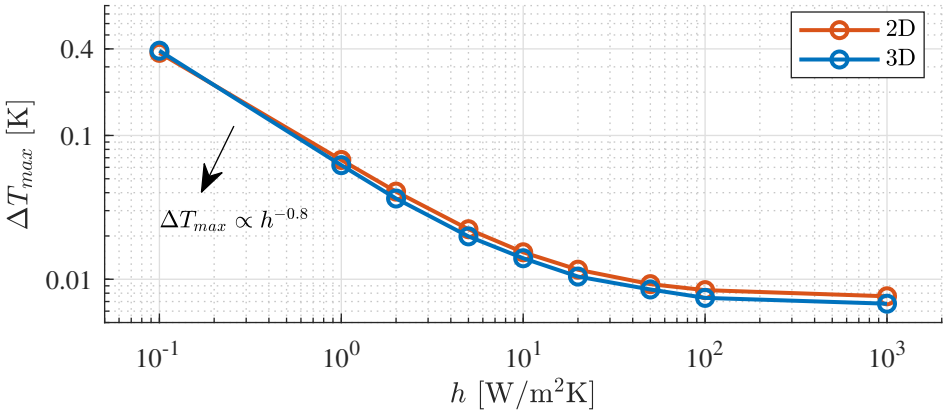

Figure 6.17: Maximal temperature increase ΔT_{max} during ramp-up against liquid helium convective heat transfer coefficient h. Comparison between results in 3D and in 2D axisymmetric geometry.

The maximal temperature increase during ramp-up is shown in Fig. 6.17 for different convective coefficients. As discussed earlier, the 2D axisymmetric model slightly overestimates the temperature rise. Notably, two asymptotic regimes can be distinguished. In the large Biot number regime, the temperature increase is independent of the convective coefficient. On the other hand, in the small Biot number regime, temperature gradients in the solid can be neglected and there is a balance between heat generation and convective cooling. Assuming a thermal time constant smaller than the ramp-up characteristic time (which is less and less true as h decreases), it comes from dimensional analysis:

$$q_{\text{hys}} L_c \sim h \Delta T \Rightarrow \Delta T \sim \frac{q_{\text{hys}} L_c}{h}, \tag{6.5}$$

which explains the shape of the curve in Fig. 6.17. The fact that the numerical maximal temperature rise scales as $\Delta T_{\text{max}} \propto h^{-0.8}$ can among other reasons be explained by the nonlinearity of the problem. Since the critical current density decreases as temperature is increased, so does the local hysteresis loss (assuming mostly fully penetrated filaments). In the intermediate regime, all the different phenomena must be considered and it is more complex to perform dimensional analysis.

6.4.2 Impact of the total ramp time

The total ramp time of the C400 is $T_{\text{up}} = 7200$ s. As previously observed, the temperature rise in the coil is not significant. In this section, the duration of the current ramp is reduced. For now, a linear current profile as described by Eq. (4.1) is still considered. For all the simulations performed, the time step has been adjusted to keep the ratio $T_{\text{up}}/\Delta t$ fixed throughout the study. It is $T_{\text{up}}/\Delta t = 72$ in 3D and $T_{\text{up}}/\Delta t = 360$ in 2D. The maximal temperature rise in the coil is shown in Fig. 6.18. As expected, the temperature rise increases with the ramp rate. Remarkably, even for a ramp time of 360 s, the maximal temperature rise is $\Delta T_{\text{max}} = 0.15$ K and the coil still remains in the superconducting state. Nevertheless, such a fast ramp-up is not feasible in practice: this issue is addressed below. Before that, a closer look at Fig. 6.18 allows us to observe a $\Delta T_{\text{max}} \sim 1/T_{\text{up}}$ dependence of the temperature peak. This can be explained by the results shown in Fig. 6.19, representing the mean loss averaged over the duration of the ramp-up. Note the agreement between the 3D and the 2D axisymmetric results.

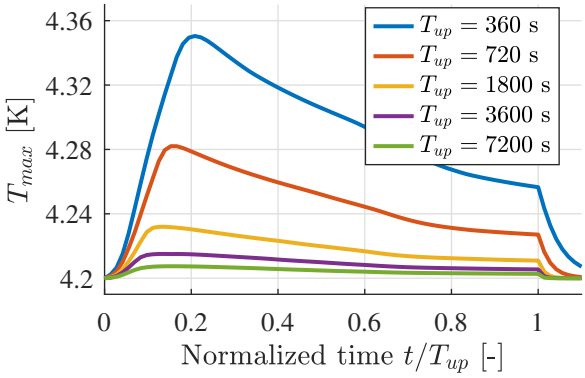

Figure 6.18: Evolution of the maximal temperature T_{max} in the coil for various ramp times T_{up}. For proper comparison, the time is normalized by T_{up}. 3D results.

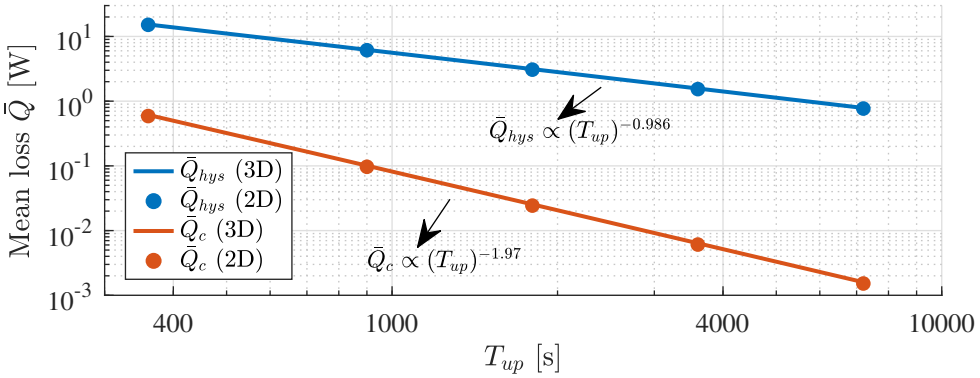

Figure 6.19: Mean hysteresis loss $\bar{Q}_{\text{hys}}$ and mean coupling loss $\bar{Q}_{\text{c}}$ during ramp-up against total ramp-up time T_{up}. Comparison between results in 3D and in 2D axisymmetric geometry.

As previously discussed, the hysteresis loss is much larger than the coupling loss. However, the ratio between the two loss sources decreases as the ramp time is reduced. It is expected from dimensional analysis as the hysteresis loss scales as $q_{\text{hys}} \propto \dot{b} \propto 1/T_{\text{up}}$, while the coupling loss scales as $q_{\text{c}} \propto \dot{b}^2 \propto 1/T_{\text{up}}^2$. Such results are obtained numerically. In 3D: $\bar{Q}_{\text{hys}} = 15.31$ W for $T_{\text{up}} = 360$ s compared to $\bar{Q}_{\text{hys}} = 1.568$ W for $T_{\text{up}} = 3600$ s. Reducing the ramp time further increases the maximal temperature in the coil, which tends to slightly reduce the hysteresis loss due to $\partial j_{\text{c}}/\partial T < 0$, highlighting the nonlinearity of the problem. In the large Biot number regime, the temperature increase is proportional to the loss source, as emphasized by Eq. (6.1). The hysteresis loss scaling law therefore explains the evolution of the maximal coil temperature with ramp time in Fig. 6.19.

In the present case, the limiting factor is not the temperature increase. Due to the consequent energy that needs to be charged in the magnet ($E_m = 34.3$ MJ, from Section 4.8.2), the ramp time is mainly constrained by the voltage available at the power supply terminals: $\Delta v_{\text{lim}} = 20$ V. In practice, the two coils (below and above the median plane of the cyclotron) are arranged in series and the maximal voltage available for the coil studied in this work is $\Delta v'_{\text{lim}} = \Delta v_{\text{lim}}/2 = 10$ V.

The a-formulation presented in Chapter 3 can be adapted to retrieve the potential difference across one stranded conductor turn Δv_1 [V] as a global quantity. The corresponding formulation is called the a-v-formulation. Please refer to [6] for a theoretical description of the formulation and the coupling to circuit relations.

The total voltage across the coil Δv [V] has been computed in the axisymmetric geometry, taking into account the number of turns of the two sub-coils: $\Delta v = 1344 \Delta v_1$.

Physically, the induced voltage drop across the conductor is a direct consequence of Lenz's law: $\Delta v_1 = -d\phi_b/dt$. Neglecting the electrical resistance of the superconducting coil, the induced voltage is equal to the time variation of the magnetic flux ϕ_b [Wb] embraced by the coil. It depends strongly on the magnetic response of the ferromagnetic yoke and on the induced eddy currents in the yoke, which oppose the flux variation. The maximal voltage drop across the coil is shown in Fig. 6.20 for different ramp times. The voltage drop increases as the ramp time decreases, which is expected since the magnetic flux grows more rapidly. Remarkably, the maximal voltage drop scales as $\Delta v_{\text{max}} \propto T_{\text{up}}^{-0.65}$. The particular numerical value of the scaling factor is difficult to interpret as the magnetic problem is nonlinear. Nevertheless, Fig. 6.20 highlights the need to choose a ramp time greater than $T_{\text{up}} = 1200$ s (20 minutes) to avoid overloading the power source when working with a linear current profile.

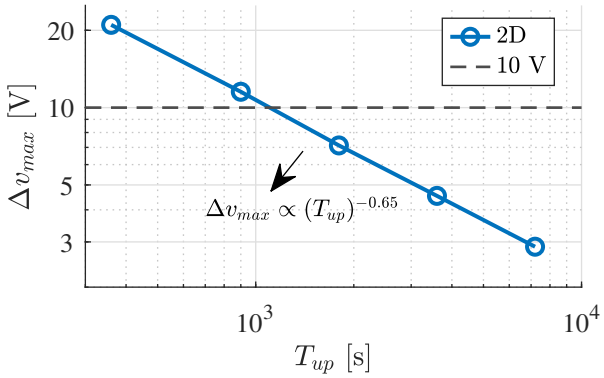

Figure 6.20: Maximal voltage drop Δv_{max} across the coil for various ramp-up times T_{up}. Axisymmetric results.

6.4.3 Impact of the filament diameter

As mentioned in Section 3.5, working with finer filaments is expected to reduce the Nb-Ti hysteresis losses. One simulation has been performed with filaments of diameter $d_f = 30$ µm and the corresponding maximal temperature evolution is shown in Fig. 6.21. It is compared to the results discussed previously. The number of filaments per conductor has been increased to keep a constant Nb-Ti filling ratio with respect to the default configuration.

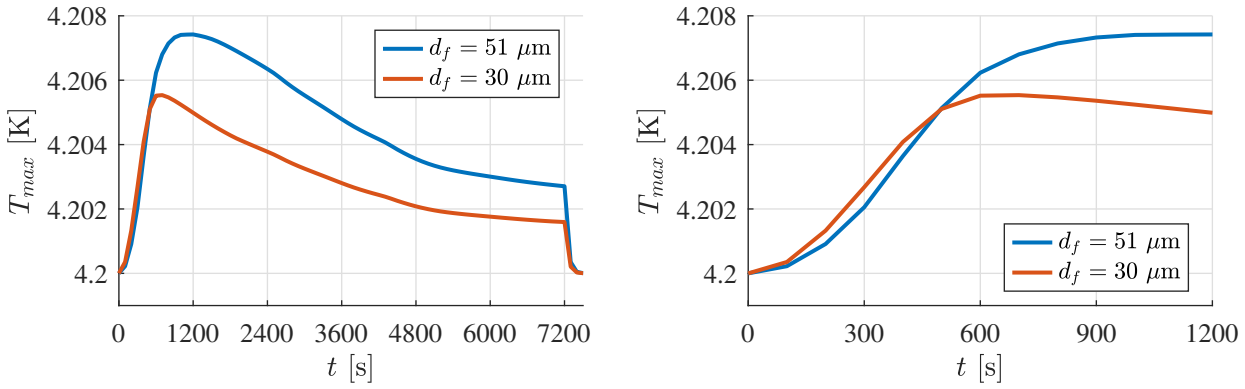

Figure 6.21: Evolution of the maximal temperature T_{max} in the coil for two different Nb-Ti filament diameters d_f. 3D results.

As a direct consequence of the smaller hysteresis loss, the maximal temperature increase in the coil is reduced to $\Delta T_{\text{max}} = 0.0055$ K. Initially, the temperature is higher when using finer filaments.

Additionally, the maximal temperature is reached earlier during ramp-up. These results can again be explained by the analytical approximation (Eq. (3.61)) used to compute the hysteresis loss, which is represented in Fig. 6.22 for the considered diameters. With all other parameters held constant, the loss is decreased in the fully penetrated regime, as expected from Eq. (3.59). Conversely, the loss is increased in the weakly penetrated regime, as also anticipated from Eq. (3.60). Furthermore, the fully penetrated regime is achieved earlier for finer filaments. Globally, the hysteresis loss in the C400 coil is indeed reduced when working with finer filaments. Reducing the filament diameter therefore constitutes a solution for decreasing the temperature increase during ramp-up. Note that a filament diameter of 30 µm seems reasonable as 6 µm filaments were used in superconducting cables for the LHC [32].

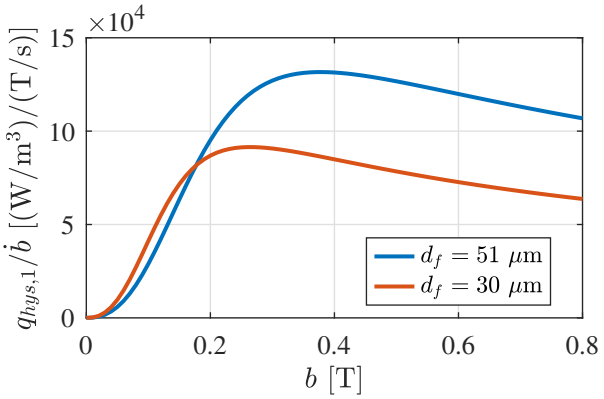

Figure 6.22: Theoretical (Eq. (3.61)) single filament hysteresis loss $q_{\text{hys,1}}$ normalized by the flux density variation $\dot{b}$ at $T_{\text{He}} = 4.2$ K for two filament diameters d_f.

6.4.4 Impact of the current profile

The diameter of Nb-Ti filaments cannot be modified once the coil is built. A more convenient solution to reduce the temperature rise in the coil is to modify the default linear current ramp used in the previous sections. In fact, the ramp-up procedure can be adjusted based on the physical interpretation provided in Section 6.2.2. Since the hysteresis loss is proportional to the flux density variation, the main idea is to reduce the ramp rate in the period corresponding to the maximal loss in the default configuration. From the results shown in Fig. 6.14(b), the hysteresis loss is maximal in the time range $t \sim 600 - 2500$ s. However, reducing the ramp rate in one range requires increasing the ramp rate in another range to keep the total ramp time at $T_{\text{up}} = 7200$ s. The ramp rate is thus increased in the final part of the ramp-up procedure where the losses are relatively small.
Different piecewise linear functions were tested and the optimized ramp shown in Fig. 6.23(a) has been fine-tuned by trial and error. The final current ramp rate reads

$$\frac{dI(t)/I_{\text{max}}}{dt/T_{\text{up}}} = \begin{cases} 1, & \text{for } t \in [0; 600[\text{ s}, \\ 0.75, & \text{for } t \in [600; 2800[\text{ s}, \\ 0.9, & \text{for } t \in [2800; 5000[\text{ s}, \\ 1.35, & \text{for } t \in [5000; 7200[\text{ s}. \end{cases} \tag{6.6}$$

As can be observed in Fig. 6.23(b), the integrated hysteresis loss has indeed been reduced in the period that previously corresponded to the maximal loss. On the other hand, the loss in the last part of the ramp has been significantly increased. The optimal choice thus results from a trade-off. Accordingly, the maximal temperature rise in the coil has been reduced from $\Delta T_{\text{max}} = 0.0074$ K to $\Delta T_{\text{max}} = 0.0064$ K. The maximal temperature rise has thus been decreased by 14 % compared to the default current ramp, highlighting the effectiveness of the optimized ramp-up procedure proposed in this section.

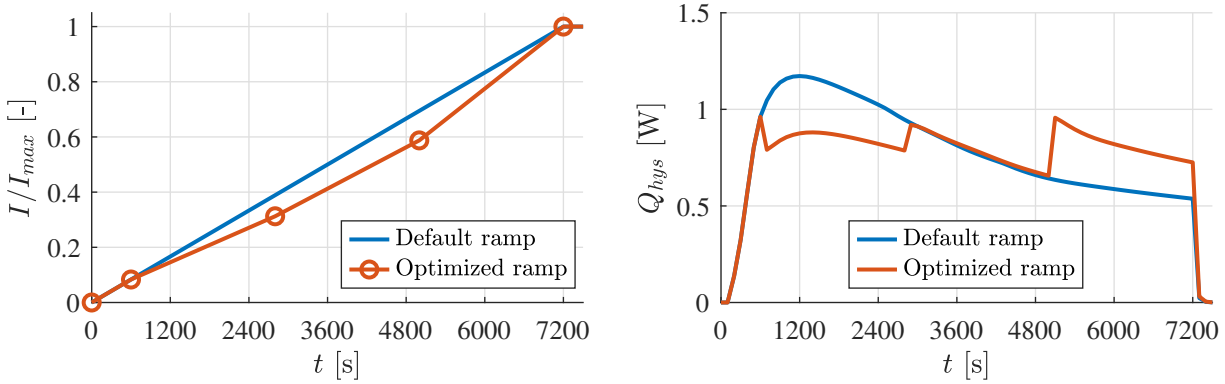

(a) (b)

Figure 6.23: (a) Optimized current profile normalized by the nominal current I/I_{max} and (b) evolution of the corresponding integrated hysteresis loss Q_{hys} in the coil, compared to the default current profile. 3D results.

6.4.5 Impact of the current configuration

Let us discuss the different nominal current configurations summarized in Tab. 2.1. As mentioned in Section 4.8.2, the two proton configurations give similar steady state results. As shown in Fig. 6.24, working in the p1 configuration induces a slightly larger temperature increase during ramp-up. Such a result is quite complex to interpret as the problem is highly nonlinear. In addition, the two carbon configurations lead to a smaller temperature rise in the coil as they involve lower nominal currents compared to the proton configuration. The peak temperature is also reached slightly later in the carbon configurations. Nevertheless, all configurations give very similar results as the maximal temperature rise during ramp-up remains in the range $\Delta T_{\text{max}} = 0.0074 - 0.0080$ K. The default configuration (Config. 0) induces the smallest temperature rise.

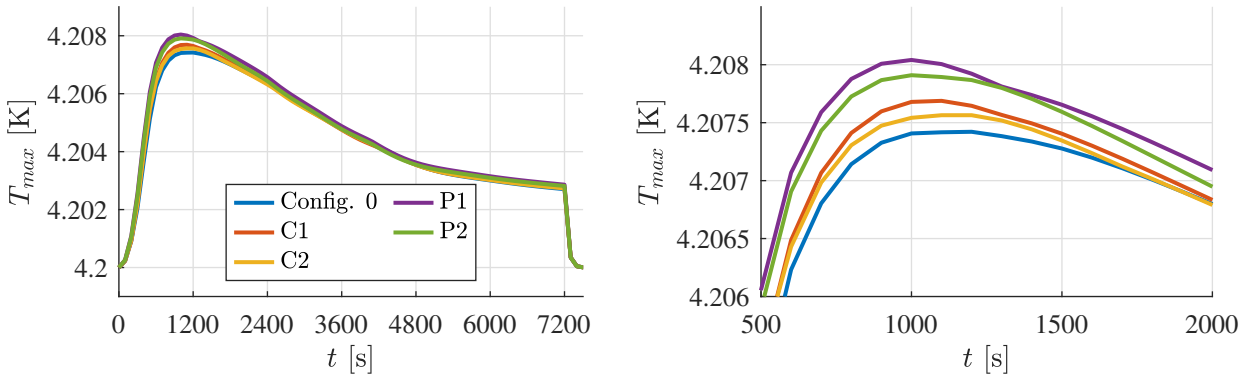

Figure 6.24: Evolution of the maximal temperature T_{max} in the coil for the different nominal current configurations listed in Tab. 2.1. 3D results.

Conclusion of the chapter

After discussing the coupling scheme between the magnetodynamic and thermal solvers, the numerical simulation parameters were varied until the convergence of the results was found to be satisfactory. During a normal ramp-up procedure, the temperature increase in the coil is extremely small. The maximal temperature rise is $\Delta T_{\text{max}} = 0.0084$ K in the 2D axisymmetric geometry. As discussed, this result was expected from dimensional analysis. In addition, the inter-filament coupling loss was shown to be negligible compared to the hysteresis loss in Nb-Ti filaments, which was also expected from dimensional analysis. A deeper physical interpretation has highlighted the significant role of the hysteresis loss in the maximal temperature increase in the coil. The large Biot number regime leads to a temperature rise that is directly proportional to the main source of loss, namely the filamentary hysteresis loss. The hysteresis loss has been studied in more detail and the maximal loss occurs around $t \sim 900$ s due to the coil region closer to the cyclotron center reaching the threshold flux density value of $b \sim 0.38$ T, which maximizes the local hysteresis losses. Furthermore, since the thermal time constant of the coil is small compared to the ramp time, the temperature evolution is remarkably consistent with the hysteresis loss evolution.
The hysteresis loss curve is smoothed out in the three-dimensional geometry of the cyclotron and the maximal temperature rise in the coil is $\Delta T_{\text{max}} = 0.0074$ K, which is lower than that obtained in 2D. Among other reasons, this can be explained by the angular variation of the flux density in the coil due to the spiralized poles. As a result, the maximal loss in the coil occurs at different times depending on the angular position. Nevertheless, the 3D results are very similar to the 2D axisymmetric results, which slightly overestimate the maximal temperature rise and therefore provide a conservative approach to the problem.
In the last part of this chapter, the convective heat transfer coefficient was varied and it was shown that even with an excessively small convective coefficient, the temperature increase is not significant and the Nb-Ti filaments still remain in the superconducting state. It was also possible to distinguish different asymptotic regimes depending on the Biot number.
The ramp time was reduced and the maximal temperature rise did not exceed $\Delta T_{\text{max}} = 0.16$ K even for a 6 minute ramp-up. However, due to the limited voltage difference available at the power source terminals, it was found that the ramp-up procedure could not be performed in less than 20 minutes. This result is valid for a linear current ramp.
Since the temperature rise is mainly determined by the hysteresis loss in the coil, a solution to reduce the temperature rise during ramp-up is to reduce the diameter of the Nb-Ti filaments. The effectiveness of this solution has been demonstrated in this chapter. Furthermore, an optimized current ramp has been proposed to reduce the hysteresis loss during ramp-up, which constitutes a more practical solution as it can be implemented and adapted on an existing machine. It has reduced the maximal temperature rise by 14%.

The main conclusion of the chapter is the fundamental role played by hysteresis losses in the magnetothermal behaviour of the coil. The analytical approximation used to compute these losses relies on many assumptions as discussed in Section 3.5. Consequently, the accuracy of the hysteresis loss prediction is evaluated in the next chapter based on a numerical model at the filament scale, which will be the main building block of the multi-scale resolution presented in the final chapter of this thesis.

CHAPTER 7
LOSSES AT THE FILAMENT SCALE

As highlighted in Chapter 6, hysteresis loss in Nb-Ti filaments plays a central role in the thermal behaviour of the coil. The aim of this chapter is to assess the accuracy of the analytical approximation (Eq. (3.61)) used thus far for computing hysteresis losses at the macroscopic scale. For that purpose, a single Nb-Ti filament is modelled, and its magnetic response to a transverse applied magnetic field is computed numerically. The impact of the transport current on hysteresis loss, which has been neglected thus far, is also explored. The superconducting constitutive equation implemented numerically is the power-law, an extension of the CSM as introduced in Chapter 3. It is important to note that the analytical approximation used in the previous chapter is based on the CSM. Therefore, using the power-law will affect the hysteresis loss in the filament, and this impact will be quantified in this chapter. Finally, the filament model allows the limitations of analytical approximations to be highlighted. Consequently, a multi-scale approach for computing hysteresis losses is proposed and implemented in Chapter 8.

7.1 Numerical model

A representation of the filament model and the corresponding boundary conditions is shown in Fig. 7.2. The radius of curvature of the filament is neglected and only its cross-section is modelled. The model developed by Geuzaine, Kamani and Stenvall [52] as a GetDP benchmark for superconductors has been adapted to meet the requirements of the present study. A transverse uniform flux density $\bar{\boldsymbol{b}}_a(t)$ [T] is applied to the outer boundary of the domain. It can be interpreted as the local flux density in the composite conductor of the C400 coil. As the applied flux density varies with time, induced currents are generated in the superconducting filament. The outer domain must be chosen large enough to avoid impacting the magnetic response of the filament. In the present context, an outer diameter of $d_{\text{out}} = 10 d_f = 510$ µm was found to be appropriate. The mesh used for discretizing the domain is shown in Fig. 7.1. It has been carefully refined and the convergence of results has been checked.

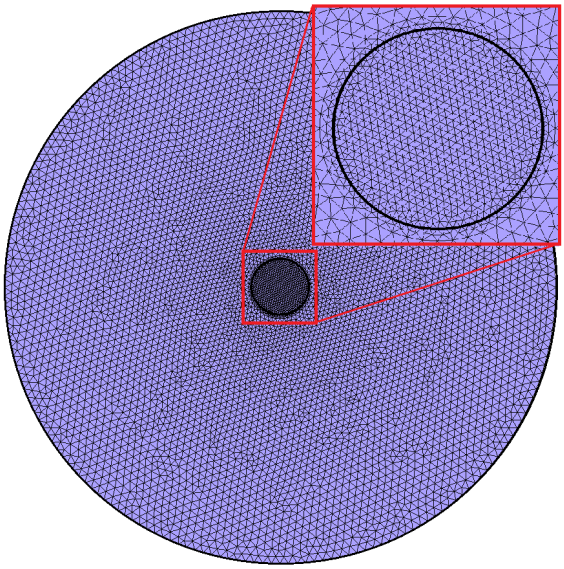

Figure 7.1: Mesh discretization of the filament.

Moreover, a net transport current $\bar{I}_{\mathrm{t}}(t)$ [A] is imposed along the $\hat{\boldsymbol{z}}$-axis of the filament, which corresponds to the local transport current contribution to the total current in the composite conductor. The j-e constitutive law of the superconducting filament is modelled using the power-law introduced in Section 3.3.4. The h-ϕ formulation is chosen as the weak formulation and it is described in Section 3.1. The conducting domain Ω_{c} is only composed of the filament. The outer domain is chosen to be non-conductive for focusing on the hysteresis loss inside the Nb-Ti filament. As such, the inter-filament coupling losses are disregarded. No essential boundary condition is considered, $\Gamma_h = \emptyset$ and $\Gamma_e = \Gamma$. However, the formulation as stated in Eq. (3.27) must be adapted for allowing a uniform external flux density to be imposed.

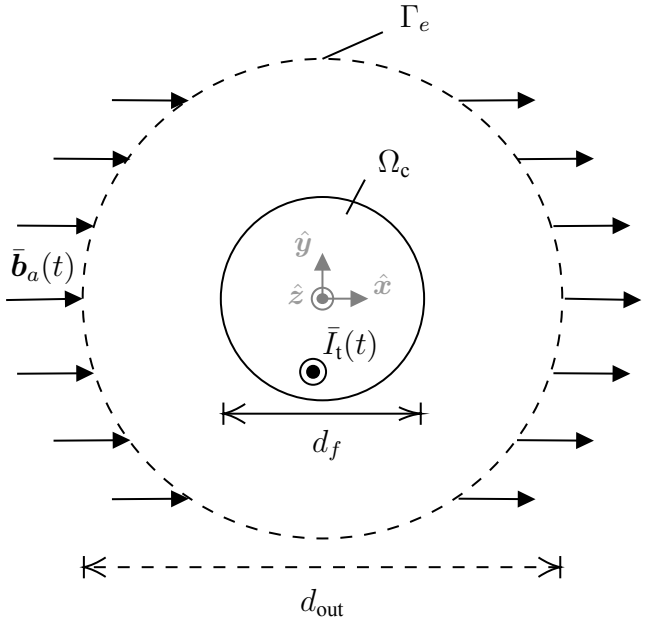

Figure 7.2: Numerical model of one Nb-Ti filament, denoted by Ω_{c}. The outer domain is composed of a non-conducting medium and a uniform external field $\bar{\boldsymbol{b}}_a$ [T] is applied to the outer boundary Γ_e of the domain. A net transport current $\bar{I}_{\mathrm{t}}$ [A] is imposed along the $\hat{\boldsymbol{z}}$-axis of the filament. The diameter of the filament is $d_f = 51$ µm and the outer domain diameter is $d_{\mathrm{out}} = 510$ µm.

The surface term in the h-ϕ-formulation can be modified by taking into account the fact that the boundary Γ_e is around the non-conducting domain of study in which the curl-free property of $\boldsymbol{h}$ is satisfied.
Hence, by setting the test function to $\boldsymbol{h}' = \nabla\phi'$ (the missing negative sign with respect to Eq. (3.28) does not matter as test functions are arbitrary), it comes successively

$$\langle \bar{\boldsymbol{e}} \times \boldsymbol{n}, \boldsymbol{h}' \rangle_{\Gamma_e} = \langle \bar{\boldsymbol{e}} \times \boldsymbol{n}, \nabla\phi' \rangle_{\Gamma_e} \tag{7.1}$$

$$= \int_{\Gamma_e} \nabla \cdot \Big(\phi' (\bar{\boldsymbol{e}} \times \boldsymbol{n}) \Big) \, d\Gamma_e - \langle \nabla \cdot (\bar{\boldsymbol{e}} \times \boldsymbol{n}), \phi' \rangle_{\Gamma_e} \tag{7.2}$$

$$= \int_{\Gamma_e} \nabla \cdot \Big(\phi' (\bar{\boldsymbol{e}} \times \boldsymbol{n}) \Big) \, d\Gamma_e + \langle \bar{\boldsymbol{e}} \cdot (\nabla \times \boldsymbol{n}), \phi' \rangle_{\Gamma_e} - \langle \boldsymbol{n} \cdot (\nabla \times \bar{\boldsymbol{e}}), \phi' \rangle_{\Gamma_e} \tag{7.3}$$

$$= -\langle \boldsymbol{n} \cdot (\nabla \times \bar{\boldsymbol{e}}), \phi' \rangle_{\Gamma_e} = \langle \boldsymbol{n} \cdot \partial_t \bar{\boldsymbol{b}}, \phi' \rangle_{\Gamma_e}. \tag{7.4}$$

The first term in Eq. (7.3) is equal to zero because the boundary Γ_e is closed, while the second term is equal to zero because the boundary is smooth. Hence, through Faraday's law, the natural boundary condition amounts to specify the variation of the flux density $\boldsymbol{n} \cdot \partial_t \bar{\boldsymbol{b}} = \boldsymbol{n} \cdot \partial_t \bar{\boldsymbol{b}}_a$ normal to the boundary Γ_e. As the applied flux density is considered zero in $t = 0$, a boundary condition on $\boldsymbol{n} \cdot \partial_t \bar{\boldsymbol{b}}_a$ is equivalent to a boundary condition on $\boldsymbol{n} \cdot \bar{\boldsymbol{b}}_a = \int_0^{t^*} \boldsymbol{n} \cdot \partial_t \bar{\boldsymbol{b}}_a \, dt$.
Note that such a boundary condition does not interfere with the magnetic field generated by a net transport current in the superconducting filament. The self-field $\boldsymbol{b}_{\mathrm{self}}$ is mostly azimuthal far from the filament, implying that $\boldsymbol{n} \cdot \boldsymbol{b}_{\mathrm{self}} = 0$ on Γ_e.

Due to the strongly nonlinear behaviour of the power-law, the convergence of the Newton-Raphson algorithm depends on various parameters, such as the rate of applied flux density variation or the rate of transport current increase in the filament. To ensure robustness, the model involves an adaptive time step. If the iterative algorithm fails to converge within 12 iterations, the time step is reduced by a factor of 3. Conversely, if the convergence is achieved in less than 6 iterations, the time step is increased by a factor of 1.5.

7.2 Constant critical current density

First, let us consider a constant critical current density $j_c = 5 \times 10^9$ [A/m^2] in the filament. It is consistent with the constant j_c assumption made for the derivation of the analytical approximation introduced in Section 3.5. The corresponding penetration flux density (Eq. (3.58)) is $b_p = 0.102$ T. The transport current is neglected for now, $\bar{I}_t = 0$, and a uniform flux density is applied along the $\hat{\boldsymbol{y}}$-axis. For now, a linear monotonically increasing field ramp is considered from 0 T to $b_{\text{max}} = 2$ T at a constant rate denoted by $\dot{b}_a$ [T/s]:

$$\bar{\boldsymbol{b}}_a(t) = \dot{b}_a \, t \, \hat{\boldsymbol{y}}, \qquad \text{for } t \in [0; b_{\text{max}}/\dot{b}_a]. \tag{7.5}$$

7.2.1 Flux penetration in the filament

The flux penetration mechanism has been discussed in Section 3.5. Here, numerical results obtained with $n = 50$ and $\dot{b}_a = 1$ T/s are briefly presented to validate the previous theoretical description. Note that the rate $\dot{b}_a = 1$ T/s applied in this section is several orders of magnitude larger than what is observed in the C400 coil ($\dot{b} \sim 3 \times 10^{-4}$ T/s). The results are shown in Fig. 7.3. Initially, persistent currents are established on a thin elliptical layer on the surface of the filament, resulting in a zero flux density within the center of the filament. The current density is determined by the power-law model, allowing the electric field to vary smoothly while the current density magnitude is either very small or close to j_c. In the center of the filament, the current density magnitude is lower than 100 A/m^2, and the variations in Fig. 7.3(a-b) are due to numerical perturbations around zero. Then, the flux density gradually penetrates the filament until currents are established throughout the entire filament. At $t = 0.11$ s, $b_a = 0.11$ T, and the fully penetrated regime is reached, which is consistent with the $b_p = 0.102$ T prediction from the CSM. In the fully penetrated regime, the persistent currents and the filament magnetization are, to a first approximation, independent of time (as predicted by the CSM), resulting in an electric field of $e_z \sim \dot{b}_a x$ according to Faraday's law. Note the similarity between Fig. 7.3(a,d) and the theoretical expectation from the CSM in Fig. 3.10.

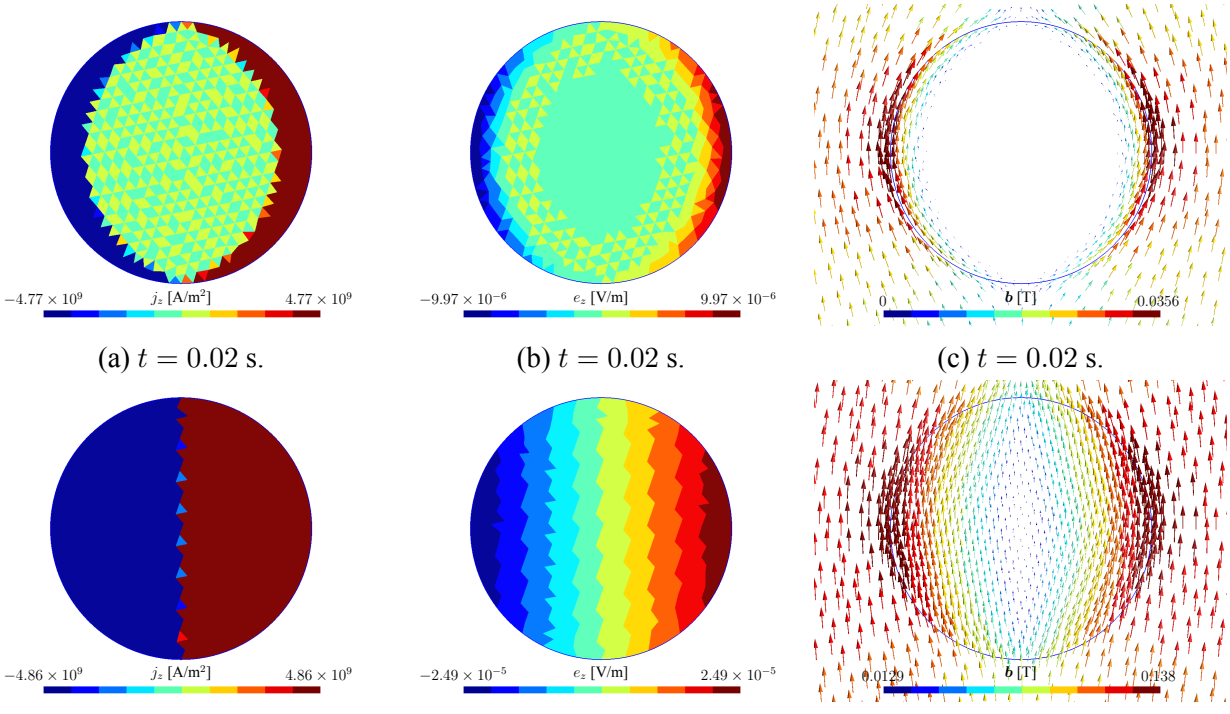

(a) $t = 0.02$ s. (b) $t = 0.02$ s. (c) $t = 0.02$ s.

(d) $t = 0.11$ s. (e) $t = 0.11$ s. (f) $t = 0.11$ s.

Figure 7.3: From left to right: current density j_z, electric field e_z and flux density $\boldsymbol{b}$ in the filament at $t = 0.02$ s (weak penetration) and $t = 0.11$ s (full penetration).

In fact, the electric field in full penetration is very similar to $e_z = \dot{b}_a x$ as highlighted in Fig. 7.4(a). The current density distribution can be deduced from the power-law constitutive equation as

$$j_z(x) = \text{sign}(x) j_c \left(\frac{|\dot{b}_a x|}{e_c} \right)^{1/n}, \tag{7.6}$$

which is retrieved numerically as shown in Fig. 7.4(b). As $|\dot{b}_a x| < e_c = 10^{-4}$ V/m in the present configuration, the current density is slightly lower than the critical current density.

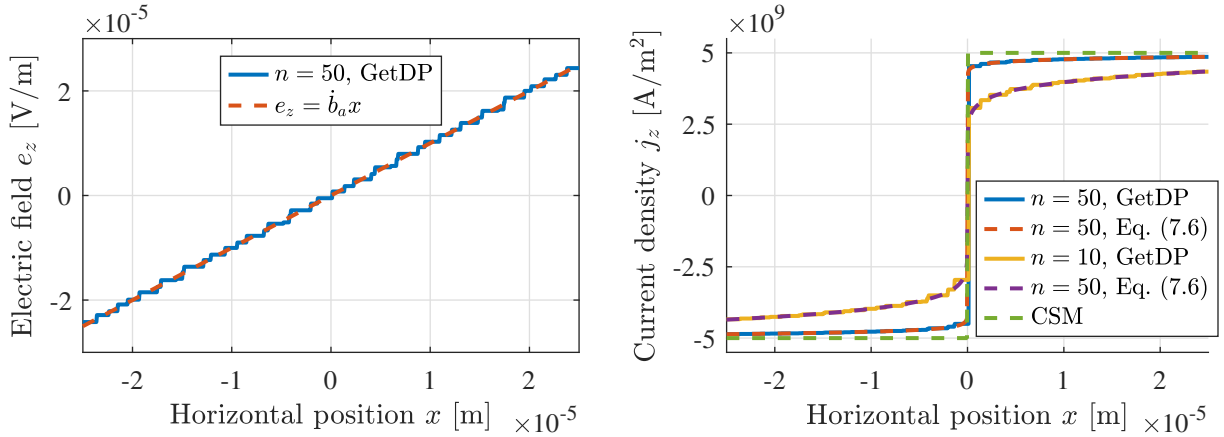

(a) (b)

Figure 7.4: (a) Electric field e_z and (b) current density j_z along the $\hat{\boldsymbol{x}}$-axis of the filament, in $y = 0$ and $t = 2$ s for $\dot{b}_a = 1$ T/s. Numerical results for $n = 50$ and $n = 10$ (GetDP) are compared to the distribution (Eq. (7.6)) deduced from $e_z = \dot{b}_a x$ and to the CSM.

7.2.2 Impact of the power-law exponent

The quantity of interest is the filament hysteresis loss averaged over the volume of the filament, $q_{\text{hys},1}$ as defined by Eq. (3.57). It has been computed numerically during the linear field ramp-up and the results are shown in Fig. 7.5 for multiple power-law exponent n values.
Several conclusions can be drawn from the analysis of Fig. 7.5. First, the hysteresis loss reaches a constant value once the applied flux density reaches $b_p = 0.102$ T. Consequently, the interpolated analytical approximation (Eq. (3.61)) used thus far underestimates the loss in the intermediate regime, in which the loss evolution is complex to quantify. Furthermore, the constant loss value in the fully penetrated regime differs from the prediction of the CSM (Eq. (3.59)). The difference in loss between the CSM and the power-law model is quantified in the next section. As anticipated, the numerical full penetration loss tends towards the CSM prediction as n tends towards infinity. Also, the numerical model allows for the validation of the analytical approximation in the weak penetration regime (Eq. (3.60)) derived in this study. The numerical oscillations observed in Fig. 7.5(b) can be attributed to the finite spatial discretization of the filament, with the persisting eddy currents entering the filament element by element as shown in Fig. 7.3(a). Finally, as the exponent of the power-law increases, its nonlinearity becomes stronger, making numerical convergence more challenging. In fact, the total number of iterations for performing the whole resolution from $t = 0$ to $t = 2$ s evolves from 319 with $n = 10$ to 3398 with $n = 120$.

As already discussed, the literature [36, 39] suggests an exponent dependence on flux density and temperature. Nevertheless, the n value for Nb-Ti filaments seems relatively stable in the considered $b \sim 0 - 4$ T range [36, 39] of the C400 conductor and a reasonable value of $n = 50$ is chosen in the next parts of this study, including Chapter 8.

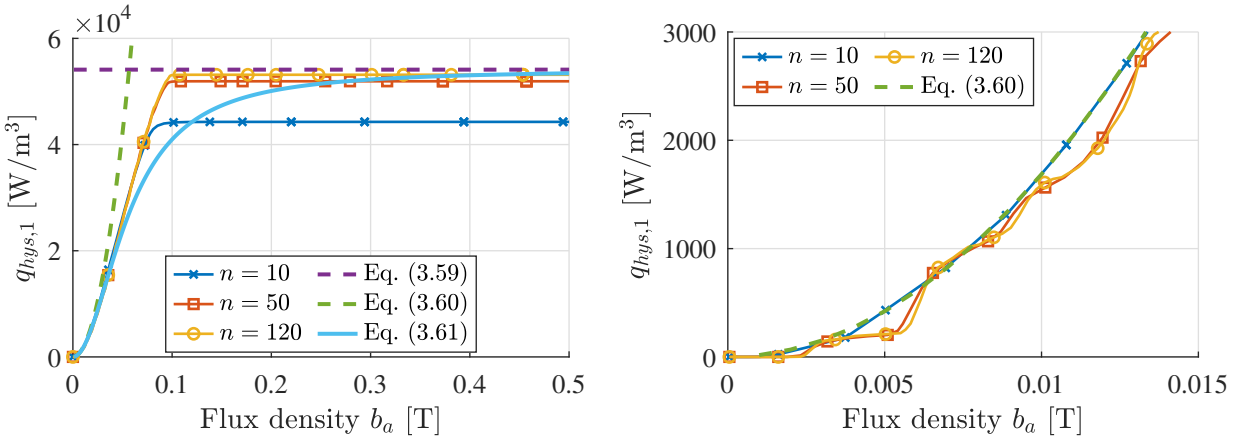

(a) (b)

Figure 7.5: Filament hysteresis loss $q_{\text{hys},1}$ during linear field ramp-up (Eq. (7.5)) with $\dot{b}_a = 1$ T/s for various n exponents, compared to analytical predictions based on the CSM. (a) Global view and (b) focus on the weak penetration regime.

7.2.3 Impact of the ramp rate

In the CSM analytical approximation, the filamentary hysteresis loss is directly proportional to the field ramp rate $\dot{b}_a$. In order to compare the loss curves for different ramp rates $\dot{b}_a$, the hysteresis loss is normalized by the field variation rate in this section. Results are presented in Fig. 7.6. Once again, the analytical approximation seems accurate in the weak penetration regime but results do not correspond in the intermediate regime $b_a \sim 0.05 - 0.02$ T. As highlighted, the normalized loss ratio in full penetration increases with the ramp rate, which is not predicted by the CSM. Such a result is expected as the fully penetrated electric field can be estimated as $e_z = \dot{b}_a x$ as shown previously.

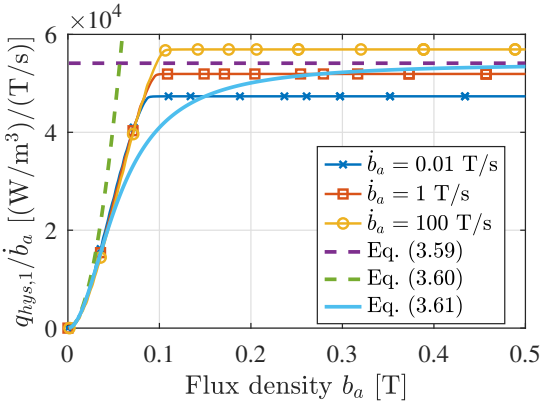

Figure 7.6: Filament hysteresis loss $q_{\text{hys},1}$ during linear field ramp-up (Eq. (7.5)) normalized by the ramp rate $\dot{b}_a$, with $n = 50$ and for various ramp rates, compared to analytical predictions based on the CSM.

The fact that the fully penetrated filamentary hysteresis loss can be estimated analytically assuming $e_z = \dot{b}_a x$ also holds in the power-law model. From the current density distribution in the filament (Eq. (7.6)), the integration of the hysteresis loss in the whole filament yields

$$q_{\text{hys},1} = \frac{\int_{-\pi/2}^{\pi/2} (\cos\theta)^{(n+1)/n} d\theta}{(3+1/n)\pi} j_c d_f \dot{b}_a \left(\frac{d_f \dot{b}_a}{2 e_c} \right)^{1/n}, \tag{7.7}$$

for which the full development is given in Appendix A.8. In the asymptotic regime $n \to \infty$, Eq. (7.7) simplifies to the CSM approximation of Eq. (3.59). The $\int_{-\pi/2}^{\pi/2} (\cos\theta)^{(n+1)/n} d\theta / (3+1/n)$ factor in Eq. (7.7) is very close to $2/3$ for high n values. Its evolution is represented in Fig. 7.7. For $n = 50$, it is equal to 0.6582 which yields a 1.4 % relative difference with respect to the CSM asymptotic regime $(2/3)$.

The fully penetrated hysteresis loss computed numerically is compared to values predicted by both the power-law model and the CSM model and results are gathered in Tab. 7.1. The first conclusion is the validity of the power-law analytical approximation derived in this study. Nevertheless, such a similarity between numerical results and predictions is expected as they both rely on the same power-law model, which is a model and which does not exactly reflect the reality. The nearly constant relative difference of 0.13% is due to the spatial discretization of the filament.

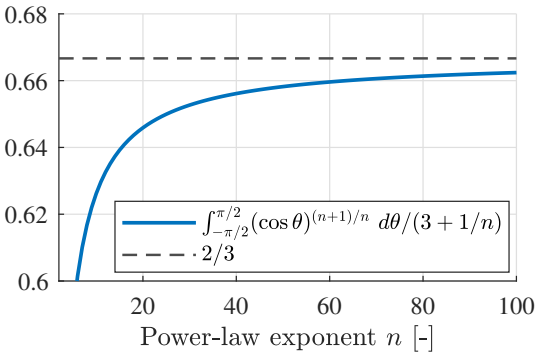

Figure 7.7: Evolution of the $\int_{-\pi/2}^{\pi/2}(\cos\theta)^{(n+1)/n}d\theta/(3+1/n)$ factor in Eq. (7.7) with the power-law n exponent.

In particular, it can be explained by the finite size of elements lying on the $x = 0$-axis for which the current density is significantly lower than j_c as observed in Fig. 7.3(d). Such an interpretation has been validated by reducing the size of the mesh by a factor of two, in which case the relative difference reaches 0.037 %.

As highlighted in Tab. 7.1, the CSM prediction does not yield satisfying results in full penetration as it does not take the impact of the ramp rate into account, among other parameters. In practice, the physics of Nb-Ti filaments is more accurately represented by the power-law model, as the transition to the resistive state is not abrupt but rather smoothed out [36]. As such, the proposed approximation (Eq. (7.7)) is considered more accurate than the CSM prediction used thus far.

n	[-]	10	50	120	50	50
$\dot{b}_a$	[T/s]	1	1	1	0.01	100
GetDP	[W/m^3]	44273	51920	53149	473.52	5692950
Power-law, Eq. (7.7)	[W/m^3]	44336	51990	53216	474.13	5700300
$\delta q_{\text{hys},1}/q_{\text{hys},1}$	[%]	0.14	0.13	0.13	0.13	0.13
CSM, Eq. (3.59)	[W/m^3]	54113	54113	54113	541.13	5411300
$\delta q_{\text{hys},1}/q_{\text{hys},1}$	[%]	22.2	4.22	1.81	14.3	4.95

Table 7.1: Fully penetrated hysteresis loss $q_{\text{hys},1}$ obtained with GetDP for various parameter sets, compared to the power-law approximation (Eq. (7.7)) and the CSM approximation (Eq. (3.59)). The numerical fully penetrated hysteresis loss is computed as an average over $b \in [0.2; 2]$ T. The relative difference compared to numerical results is denoted by $\delta q_{\text{hys},1}/q_{\text{hys},1}$.

Please note that the results obtained in this section rely on three strong assumptions: a constant critical current density, a constant field variation rate, and no transport current. These assumptions will be relaxed in the next sections.

7.3 Critical current dependence on flux density

As discussed in Section 3.3.2, the critical current density of Nb-Ti depends on flux density and temperature. As the temperature variations in the C400 coil are very small, the temperature dependence is neglected in this section and $T = T_{\text{He}} = 4.2$ K is assumed. The $j_c(b)$ relation implemented numerically is the Bottura relationship introduced in Section 3.3.2. The same linear field ramp is considered as in the previous section (Eq. (7.5)) and no transport current is applied to the filament. The normalized hysteresis loss for various ramp rates is shown in Fig. 7.8. It is compared to the CSM analytical approximations already introduced in Fig. 6.7.

As observed, the weak penetration regime is once again accurately described, even though the analytical approximation was derived assuming a constant j_c. In the second part of the fully penetrated regime, the numerical results also align with the analytical approximation, and once again, the loss seems to increase with the ramp rate. However, the behaviour in the intermediate regime is quite complex. The interpolated approximation (Eq. (3.61)) underestimates the loss, as already discussed previously. Remarkably, even the fully penetrated approximation (Eq. (3.59)) underestimates the loss in the first part of the fully penetrated regime, which was not the case in the constant j_c scenario.

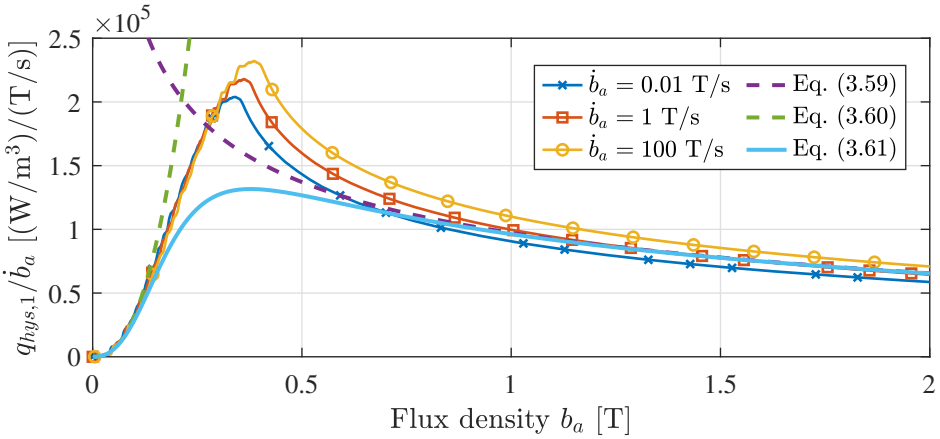

Figure 7.8: Filament hysteresis loss $q_{\text{hys},1}$ during linear field ramp-up (Eq. (7.5)) normalized by the ramp rate $\dot{b}_a$, with $n = 50$, the $j_c(b)$ Bottura relationship and for various ramp rates, compared to analytical predictions based on the CSM.

This discrepancy may be explained by the fact that Eq. (3.59) and Eq. (3.61) evaluate $j_c(b_a)$ based on the external flux density, while the numerical implementation at the filament scale evaluates $j_c(b)$ based on the local flux density b within the superconductor, which is different from b_a due to the filament magnetization. As a consequence, the fully penetrated current density distribution in the filament differs from what has been observed previously, as shown in Fig. 7.9. The $j_c(b = 0.5)$ curve represents the current distribution expected from the CSM at $t = 0.5$ s (in absolute value) neglecting filament magnetization. The flux density is lower in the filament center because of persisting currents, the critical current density is therefore larger.

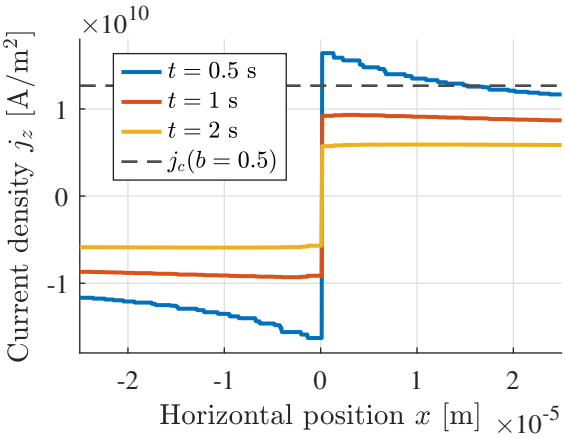

Figure 7.9: Current density j_z computed numerically with $j_c(b)$ along the $\hat{\boldsymbol{x}}$-axis, in $y = 0$ and at different instants, for $\dot{b}_a = 1$ T/s and $n = 50$. Compared to the $j_c(b = 0.5)$ value.

The opposite phenomenon takes place in the outer shell of the filament. Such a behaviour is less observed at higher external fields because the permanent magnetization of the filaments becomes negligible with respect to the applied field.

More generally, the physical phenomena at play are more intricate considering a critical current density depending on flux density. In that context, it is more complex to derive an analytical approximation for the hysteresis loss and the CSM prediction used in Chapter 6 does not provide accurate results in the intermediate range of transverse fields.

7.4 Impact of transport current

In this section, the focus is set on the impact of transport current on the hysteresis loss. Let us again consider a constant $j_c = 5 \times 10^9$ A/m^2. As previously, the exponent is kept at $n = 50$. The aim is to compute the transverse field loss in a filament carrying a fixed DC current I_t. The parameter here is the transport current ratio of the filament $i = I_t/I_c$. Numerically, the state of the superconducting filament is solved for $t \in [0; 5]$ s. The imposed transport current is first established in the system with a linear ramp of 2 s, followed by a stand-by situation of 1 s, before increasing the uniform applied field from $b_a(t = 3\text{ s}) = 0$ T to $b_a(t = 5\text{ s}) = 2$ T at a constant rate of $\dot{b}_a = 1$ T/s as previously. The evolution of the transport current and the applied flux density are respectively:

$$\begin{aligned} I_t(t) &= iI_c\frac{t}{2} \quad \text{for } t \leq 2\text{ s}, \qquad I_t(t) = iI_c \quad \text{for } t > 2\text{ s}, \\ b_a(t) &= 0 \quad \text{for } t \leq 3\text{ s}, \qquad b_a(t) = (t-3) \quad \text{for } t > 3\text{ s}. \end{aligned} \tag{7.8}$$

The current density first enters the filament through its boundary as shown in Fig. 7.10(a). The irregular pattern of smaller current on the interior boundary of the current shell is due to the finite resolution of the spatial discretization. Note that the transport current generates an azimuthal flux density, shown in Fig. 7.10(b), which therefore has a zero normal component on the boundary of the numerical domain.

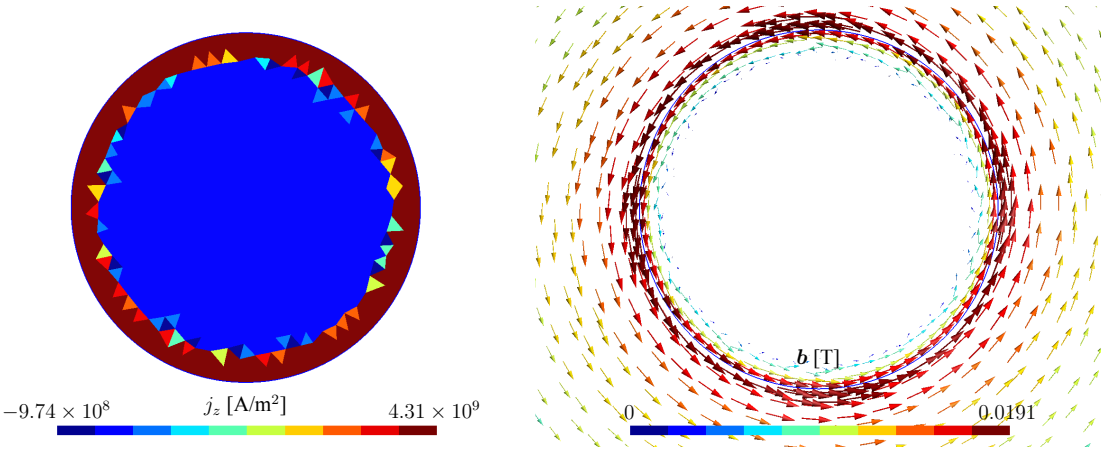

(a) $t = 1.15$ s. (b) $t = 1.15$ s.

Figure 7.10: (a) Current density j_z and (b) flux density $\boldsymbol{b}$ in a filament carrying a positive transport current along the $\hat{\boldsymbol{z}}$-axis. Boundary conditions described by Eq. (7.8), with $n = 50$ and $i = 0.4$.

The filamentary hysteresis loss is represented in Fig. 7.11 for various transport current ratios i. As observed, the hysteresis loss increases with the transport current carried by the filament. In full penetration, the loss is once again constant at fixed field ramp rate. As may be observed in Fig. 7.12(a), the electric field is almost linear in full penetration. The staircase shape of the curves is due to the numerical discretization. Assuming a linear electric field $e_z = (x - x_0)\dot{b}_a$, which is valid if the magnetization of the filament is considered constant, the y-axis of symmetry of the electric field is shifted by some value x_0 [m] along the $\hat{\boldsymbol{x}}$-axis. The current density is then given by $j_z(x - x_0)$ with j_z the distribution of Eq. (7.6). This result is also retrieved numerically in Fig. 7.12(b). The shift x_0 depends on the net transport current I_t and it can be computed by solving the implicit equation:

$$I_t = \int_0^{d_f/2}\int_0^{2\pi} \text{sign}(r\cos\theta - x_0) j_c \left(\frac{|r\cos\theta - x_0|\dot{b}_a}{e_c}\right)^{1/n} r\, d\theta\, dr. \tag{7.9}$$

Such an equation can be solved numerically. Once the shift x_0 is known, the fully penetrated hysteresis loss can be computed from the e_z and j_z distribution through Eq. (3.57). The shift x_0 has a significant impact on the local loss $j_z \cdot e_z$, as shown in Fig.7.12(c). The increase in total hysteresis loss is a direct consequence of x_0, which is itself due to a net transport current. Without going into much detail, the fully penetrated loss computed numerically is close to the $g(i)$ factor derived by Carr (Eq. (3.66)), which is based on the same shift reasoning in the CSM ($n \to \infty$) limit. For $i = 0.8$, the numerical relative loss increase is 1.76 with respect to $i = 0$, compared to $g(0.8) = 1.68$ predicted by Carr. Still for $i = 0.8$, solving Eq. (7.9) yields $x_0 = -0.351\ d_f$ and the integration of the theoretical current and electric field distributions leads to a relative loss increase of 1.754, which much closer to the numerical results.

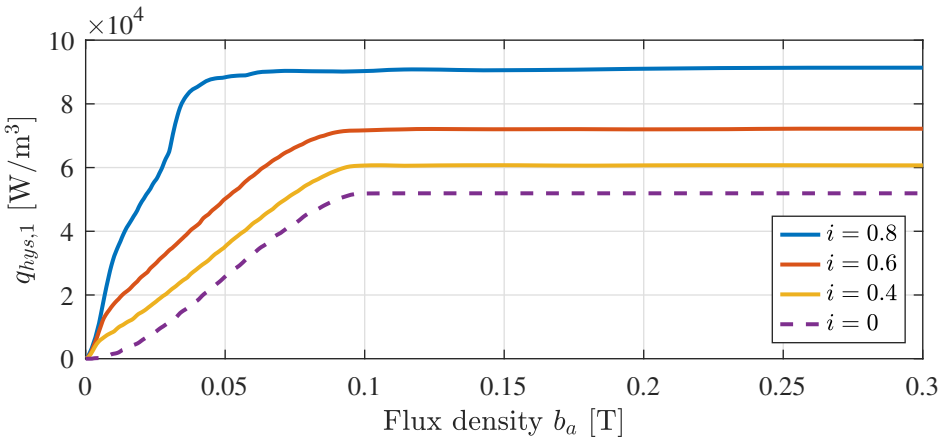

Figure 7.11: Filament hysteresis loss $q_{\text{hys},1}$ in boundary conditions given by Eq. (7.8), with $n = 50$, $j_c = 5 \times 10^9$ A/m^2 and for various transport current ratios i.

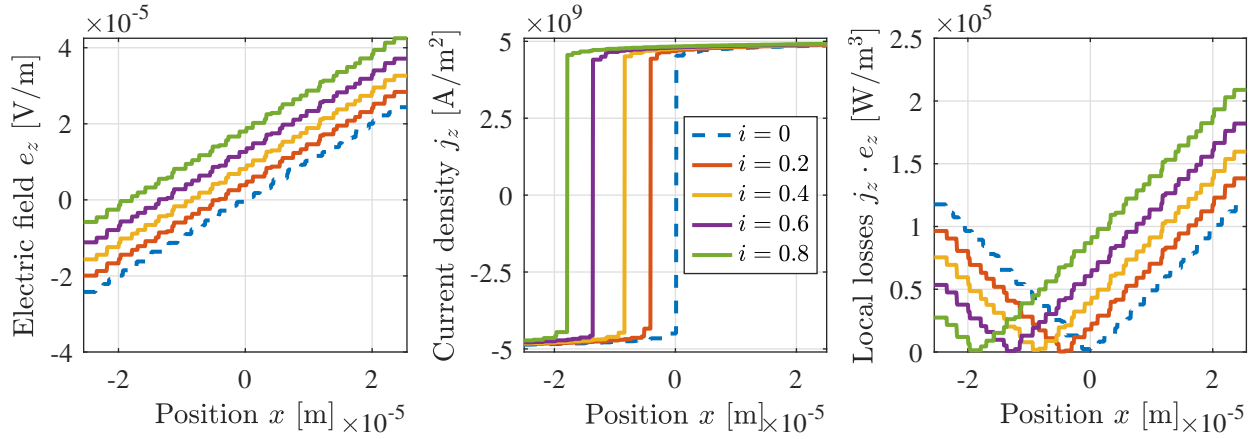

Figure 7.12: Electric field e_z, current density j_z and local losses $q = \boldsymbol{j} \cdot \boldsymbol{e}$ along the $\hat{\boldsymbol{x}}$-axis of the filament, in $y = 0$ and $t = 5$ s for boundary conditions given by Eq. (7.8), $n = 50$ and various transport current ratios i.

On the other hand, Fig. 7.11 highlights a significant increase in loss in weak penetration, even for low transport current ratios. These large losses can be explained by the fact that persistent currents are already established in the filament before the applied field is increased, as shown in Fig. 7.10(a). Moreover, approximating the transport current loss in weak penetration analytically is quite complex. From Fig. 7.8, the full penetration regime is reached at $b \sim 0.3 - 0.5$T, considering the dependence of $j_c(b)$. Consequently, some filaments of the C400 coil may never reach the fully penetrated regime, as inferred from Fig. 6.6(b). Thus, the interpolated analytical approximation used in Chapter 7, which neglected the transport current, may have underestimated the hysteresis loss.

7.5 Application in realistic conditions

So far, only simple academic problems have been considered in this chapter. Let us now focus on more realistic boundary conditions. In particular, for each of the four positions indicated in Fig. 6.4(b), the filament model is simulated with the flux density computed from the macroscopic model as the external flux density $\boldsymbol{b}_a$, while the filament transport current is assumed to increase linearly over time. The flux density was computed in the axisymmetric geometry with $\Delta t = 20$ s and $s = 0.12$. Note that the filament model also takes the direction of the applied field into account by considering the evolution of each component of $\boldsymbol{b}_a$ individually. The transport current carried by the filament is also taken into account, assuming a filament current equal to the conductor current divided by the number of filaments. The evolution of the flux density norm is represented in Fig. 6.6(b), and the corresponding hysteresis loss per unit volume, computed from Eq. (3.61), is shown in Fig. 6.6(a). The results obtained with the filament model ($n = 50$) are shown in Fig. 7.13. Note that $q_{\text{hys}} = \lambda_{\text{SC}} q_{\text{hys},1}$ is represented in contrast with the previous graphs of this chapter.

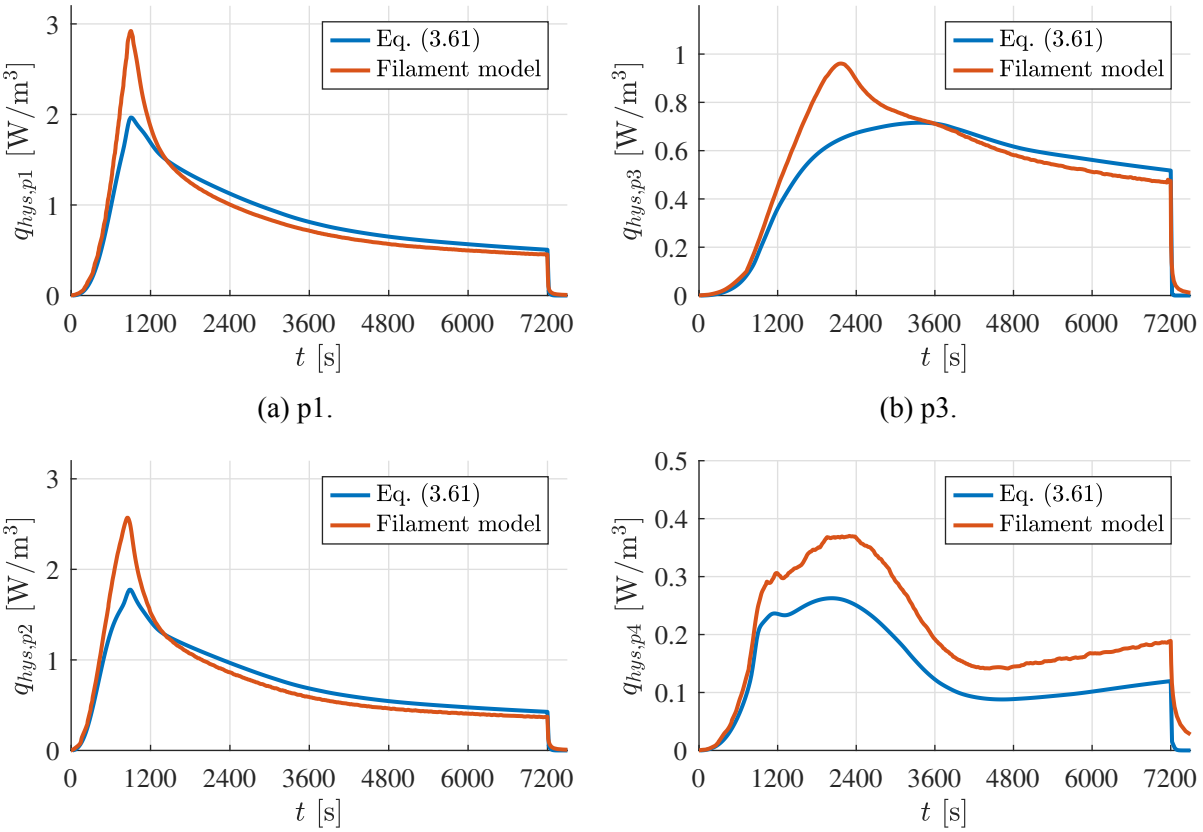

(a) p1. (b) p3.

(c) p2. (d) p4.

Figure 7.13: Hysteresis loss computed from the filament model with $n = 50$ at the four points indicated in Fig. 6.4(b) compared to the analytical approximation of Eq. (3.61).

As observed, there is a significant difference between the analytical approximation and the numerical results. The relative difference of the analytical approximation used in the previous chapters is quite important as it is around ~ 40 % in the worst conditions. The first three graphs in Fig. 7.13 can be interpreted similarly. In weak penetration, the analytical approximation is accurate. In the intermediate regime, the loss is underestimated as highlighted multiple times in this chapter. Also, the critical current dependence on flux density tends to further increase the numerical hysteresis loss in the intermediate regime, compared to the analytical approximation. Once the filament is fully penetrated, the numerical loss is lower than the analytical approximation, even though it takes

the transport current into account. This may be explained by the low field variation rate in the coil, around $\dot{b} \sim 3/7200 \sim 4 \times 10^{-4}$ T/s. In full penetration, the induced electric field is thus significantly lower than the critical electric field e_c, leading to a lower loss as emphasized by the last factor in Eq. (7.7).
As already discussed in Chapter 6, the flux density reaches the threshold value $b \sim 0.38$ T sooner in the left part of the coil. This explains why the loss peak appears earlier and why the losses are greater compared to the p3 point, as there is a larger field variation.
The behaviour of the loss in the p4 point is more complex to discuss. As shown in Fig. 6.6(b), the flux density never exceeds $b \sim 0.41$ T and thus the filament cannot be considered fully penetrated. In that context, the signifant loss increase computed with the numerical model may also be explained by the impact of transport current as discussed in the previous section.

Conclusion of the chapter

The aim of this chapter has been to introduce a numerical model for computing the hysteresis loss at the filament scale. As such, the limitations of the analytical approximation used in Chapter 6 have been highlighted. Although it may be accurate in weak penetration when the transport current is negligible, the losses in the intermediate regime have been underestimated. Furthermore, the power-law model introduced an additional dependence of the losses on the ramp rate and on the power-law exponent. This effect was quantified in the fully penetrated regime, for which an analytical approximation of the hysteresis loss was derived in the present study. This allowed the validation of the filament model, as the numerical results were very close to the analytical prediction. However, the critical current dependence on the flux density further increased the complexity of the physical phenomena involved and analytical approximations could no longer be derived. The transport current was shown to have a significant effect on the loss in weak penetration and the physical origin of the relative loss increase when taking transport current into account was also discussed.

Finally, the numerical results were compared to analytical approximations in real flux density conditions obtained from a magnetodynamic computation at the macroscopic scale. The relative difference was quite large, highlighting the need for a numerical model at the filament scale. The physics of hysteresis losses in superconducting filaments is complex and depends on many physical parameters. Although the temperature dependence and the coupling between filaments have been neglected in this chapter, the filament model allowed the variation of the potentially rotating local flux density inside the coil to be taken into account, while considering the net transport current inside the filament and the critical current density dependence on flux density. In the next chapter, the robustness of the filament model is exploited and it is coupled to the magnetodynamic resolution at the macroscopic scale, enabling a more precise prediction of hysteresis losses during ramp-up.

CHAPTER 8

MULTI-SCALE APPROACH

As emphasized in Chapter 6, the hysteresis loss plays a fundamental role in the magnetothermal behaviour of the coil. In Chapter 7, the limitations of the analytical approximation for predicting hysteresis losses were highlighted, using a filament model. In this final chapter, the filament model is coupled with the macroscopic magnetothermal model presented in Chapter 6. The hysteresis losses are computed at the filament scale, which allows for a more robust resolution since the filament model has been validated in Chapter 7. The aim of this chapter is to increase the accuracy of the maximal temperature evolution in the coil obtained numerically. First, the implementation of the multi-scale approach is presented. The sensitivity of the results to the single numerical parameter of the approach is again briefly investigated. The final results are then discussed, both in the axisymmetric geometry and in the full cyclotron geometry. Furthermore, the losses computed from the filament scale are compared with those predicted from the analytical approximation.

8.1 Description of the method

For the purpose of the multi-scale approach, the coil is subdivided into N_z zones, which are represented in Fig. 8.1 and respectively denoted by $\Omega_{\text{fil},i}$. As discussed next, the first step of the multi-scale procedure is to retrieve the mean flux density variation in each of the N_z zones. Since the flux density variations are much more pronounced within the coil cross-section than along the azimuthal axis, it was decided to split the coil into several concentric rings.

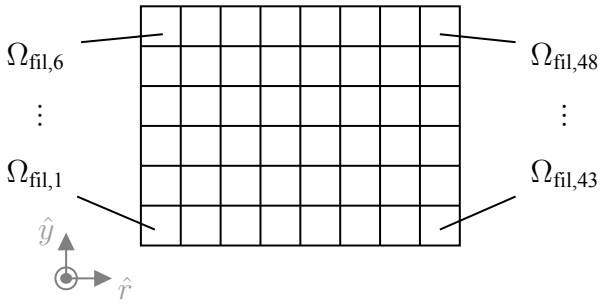

Figure 8.1: Subdivision of the coil cross-section into N_z zones, respectively denoted by $\Omega_{\text{fil},1}$, ...,Ω_{fil,N_z}, in the particular case $N_z = 48$.

This allows a representative mapping of the flux density distribution within the coil to be obtained. The proposed multi-scale resolution scheme for computing the temperature distribution in the coil is summarized in Fig. 8.2. First, the flux density distribution in the coil is obtained from the magnetodynamic solver described in Chapter 4, relying on the a-formulation. Then, the volume average flux density $\bar{\boldsymbol{b}}(t)$ is computed in each of the N_z zones as a function of time. In particular, the radial $\bar{b}_r$ and vertical $\bar{b}_y$ components are computed independently.

The second step of the multi-scale procedure is to compute the response of one filament per zone $\Omega_{\text{fil},i}$, based on the filament model described in Chapter 7 relying on the h-ϕ formulation. In each zone, the mean flux density evolution from the previous macroscopic resolution is applied as a boundary condition to the outer boundary of the filament model. Since the radius of curvature of

the filaments is neglected, the radial component $\bar{b}_r$ is applied along the $\hat{\boldsymbol{x}}$ local axis of the filament in Fig. 7.2. In each zone, the local filament transport current $\bar{I}_\mathrm{t}(t)$ is assumed to be the conductor current divided by the number of filaments N_f per conductor. It increases linearly with time during the ramp-up procedure. As explained in Section 3.3.2, the critical current density depends on temperature. In first approximation, the temperature is assumed to be $T = T_\mathrm{He}$. From these inputs, the average filamentary hysteresis loss $\bar{q}_{\mathrm{hys},1}(t)$ is computed numerically, again as a function of time.
In the third and final step of the procedure, the temperature distribution in the coil is computed from the hysteresis loss, based on the thermal model of the coil described in Chapter 5, denoted by the T-formulation in Fig. 8.2. In each zone $\Omega_{\mathrm{fil},i}$, the volumetric heat source is $q_\mathrm{s} = q_\mathrm{c} + \lambda_\mathrm{SC}\bar{q}_{\mathrm{hys},1}$, where inter-filamentary coupling loss q_c is taken from the magnetodynamic computation.
An optional feedback loop could then be implemented. From the thermal computation, the mean temperature evolution $\bar{T}(t)$ in each zone could be extracted and sent back to the corresponding filament model. An iterative procedure could then take place with the filament models and the macroscopic model communicating until some stopping criterion on the integrated hysteresis loss Q_hys is met. At this point, the temperature distribution could be retrieved from the last iteration of the multi-scale procedure. In this study, since the temperature increase in the C400 is less than $\Delta T_\mathrm{max} = 0.01$ K, the variation of the critical current density with temperature has been neglected. Therefore, the focus is on the accurate numerical prediction of the hysteresis losses that occur within the coil during ramp-up. Note that the twisting of filaments, as well as the coupling between filaments, is neglected at the filament scale.
In summary, the multi-scale resolution takes a ramp-up profile as an input and provides the corresponding temperature distribution within the coil as an output.

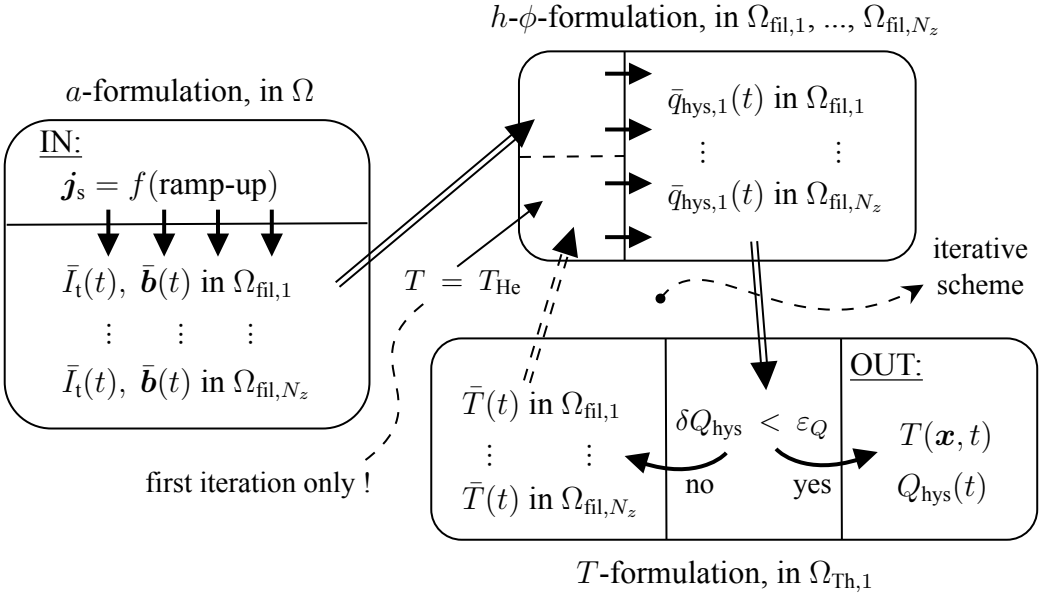

Figure 8.2: Flowchart of the multi-scale approach for computing the temperature field in the coil based on hysteresis losses retrieved from the filament model.

Note that with the mesh presented in Fig. 7.1 of Chapter 7, a simulation at the filament scale takes on average 45 minutes of CPU time. In this chapter, the adaptive time step of the filament model is constrained to not exceed 50 s for numerical stability and a power-law exponent of $n = 50$ has been assumed for all computations. The critical current density $j_\mathrm{c}(b, T)$ dependence is modelled with Bottura's relationship described in Section 3.3.2.

8.2 Impact of the domain discretization

The only numerical parameter to be studied in this chapter is the number of zones N_z used to discretize the coil cross-section, as represented in Fig. 8.1. The integrated hysteresis loss is shown in Fig. 8.3 for an increasing number of zones, in the axisymmetric geometry. The oscillations in the hysteretic loss for $N_z = 1$ can be explained by the mesh discretization of the filament model as discussed in Chapter 7. As expected, the results converge as the number of zones increases. In particular, the energy $E_{\text{hys}} = \int_0^{+\infty} Q_{\text{hys}}(t)\, dt$ dissipated in the form of hysteresis loss converges monotonically as highlighted in Tab. 8.1. Such a behaviour is also expected since averaging the flux density in the different zones will smooth out the flux density variations and thus reduce the hysteresis loss. As the number of zones increases, the effect of volume averaging decreases. The relative difference in dissipated energy E_{hys} between $N_z = 12$ and $N_z = 48$ is 0.72 %. For the following simulations, the number of zones is set to $N_z = 48$: 8 zones along the $\hat{\boldsymbol{r}}$-axis of the coil and 6 along its $\hat{\boldsymbol{y}}$-axis.

N_z	[-]	1	4	12	48
E_{hys}	[J]	4413	5037	5470	5510

Table 8.1: Total energy E_{hys} dissipated in the form of hysteresis loss during ramp-up for various N_z, in the axisymmetric geometry.

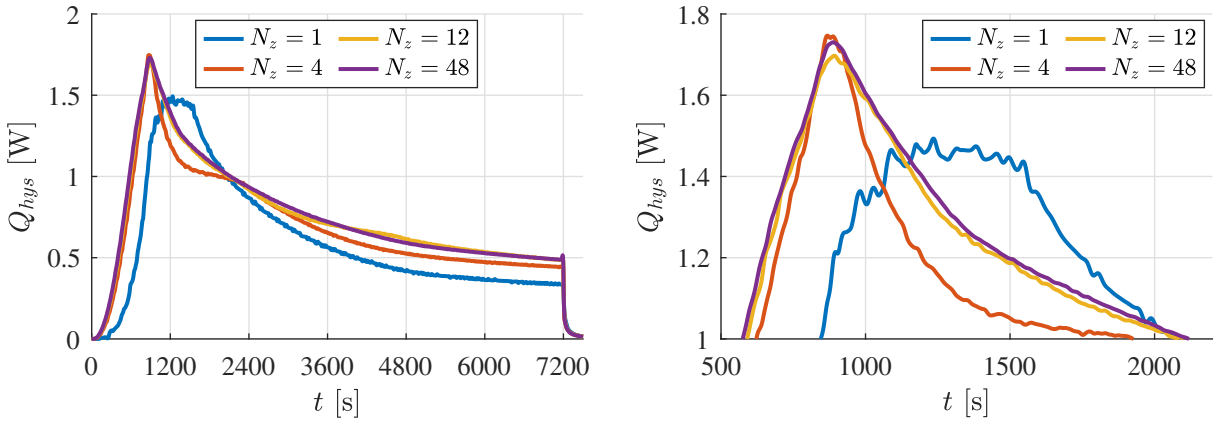

Figure 8.3: Integrated hysteresis loss Q_{hys} computed with the multi-scale approach, based on a 2D axisymmetric simulation with $s = 0.12$ and $\Delta t = 20$ s, for various number of zones N_z.

8.3 Main results

The integrated hysteresis loss Q_{hys} computed from the multi-scale approach is shown in Fig. 8.4, both in the 2D axisymmetric geometry and in the three-dimensional geometry. The results are compared to the macroscopic results presented in Chapter 6, where the hysteresis loss was computed based on Eq. (3.61). As can be seen in Fig. 8.4, the peak hysteresis loss was underestimated by the macroscopic computation. As discussed several times in Chapter 7, this is a direct consequence of the analytical approximation not being sufficiently accurate in the intermediate field regime. The peak hysteresis loss is given by $Q_{\text{hys}} = 1.728$ W and $Q_{\text{hys}} = 1.457$ W in 2D and in 3D respectively, yielding an increase of 29 % and 24 % compared to the results of Chapter 6. In the second part of the ramp-up procedure, the numerical hysteresis loss is lower than that predicted by Eq. (3.61). Such a behaviour is also expected because the induced electric field in the fully penetrated regime of the filaments is much smaller than the critical electric field, thus reducing the power loss as quantified in the previous chapter. The different observations are similar in both geometries. As discussed in Section 6.3, the 3D results are smoothed out in comparison to the axisymmetric results.

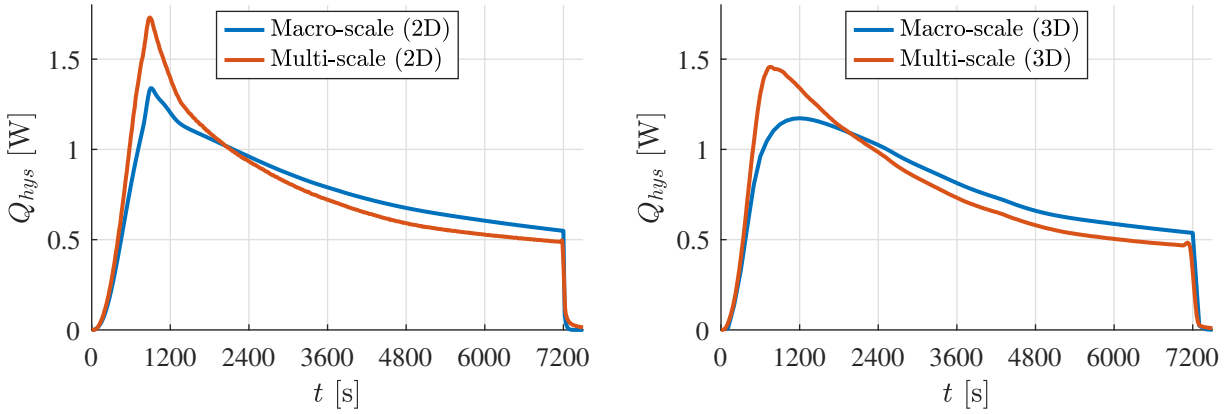

Figure 8.4: Evolution of the integrated hysteresis loss Q_{hys} computed with the multi-scale approach, (a) 2D axisymmetric results ($s = 0.12$, $\Delta t = 20$ s) and (b) 3D results ($s = 0.84$, $\Delta t = 100$ s), compared to the results of Chapter 6 based on Eq. (3.61) (macro-scale).

Overall, the discussion in Section 7.5, interpreting the results in Fig. 7.13(a-b-c), is still valid in the present context and can be applied to the hysteresis loss integrated over the volume of the coil. The evolution of the average flux density in different zones of the coil is gathered in Appendix B.3, together with the corresponding hysteresis loss obtained from the multi-scale resolution. The different zones are shown in Fig. B.2. The peak hysteresis loss in the regions of the coil closer to the cyclotron center was indeed underestimated by the analytical approximation. The same conclusion holds for the zones $\{8, 16, 32, 35\}$ corresponding to the upper and central parts of the coil. However, some peculiar phenomena can be observed in the lower right part of the coil cross-section. As mentioned in Section 4.7.3, the low field region moves downward over time. In particular, the zero field region crosses the zone 39 during the ramp-up procedure. The evolution of the corresponding average flux density is also represented in Appendix B.3. Since the low field region crosses the zone during ramp-up, the flux density and its variation are remarkably low. There is a significant difference between the hysteresis loss computed from the multi-scale resolution and the analytical approximation. This can be explained by the current density distribution in the filament and the corresponding flux density, which are shown in Fig. 8.5, at $t = 7200$ s.

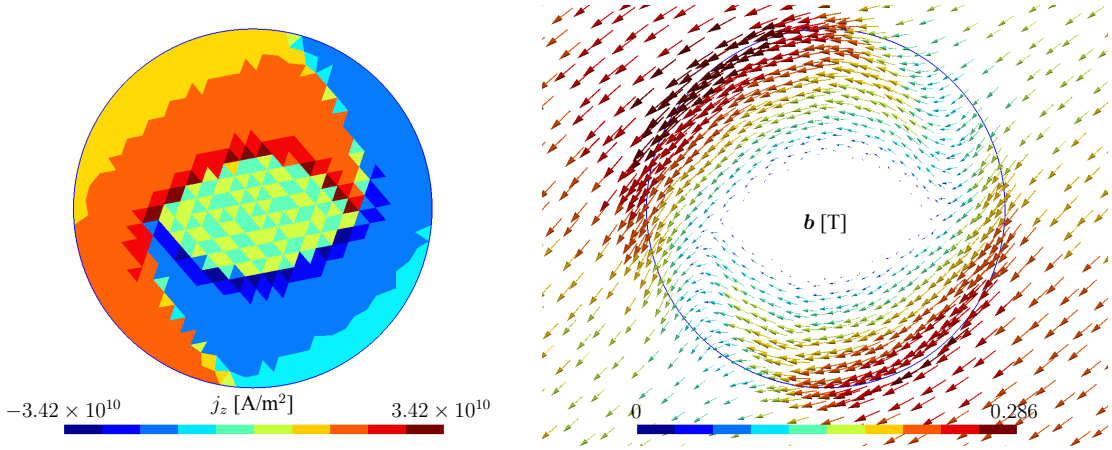

(a) $t = 7200$ s. (b) $t = 7200$ s.

Figure 8.5: (a) Current density and (b) induced flux density in the filament of zone 39 at $t = 7200$ s, retrieved from the multi-scale resolution based on a 3D magnetodynamic simulation with $s = 0.84$ and $\Delta t = 100$ s.

As observed in Fig. 8.5, the filament never reaches the fully penetrated regime, due to the particularly low flux density in zone 39. Moreover, the flux density rotates around the zero field region crossing the zone. Consequently, the final distribution of persistent currents in the superconducting filament is remarkable. A similar distribution of field lines has also been obtained numerically by Prigozhin [53]. He studied a cylindrical superconductor with square cross-section subjected to a perpendicular field which increases but remains in the weak penetration regime and then rotates. The physical mechanisms at play are quite complex. In particular, the assumptions of the CSM prediction introduced in Section 3.5 are not valid in such a configuration and the analytical approximations fail to provide consistent results. These observations again highlight the importance of modelling the magnetic behaviour of filaments using a multi-scale resolution for predicting hysteresis losses in the C400 coil.

Last but not least, the maximal coil temperature evolution computed from the multi-scale resolution is shown in Fig. 8.6. In the axisymmetric geometry, the maximal temperature rise ΔT_{max} is increased by 35.7 % compared to the previous results of Chapter 6 and reaches $\Delta T_{\text{max}} = 0.0114$ K. In the full three-dimensional geometry of the C400, the maximal temperature rise in the coil is $\Delta T_{\text{max}} = 0.0101$ K, corresponding to a 36.5% relative increase with respect to the macroscopic resolution. As is the case for the hysteresis loss, the maximal temperature was previously underestimated by the macroscopic model. Also, the temperature is lower than what has been predicted in Chapter 6 during the second part of the ramp-up procedure. Again, the similarity between the temperature evolution and the hysteresis loss evolution is remarkable. This has been discussed in Chapter 6. Still, the temperature rise in the coil is not significant and the Nb-Ti filaments should effectively remain in the superconducting state during ramp-up. Nevertheless, the multi-scale resolution allowed to increase the accuracy of the numerical prediction. The next step should be to measure the hysteresis loss experimentally to validate the numerical results. A practical solution for doing so would be to measure the enthalpy variation of the liquid helium used for cooling.

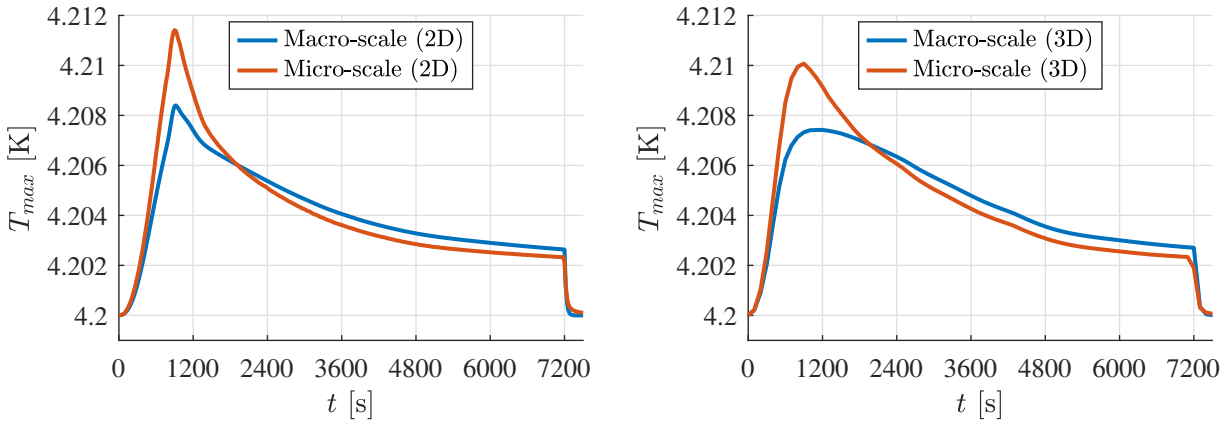

Figure 8.6: Evolution of the maximal coil temperature T_{max} computed with the multi-scale approach, (a) 2D axisymmetric results ($s = 0.12$, $\Delta t = 20$ s) and (b) 3D results ($s = 0.84$, $\Delta t = 100$ s), compared to the results of Chapter 6 (macro-scale).

As a conclusion to this chapter, the multi-scale approach for computing hysteresis losses has been successfully implemented in the context of the C400 coil. As a result, the numerical resolution is more robust than that discussed in Chapter 6 and complex phenomena can now be modelled in the Nb-Ti filaments. The proposed approach is quite general and it could be extended to other composite superconducting coil.

CONCLUSION AND PERSPECTIVES

In this thesis, a numerical model has been developed to predict the magnetothermal behaviour of the superconducting coil during the ramp-up of the C400 cyclotron. After describing the context and defining the problem and its geometry in the first two chapters, the theoretical background and a literature review were presented in detail in Chapter 3. In particular, an approximation for the hysteresis loss in Nb-Ti filaments in the weakly penetrated regime was derived based on the CSM. An interpolated analytical approximation was then proposed for the full range of applied transverse flux densities, neglecting the transport current in the filaments.

Chapter 4 introduced the magnetic model of the cyclotron, in which the coil was homogenized and approximated as a stranded conductor. Various numerical parameters, such as the time step and the mesh size, were fine-tuned for optimal efficiency. The consistency of the results obtained with models of increasing complexity was demonstrated, while the need to include the spiralized poles and the off-center vertical holes in the final model was also highlighted. The thermal model of the coil was introduced in Chapter 5. In particular, the natural domain decomposition between the coil and the surrounding helium vessel and the corresponding boundary conditions were discussed. Since the coil was homogenized, its effective thermal properties were derived. Finally, the large Biot number regime allowed the determination of the thermal time constant of the coil ($\tau_{\text{th}} \sim 10$ s), which was confirmed by numerical results.

The coupled magnetothermal model was described in Chapter 6. Again, the numerical parameters were varied until the convergence of the results was found to be satisfactory. As discussed, the impact of the helium vessel on the numerical results is not significant and it can be disregarded in the final model. The central role played by hysteresis losses in the magnetothermal behaviour of the coil was highlighted as the inter-filament coupling losses were found to be negligible. In this context, the large Biot number regime leads to a temperature rise that is directly proportional to the hysteresis loss since the thermal time constant is much smaller than the ramp-up time. Accordingly, the maximal temperature rise of $\Delta T_{\text{max}} = 0.0074$ K obtained numerically was expected from dimensional analysis. In Section 6.4, the convective heat transfer coefficient was varied over several orders of magnitude and even with an excessively small convective coefficient, the Nb-Ti filaments still remain in the superconducting state. Similarly, reducing the ramp time to 6 minutes leads to a temperature rise of $\Delta T_{\text{max}} = 0.16$ K. However, due to the limited voltage difference available at the power source terminals, it was found that the linear ramp-up procedure could not be performed in less than 20 minutes. Two solutions were then proposed to reduce the temperature rise in the coil: reducing the diameter of the Nb-Ti filaments and adjusting the current ramp profile based on the physical interpretation of hysteresis losses. The second, more practical solution reduced the temperature rise by 14 %.

In Chapter 7, it was decided to further investigate the transverse field hysteresis losses with a filament model, as they determine the magnetothermal behaviour of the coil. The model was adapted to consider both the transport current and the time variation of an external transverse flux density. The analytical approximation used in the previous chapters was found to underestimate the loss in the intermediate field range. While simplified academic problems allowed analytical solutions to be derived to validate the numerical implementation, the complexity of the physical phenomena involved was highlighted. In particular, the critical current density dependence on the flux density and the effect of the transport current cannot be neglected. In this context, the limitations of analytical approximations in realistic flux density conditions have been demonstrated.

Finally, the filament model was coupled with the macroscopic model discussed in Chapter 6, as a multi-scale approach for computing hysteresis loss was proposed and implemented in Chapter 8. Based on the flux density evolution obtained from a magnetodynamic computation at the macroscopic scale, the hysteresis loss is determined at the filament scale, allowing the temperature distribution to be computed with greater accuracy since more realistic phenomena can be modelled at the filament scale. Based on the multi-scale approach, the effective temperature rise in the three-dimensional coil was found to be $\Delta T_{\text{max}} = 0.0101$ K. Consequently, the Nb-Ti filaments should remain in the superconducting state during a regular ramp-up procedure.

Some of the results discussed in Chapters 7 and 8 were presented at the 14th International Particle Accelerator Conference in Venice last May [54].

Further improvements and perspectives

The analysis carried out in this thesis could be further extended in several ways:

- Although negligible in the context of the C400 coil, inter-filament coupling losses could be investigated at the filament scale in a similar way to hysteresis losses. Twisted filaments could be modelled using an equivalent two-dimensional model based on a helicoidal transformation method as already introduced in [7].
- In addition to the magnetic response of the filaments, their thermal response could be studied at the microscopic scale by modelling the transient heat conduction in the Nb-Ti filaments, together with the corresponding heat transfer at the interface with the copper matrix. Furthermore, a magnetothermal model at the filament scale could be developed to describe complex phenomena such as quench propagation.
- Among other possibilities, the finite element model at the filament scale could be replaced by a machine learning algorithm. In particular, recurrent neural networks have proven very successful in multi-scale modelling for nonlinear mechanics [55]. Such methods could be adapted to model the hysteretic behaviour of superconductors, potentially increasing the computational efficiency of the multi-scale resolution presented in this thesis. Including machine learning in magnetic finite element simulations looks promising as it has already been applied for modelling stacks of ferromagnetic laminations [56].

APPENDIX A

MATHEMATICAL NOTATIONS AND DEVELOPMENTS

A.1 Mathematical notations

This section gathers the different mathematical notations used throughout the work:

- Vector $\boldsymbol{u}$ component along $\hat{\boldsymbol{x}}$-axis:
$$u_x = \boldsymbol{u} \cdot \hat{\boldsymbol{x}}. \tag{A.1}$$
- Norm of vector $\boldsymbol{u}$:
$$u = \|\boldsymbol{u}\| = \sqrt{u_x^2 + u_y^2 + u_z^2}. \tag{A.2}$$
- Partial derivative of u with respect to x:
$$\partial_x u = \frac{\partial u}{\partial x}. \tag{A.3}$$
- Volume inner product of vector fields $\boldsymbol{a}$ and $\boldsymbol{b}$ in Ω and volume inner product of scalar fields c and d in Ω, respectively:
$$(\boldsymbol{a}, \boldsymbol{b})_\Omega = \int_\Omega \boldsymbol{a} \cdot \boldsymbol{b} \, d\Omega, \quad (c, d)_\Omega = \int_\Omega c \, d \, d\Omega. \tag{A.4}$$
- Surface inner product of vector fields $\boldsymbol{a}$ and $\boldsymbol{b}$ on Γ and surface inner product of scalar fields c and d on Γ, respectively:
$$\langle \boldsymbol{a}, \boldsymbol{b} \rangle_\Gamma = \int_\Gamma \boldsymbol{a} \cdot \boldsymbol{b} \, d\Gamma, \quad \langle c, d \rangle_\Gamma = \int_\Gamma c \, d \, d\Gamma. \tag{A.5}$$

A.2 Definition of function spaces

Vector potential formulation

Similarly to what is done in [7], we seek a solution $\boldsymbol{a}$ in the function space

$$\mathcal{A}(\Omega) = \left\{ \boldsymbol{a} \in H(\nabla\times;\Omega) \mid \boldsymbol{a} \text{ is gauged in } \Omega_{\mathrm{c}}^{\mathrm{C}}, (\boldsymbol{a} - \bar{\boldsymbol{a}}) \times \boldsymbol{n} = \boldsymbol{0} \text{ on } \Gamma_e \right\}, \tag{A.6}$$

with

$$H(\nabla\times;\Omega) = \left\{ \boldsymbol{a} \in \boldsymbol{L}^2(\Omega) \ : \ \nabla \times \boldsymbol{a} \in \boldsymbol{L}^2(\Omega) \right\}, \tag{A.7}$$

in which the curl ($\nabla\times$) must be understood in the sense of distributions and $\boldsymbol{L}^2(\Omega)$ denotes the vector space of square integrable vector fields on Ω. Likewise, an auxiliary function space used for test functions $\boldsymbol{a}^{'}$ is introduced:

$$\mathcal{A}_0(\Omega) = \left\{ \boldsymbol{a}^{'} \in H(\nabla\times;\Omega) \mid \boldsymbol{a}^{'} \text{ is gauged in } \Omega_{\text{c}}^{\text{C}}, \boldsymbol{a}^{'} \times \boldsymbol{n} = \boldsymbol{0} \text{ on } \Gamma_e \right\}. \tag{A.8}$$

Magnetic field formulation

Again, similarly to what is done in [7], we seek a solution $\boldsymbol{h}$ in the function space

$$\mathcal{H}(\Omega) = \left\{ \boldsymbol{h} \in H(\nabla\times;\Omega) \mid \nabla \times \boldsymbol{h} = 0 \text{ in } \Omega_{\text{c}}^{\text{C}}, (\boldsymbol{h} - \bar{\boldsymbol{h}}) \times \boldsymbol{n} = \boldsymbol{0} \text{ on } \Gamma_h, \mathcal{I}(\boldsymbol{h}) = \bar{I}_{\text{t}} \right\}. \tag{A.9}$$

The auxiliary function space used for test functions $\boldsymbol{h}^{'}$ is:

$$\mathcal{H}_0(\Omega) = \left\{ \boldsymbol{h}^{'} \in H(\nabla\times;\Omega) \mid \nabla \times \boldsymbol{h}^{'} = 0 \text{ in } \Omega_{\text{c}}^{\text{C}}, \boldsymbol{h}^{'} \times \boldsymbol{n} = \boldsymbol{0} \text{ on } \Gamma_h, \mathcal{I}(\boldsymbol{h}^{'}) = 0 \right\}. \tag{A.10}$$

Thermal formulation

We seek a solution T in the function space

$$\mathcal{T}(\Omega_{\text{th}}) = \left\{ T \in H^1(\Omega_{\text{th}}) \mid T = \bar{T} \text{ on } \Gamma_{\text{th}}^D \right\}, \tag{A.11}$$

with

$$H^1(\Omega_{\text{th}}) = \left\{ T \in L^2(\Omega_{\text{th}}) \ : \ \nabla T \in \boldsymbol{L}^2(\Omega_{\text{th}}) \right\}, \tag{A.12}$$

in which the gradient (∇) must be understood in the sense of distributions and $L^2(\Omega_{\text{th}})$ denotes the vector space of square integrable scalar fields on Ω_{th}. Likewise, an auxiliary function space used for test functions $T^{'}$ is introduced:

$$\mathcal{T}_0(\Omega_{\text{th}}) = \left\{ T^{'} \in H^1(\Omega_{\text{th}}) \mid T^{'} = 0 \text{ on } \Gamma_{\text{th}}^D \right\}. \tag{A.13}$$

A.3 Derivation of the thermal weak formulation

The thermal weak formulation is obtained by multiplying Eq. (3.49) by a test function $T^{'} \in \mathcal{T}_0(\Omega_{\text{th}})$, taking Eq. (3.49) into account and integrating over the domain Ω_{th}. Taking advantage of the notations introduced in Appendix A.1, it comes:

$$(\rho_V c_p \, \partial_t T, T^{'})_{\Omega_{\text{th}}} - (\nabla \cdot (\boldsymbol{\kappa} \cdot \nabla T), T^{'})_{\Omega_{\text{th}}} = (q_{\text{s}}, T^{'})_{\Omega_{\text{th}}}. \tag{A.14}$$

From Green's identity, the second term becomes

$$-(\nabla \cdot (\boldsymbol{\kappa} \cdot \nabla T), T^{'})_{\Omega_{\text{th}}} = (\boldsymbol{\kappa} \cdot \nabla T, \nabla T^{'})_{\Omega_{\text{th}}} - \langle (\boldsymbol{\kappa} \cdot \nabla T) \cdot \boldsymbol{n}, T^{'} \rangle_{\Gamma_{\text{th}}}. \tag{A.15}$$

The surface term, taking Fourier's law (Eq. (3.50)) and $\Gamma_{\text{th}} = \Gamma_{\text{th}}^D \cup \Gamma_{\text{th}}^N \cup \Gamma_{\text{th}}^R$ into account, can be simplified to

$$\begin{aligned}
-\langle (\boldsymbol{\kappa} \cdot \nabla T) \cdot \boldsymbol{n}, T^{'} \rangle_{\Gamma_{\text{th}}} &= \langle \boldsymbol{q}^{''} \cdot \boldsymbol{n}, T^{'} \rangle_{\Gamma_{\text{th}}} && \text{(A.16)} \\
&= \langle \boldsymbol{q}^{''} \cdot \boldsymbol{n}, \underbrace{T^{'}}_{=0} \rangle_{\Gamma_{\text{th}}^D} + \langle \underbrace{\boldsymbol{q}^{''} \cdot \boldsymbol{n}}_{=\bar{\boldsymbol{q}}^{''} \cdot \boldsymbol{n}}, T^{'} \rangle_{\Gamma_{\text{th}}^N} + \langle \underbrace{\boldsymbol{q}^{''} \cdot \boldsymbol{n}}_{=\bar{f}(T)}, T^{'} \rangle_{\Gamma_{\text{th}}^R} && \text{(A.17)} \\
&= \langle \bar{\boldsymbol{q}}^{''} \cdot \boldsymbol{n}, T^{'} \rangle_{\Gamma_{\text{th}}^N} + \langle \bar{f}(T), T^{'} \rangle_{\Gamma_{\text{th}}^R}. && \text{(A.18)}
\end{aligned}$$

Dirichlet boundary conditions have been imposed strongly while Neumann and Robin boundary conditions are weakly satisfied. All in all, Eq. (A.14) reduces to

$$(\rho_V c_p \, \partial_t T, T^{'})_{\Omega_{\text{th}}} + (\boldsymbol{\kappa} \cdot \nabla T, \nabla T^{'})_{\Omega_{\text{th}}} + \langle \bar{\boldsymbol{q}}^{''} \cdot \boldsymbol{n}, T^{'} \rangle_{\Gamma_{\text{th}}^N} + \langle \bar{f}(T), T^{'} \rangle_{\Gamma_{\text{th}}^R} = (q_{\text{s}}, T^{'})_{\Omega_{\text{th}}}. \tag{A.19}$$

A.4 Validity of the MQS approximation

As described in [2], the magneto-quasi-static (MQS) approximation is valid as long as the dimension l of the system is much lower than the electromagnetic wavelength λ_{em}. If the C400 ramp-up (2 hours) is approximated by a quarter of a sine period, the wave period is 8 hours: $T_{\text{em}} = 4t_{\text{up}} = 28800$ s. The corresponding wavelength is

$$\lambda_{\text{em}} = c \cdot T_{\text{em}} = \frac{T_{\text{em}}}{\sqrt{\varepsilon_0 \mu_0 \mu_r}} \geq 1.14 \times 10^{11} \text{ m}. \tag{A.20}$$

This result has been obtained considering (in the worst case) a relative permeability of $\mu_r = 5696$ given by the maximal relative permeability of the ferromagnetic iron yoke (cf. Section 3.2). Obviously, the diameter of the C400 ($\sim$ 7 m) (cf. Chapter 2) is much lower than λ_{em} and the MQS approximation is valid in the present study.

A.5 Validity of the stranded conductor approximation

As described in [6], the stranded conductor approximation is valid for a winded conductor of diameter smaller than the skin depth $\delta = \sqrt{2/\omega\mu\sigma}$, in [m].
In the superconducting coil, the current is almost exclusively conducted through the superconducting filaments, of diameter $d_f = 51$ µm.
The computation of the skin depth relies on further approximations:

- The 2 hours ramp-up corresponds to one quarter of a sine period of $T_{\text{em}} = 28880$ s.
- Even though the electrical conductivity is not constant in the superconducting filaments (cf. power-law, Section 3.3.4), it is approximated as $\sigma = j_{\text{c}}/e_{\text{c}}$. The critical current density is also not constant (cf. Section 3.3.2). From a conservative point of view, it is evaluated at $b = 0.5$ T and $T = 4.2$ K: $j_{\text{c}} \approx 1.27 \times 10^{10}$ A/mm^2.
- In good approximation, $\mu = \mu_0$ in Nb-Ti.

In that context, the skin depth is

$$\delta \approx \sqrt{\frac{2T_{\text{em}}e_{\text{c}}}{2\pi\mu_0 j_{\text{c}}}} = 7.6 \text{ mm} \gg d_f. \tag{A.21}$$

Hence, the stranded conductor assumption is valid in first approximation.

A.6 Cylindrical to Cartesian change of coordinate system

In the present study, the cylindrical coordinate system is defined as

$$x = r\cos(\theta), \quad y = y, \quad z = r\sin(\theta), \tag{A.22}$$

meaning that $\theta \in [-\pi/2; 0]$ is negative as represented in Fig. A.1.
Let us apply the change of coordinates in the context of the thermal conductivity tensor of the coil. In cylindrical coordinates, Fourier's law reads

$$q_r'' = -\kappa_r \partial_r T, \quad q_y'' = -\kappa_y \partial_y T, \quad q_\theta'' = -\frac{\kappa_\theta}{r}\partial_\theta T. \tag{A.23}$$

Geometrically, it comes

$$\begin{cases} q_x'' = q_r'' \cos(\theta) - q_\theta'' \sin(\theta) \\ q_z'' = q_r'' \sin(\theta) + q_\theta'' \cos(\theta) \end{cases}. \tag{A.24}$$

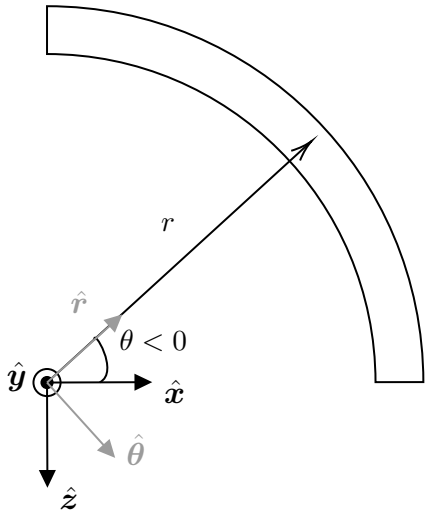

Figure A.1: Representation of the cylindrical ($\hat{\boldsymbol{r}}$,$\hat{\boldsymbol{y}}$,$\hat{\boldsymbol{\theta}}$) to Cartesian ($\hat{\boldsymbol{x}}$,$\hat{\boldsymbol{y}}$,$\hat{\boldsymbol{z}}$) system of coordinates change.

Inserting Eq. (A.23) into the previous equation and applying the chain rule with Eq. (A.22), the heat flux in Cartesian coordinates is given by

$$\begin{cases} q_x'' = -\left(\kappa_r \cos^2(\theta) + \kappa_\theta \sin^2(\theta)\right)\partial_x T - (\kappa_r - \kappa_\theta)\cos(\theta)\sin(\theta)\partial_z T \\ q_y'' = -\kappa_y \partial_y T \\ q_z'' = -(\kappa_r - \kappa_\theta)\cos(\theta)\sin(\theta)\partial_x T - \left(\kappa_r \sin^2(\theta) + \kappa_\theta \cos^2(\theta)\right)\partial_z T \end{cases} \Rightarrow \boldsymbol{q}'' = -\boldsymbol{\kappa}\nabla_{\boldsymbol{x}} T, \tag{A.25}$$

with $\boldsymbol{\kappa}$ being the tensor from Eq. (5.13).

A.7 Transverse hysteresis loss in weak penetration based on the CSM

As introduced in Section 3.5, the focus is set on $b_a \ll b_p$, no persistent currents are supposed in the initial state and the field ramp-up is supposed monotonic. The current density distribution in the filament is shown in the left part of Fig. 3.10. The moving boundary between $j = j_c$ and $j = 0$ is denoted $R_i(t, \theta)$. Cylindrical coordinates $(r, \theta, z) \in \mathbb{R}^+ \times [0; 2\pi[\times\mathbb{R}$ are preferred to study this phenomenon. In the present configuration, $h_z = e_\theta = e_r = 0$. Hence, Ampère's law (Eq. (3.14)) and the radial component of Faraday's law (Eq. (3.4)) are respectively given by:

$$\partial_r(e_z) = \mu_0 \dot{h}_\theta, \tag{A.26}$$

$$\frac{1}{r}\partial_r(r h_\theta) - \frac{1}{r}\partial_\theta(h_r) = j_z. \tag{A.27}$$

The losses per unit volume (Eq. (3.54)) averaged over one filament can be computed using

$$q_{\text{hys},1} = \frac{1}{\pi R_f^2}\int_0^{2\pi} d\theta \int_0^{R_f} \boldsymbol{e}\cdot\boldsymbol{j}\; r\, dr, \tag{A.28}$$

$$= \frac{j_c}{\pi R_f^2}\int_0^{2\pi} d\theta \int_{R_i}^{R_f} |e_z|\; r\, dr. \tag{A.29}$$

Near the moving boundary $R_i(t,\theta)$, the current density is (from CSM):

$$j_z = \mp j_c\, H(r-R_i) = \begin{cases} -j_c, & \text{if } r > R_i \text{ and } \theta < \pi \\ +j_c, & \text{if } r > R_i \text{ and } \theta > \pi \\ 0, & \text{if } r < R_i, \end{cases} \tag{A.30}$$

with $H(\cdot)$ the Heaviside step function, whose derivative (in the sense of distributions) is the Dirac delta $\delta(\cdot)$. Hence, deriving Eq. (A.27) with respect to time and introducing $R_i < r^* < R_f$ yields

$$\frac{1}{r}\partial_r\left(r\dot{h}_\theta\right) - \frac{1}{r}\partial_\theta\left(\dot{h}_r\right) = \dot{j}_z = \pm j_c\, \dot{R}_i\, \delta\left(r-R_i\right), \tag{A.31}$$

$$\Rightarrow \int_{R_i^-}^{r^*} \dot{j}_z\, r\, dr = \pm j_c\, \dot{R}_i\, R_i = r^*\, \dot{h}_\theta - \left(R_i\, \dot{h}_\theta\right)^- - \int_{R_i^-}^{r^*} \partial_\theta\left(\dot{h}_r\right)\, dr. \tag{A.32}$$

The last integral term in Eq. (A.32) can be neglected because of the small integration range ($R_i \lesssim r^* \lesssim R_f$ in weak penetration) and because one can show the argument itself is small. Moreover, $\dot{h}_\theta\left(R_i^-\right) = 0$ and Eq. (A.32) and the integral of Eq. (A.26) respectively simplify to

$$\dot{h}_\theta \approx \pm j_c\, \dot{R}_i\, R_i/r^* \approx \pm j_c\, \dot{R}_i \tag{A.33}$$

$$\Rightarrow \int_{R_i^-}^{r^*} \partial_r\left(e_z\right)\, dr = e_z(r^*) - \underbrace{e_z(R_i^-)}_{=0} = \int_{R_i^-}^{r^*} \pm\mu_0\, j_c\, \dot{R}_i\, dr = \pm\mu_0\, j_c\, \dot{R}_i\left(r^*-R_i\right). \tag{A.34}$$

During ramp-up, the current shell thickness increases, $\dot{R}_i < 0$ and

$$|e_z| = -\mu_0\, j_c\, \dot{R}_i\left(r^*-R_i\right)\, H(r^*-R_i), \tag{A.35}$$

$$\Rightarrow q_{\text{hys,1}} = \frac{-\mu_0\, j_c^2}{\pi R_f^2} \int_0^{2\pi} \dot{R}_i\, d\theta \int_{R_i^-}^{R_f} \left(r-R_i\right) \underbrace{r}_{\approx R_f}\, dr \tag{A.36}$$

$$= \frac{-\mu_0\, j_c^2}{2\pi R_f} \int_0^{2\pi} \dot{R}_i\, \left(R_f-R_i\right)^2\, d\theta. \tag{A.37}$$

In the weak penetration approximation and in the CSM context, the current distribution only depends on the applied field: $R_i = R_i\left(b_a/\mu_0\right)$. Carr [8] has shown that a surface current K [A/m] distribution of $K = 2h\sin(\theta)$ on the boundary of the cylinder can shield from an applied field h_a. Still in the weak penetration approximation, the surface current can be approximated by $K = \pm j_c\left(R_f-R_i\right)$. Hence, the current shell thickness is linked to the applied field and the integral in Eq. (A.37) can be developed:

$$R_f - R_i = \frac{2\, h_a}{j_c}\left|\sin(\theta)\right| = \frac{2\, b_a}{\mu_0\, j_c}\left|\sin(\theta)\right|, \tag{A.38}$$

$$\Rightarrow \dot{R}_i = -\frac{2}{\mu_0\, j_c}\dot{b}_a\left|\sin(\theta)\right|, \tag{A.39}$$

$$\Rightarrow q_{\text{hys,1}} = \frac{4}{\pi j_c \mu_0^2 R_f}\, b_a^2\, \dot{b}_a \underbrace{\int_0^{2\pi} \left|\sin(\theta)\right|^3\, d\theta}_{=8/3} = \frac{64}{3\pi j_c \mu_0^2 d_f}\, b_a^2\, \dot{b}_a. \tag{A.40}$$

Please note that this result has been obtained considering an external field increasing over time and a virgin superconducting initial state. Such an assumption is appropriate in the context of the ramp-up of the device.

A.8 Transverse hysteresis loss in full penetration based on the power-law model

Assuming a uniform external flux density b_a along the $\hat{\boldsymbol{y}}$-axis, increasing monotonically at a constant rate $\dot{b}_a$, the induced electric field in the filament can be estimated as $e_z = \dot{b}_a x$ in full penetration, as shown in Fig. 7.4(a). In other words, the magnetization of the filament is assumed constant. The corresponding current density distribution is given by Eq. (7.6). The filamentary hysteresis loss averaged over the volume of the filament is then, using cylindrical coordinates ($x = r\cos\theta$):

$$q_{\text{hys},1} = \frac{4}{\pi d_f^2}\int_0^{d_f/2}\int_0^{2\pi} \boldsymbol{j}\cdot\boldsymbol{e}\; r\; dr\; d\theta \tag{A.41}$$

$$= \frac{8}{\pi d_f^2}\int_0^{d_f/2}\int_{-\pi/2}^{\pi/2} j_\text{c}\left(\frac{\dot{b}_a r\cos\theta}{e_\text{c}}\right)^{1/n} \dot{b}_a r\cos\theta\; r\; dr\; d\theta \tag{A.42}$$

$$= \frac{8}{\pi d_f^2} j_\text{c}\dot{b}_a\left(\frac{\dot{b}_a}{e_\text{c}}\right)^{1/n}\int_{-\pi/2}^{\pi/2}(\cos\theta)^{(n+1)/n}d\theta\int_0^{d_f/2} r^{2+1/n}dr \tag{A.43}$$

$$= \frac{8}{\pi d_f^2} j_\text{c}\dot{b}_a\left(\frac{\dot{b}_a}{e_\text{c}}\right)^{1/n}\frac{1}{3+1/n}\left(\frac{d_f}{2}\right)^{(3+1/n)}\int_{-\pi/2}^{\pi/2}(\cos\theta)^{(n+1)/n}d\theta \tag{A.44}$$

$$= \frac{\int_{-\pi/2}^{\pi/2}(\cos\theta)^{(n+1)/n}d\theta}{(3+1/n)\pi} j_\text{c} d_f\dot{b}_a\left(\frac{d_f\dot{b}_a}{2e_\text{c}}\right)^{1/n}. \tag{A.45}$$

The second equality is obtained by symmetry of the electric field and current density with respect to the $x = 0$ axis.

APPENDIX B
ADDITIONAL TABLES AND FIGURES

B.1 Three-dimensional mesh structure

The mesh structure used for discretizing the complete 3D C400 model is shown in Fig. B.1. The mesh is composed of tetrahedra. Only their facets are shown.

B.2 Thermal properties

The numerical values of specific heat and thermal conductivity are taken from the National Institute of Standards and Technology (NIST) database [51]. Copper properties are found under *Copper (OFHC) - RRR100* (RRR100 is the closest value to RRR80), fibreglass under *Fiberglass Epoxy G-10* and stainless steel under *Stainless Steel 304L*.

Density

The thermal expansion is neglected in the present study, meaning the cryogenic densities of copper, fibreglass and stainless steel are their respective density at ambient temperature. For copper and fibreglass, the relative linear expansion between 273 K and 4 K is [51] less than 1 %, which justifies the previous assumption. The densities are

$$\rho_{\text{Cu}} = 8960 \text{ kg/m}^3, \quad \rho_{\text{fg}} = 1800 \text{ kg/m}^3, \quad \rho_{\text{ss}} = 8000 \text{ kg/m}^3, \tag{B.1}$$

respectively retrieved from [57], [58] and [59]. The effective density of the coil is $\rho_{\text{eff}} = 6955 \text{ kg/m}^3$.

Specific heat

The specific heat of the different materials has been fitted [51] using an equation of the form

$$\log_{10}(c_p(T)) = a_c + b_c\, t_c + c_c\, t_c^2 + d_c\, t_c^3 + e_c\, t_c^4 + f_c\, t_c^5 + g_c\, t_c^6 + h_c\, t_c^7 + i_c\, t_c^8, \text{ with } t_c = \log_{10}(T). \tag{B.2}$$

The corresponding coefficients are gathered in Tab. B.1. At $T_{\text{He}} = 4.2$ K, it corresponds to

$$c_{p,\text{Cu}} = 0.109 \text{ J/(kg K)}, \quad c_{p,\text{fg}} = 2.297 \text{ J/(kg K)}, \quad c_{p,\text{eff}} = 0.267 \text{ J/(kg K)}, \quad c_{p,\text{ss}} = 1.772 \text{ J/(kg K)}. \tag{B.3}$$

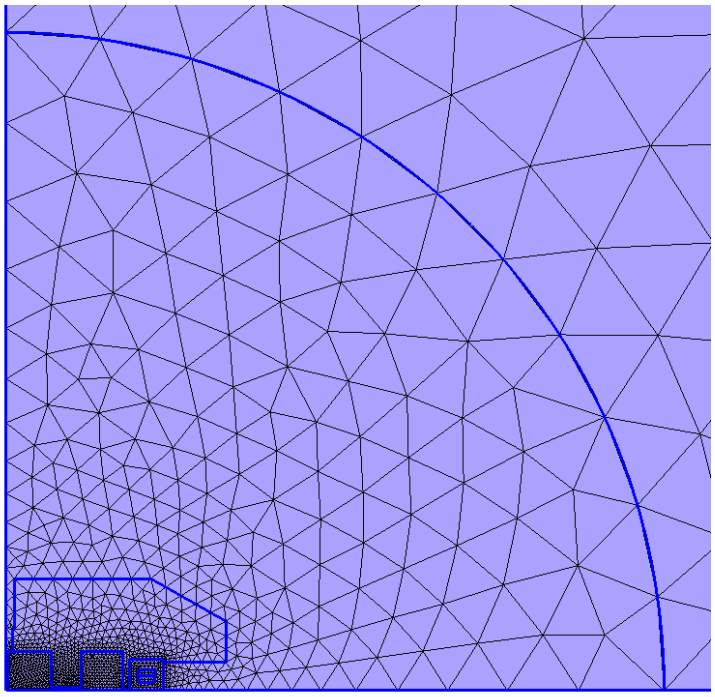

(a) Global view.

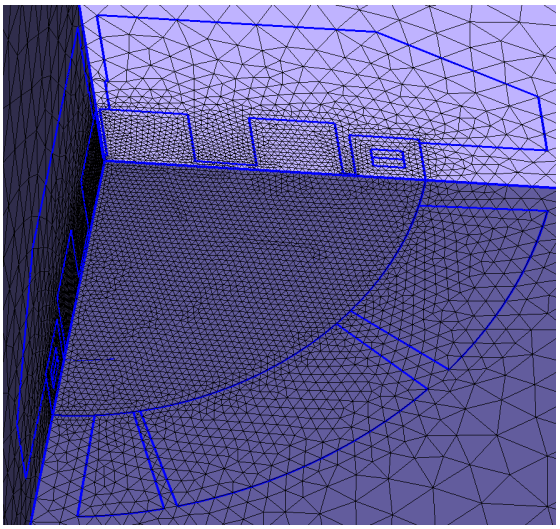

(b) Focus on the median plane.

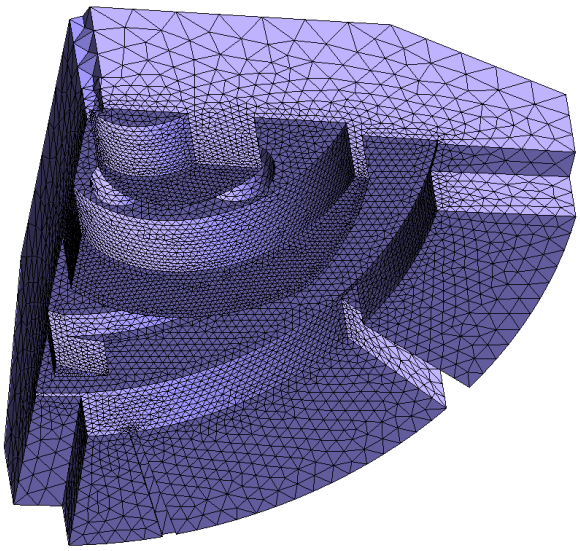

(c) Focus on the inner yoke boundary.

Figure B.1: Final mesh structure of the 3D model without helium vessel. The represented global mesh size is $s = 1$, the corresponding minimal mesh size is 30 mm. The mesh is refined where the flux density varies strongly, e. g. in the spiral ends.

Material	a_c	b_c	c_c	d_c	e_c	f_c	g_c	h_c	i_c
$c_{p,\mathrm{Cu}}$	-1.92	-0.16	8.61	-19.0	22.0	-12.7	3.54	-0.380	0
$c_{p,\mathrm{fg}}$	-2.41	7.60	-8.30	7.33	-4.24	1.43	-0.244	0.0152	0
$c_{p,\mathrm{ss}}$	-352	3120	-12000	26100	-35200	30000	-15800	4720	-611

Table B.1: Coefficients involved in Eq. (B.2), for the heat capacity of copper, fibreglass and stainless steel. From [51].

Thermal conductivity

The thermal conductivity of fibreglass (normal and warp directions) and stainless steel has been fitted [51] with

$$\log_{10}(\kappa(T)) = a_k + b_k\, t_k + c_k\, t_k^2 + d_k\, t_k^3 + e_k\, t_k^4 + f_k\, t_k^5 + g_k\, t_k^6 + h_k\, t_k^7 + i_k\, t_k^8, \text{ with } t_k = \log_{10}(T), \tag{B.4}$$

while the conductivity of copper has been fitted [51] with

$$\log_{10}(\kappa(T)) = \frac{a_k + c_k\, T^{0.5} + e_k\, T + g_k\, T^{1.5} + i_k\, T^2}{1 + b_k\, T^{0.5} + d_k\, T + f_k\, T^{1.5} + h_k\, T^2}. \tag{B.5}$$

The corresponding coefficients are gathered in Tab. B.2 and the temperature dependence of κ_{Cu}, $\kappa_{\text{fg,n}}$ and $\kappa_{\text{fg,w}}$ is represented in Fig. 5.6.

Material	a_k	b_k	c_k	d_k	e_k	f_k	g_k	h_k	i_k
κ_{Cu}	2.22	-0.475	-0.881	0.139	0.295	-0.0204	-0.0483	0.00128	0.00321
$\kappa_{\text{fg,n}}$	-4.12	13.8	-26.1	26.3	-14.7	4.50	-0.690	0.0397	0
$\kappa_{\text{fg,w}}$	-2.65	8.80	-24.9	41.2	-39.9	23.2	-7.96	1.49	-0.117
κ_{ss}	-1.41	1.40	0.254	-0.626	0.233	0.426	-0.466	0.165	-0.0199

Table B.2: Coefficients involved in Eq. (B.4) and Eq. (B.5), for the thermal conductivity of copper, fibreglass (normal and warp directions) and stainless steel. From [51].

B.3 Hysteresis loss evolution in particular zones of the coil

This section gathers the average flux density evolution in multiple zones of the coil, which are represented in Fig. B.2. The corresponding variation of the flux density $\dot{b} = \|\partial_t \bar{\boldsymbol{b}}\|$ is also shown in the respective figures. For the different zones, the filament hysteresis loss $\bar{q}_{\text{hys,1}}$ has been computed based on the CSM approximation (Eq. (3.61)) derived in Section 3.5 and used in Chapter 6 for computing the hysteresis loss at the macroscopic scale. The results are compared to the hysteresis loss retrieved from the filament model discussed in Chapter 7. Note that the local hysteresis loss $\bar{q}_{\text{hys,1}} = \bar{q}_{\text{hys}}/\lambda_{\text{SC}}$ is represented. All results are obtained from a 3D simulation with $s = 0.84$ and $\Delta t = 100$ s.

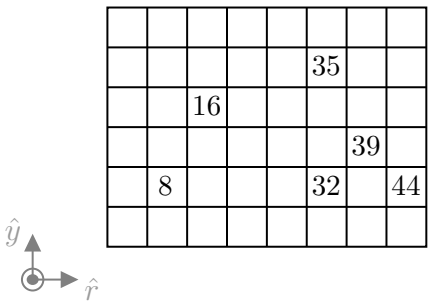

Figure B.2: Zones of the coil (cf. Fig. 8.1) for which the results are presented in this section.

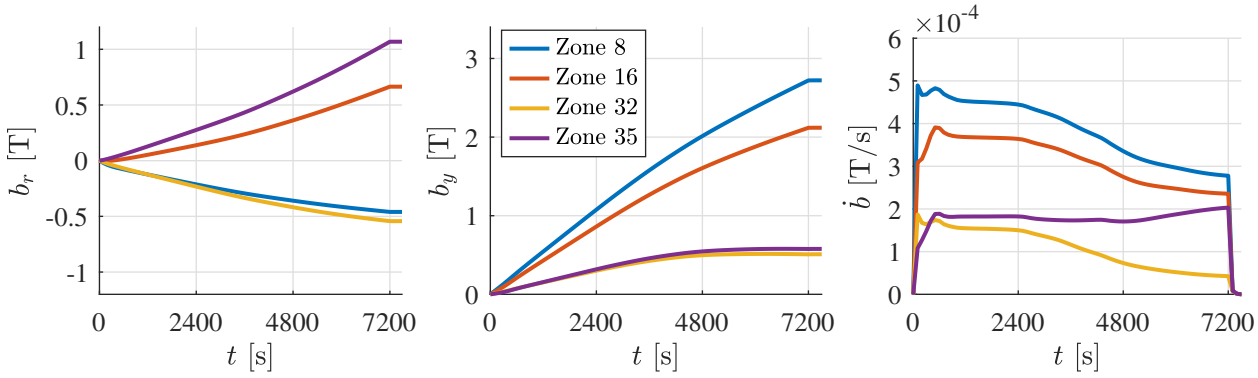

Figure B.3: Evolution of the average radial flux density $\bar{b}_r$, vertical flux density $\bar{b}_y$ and flux density variation $\dot{b}$ in zones $\{8, 16, 32, 35\}$ of Fig. B.2.

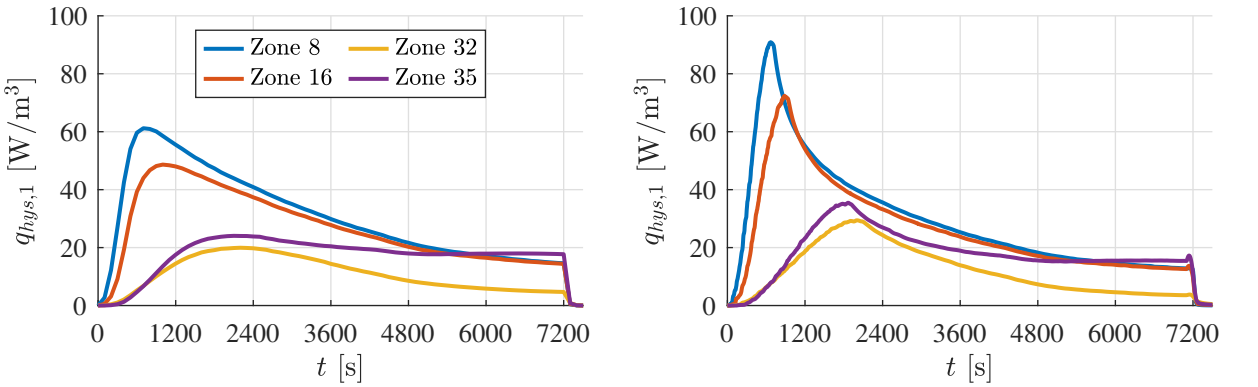

Figure B.4: Local filament hysteresis loss $\bar{q}_{\text{hys},1}$ computed (at left) from Eq. (3.61) and (at right) with the multi-scale approach, in zones $\{8, 16, 32, 35\}$ of Fig. B.2.

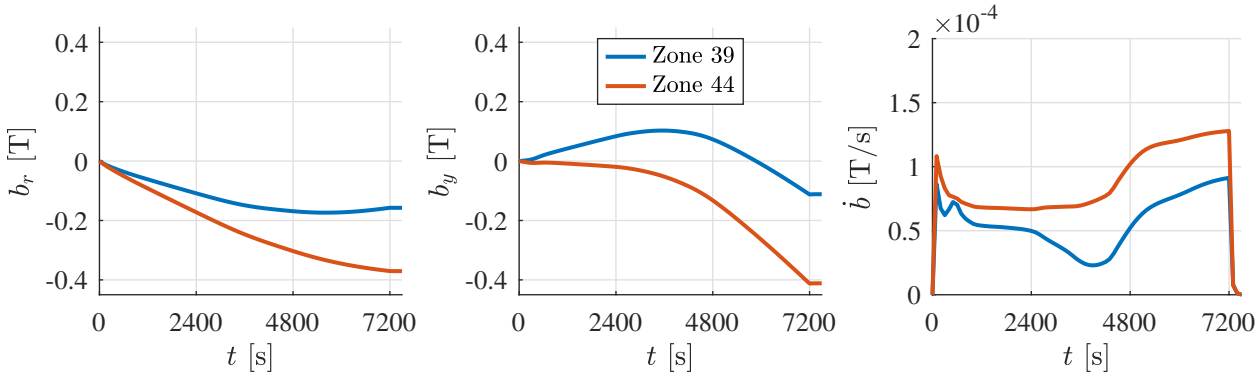

Figure B.5: Evolution of the average radial flux density $\bar{b}_r$, vertical flux density $\bar{b}_y$ and flux density variation $\dot{b}$ in zones $\{39, 44\}$ of Fig. B.2.

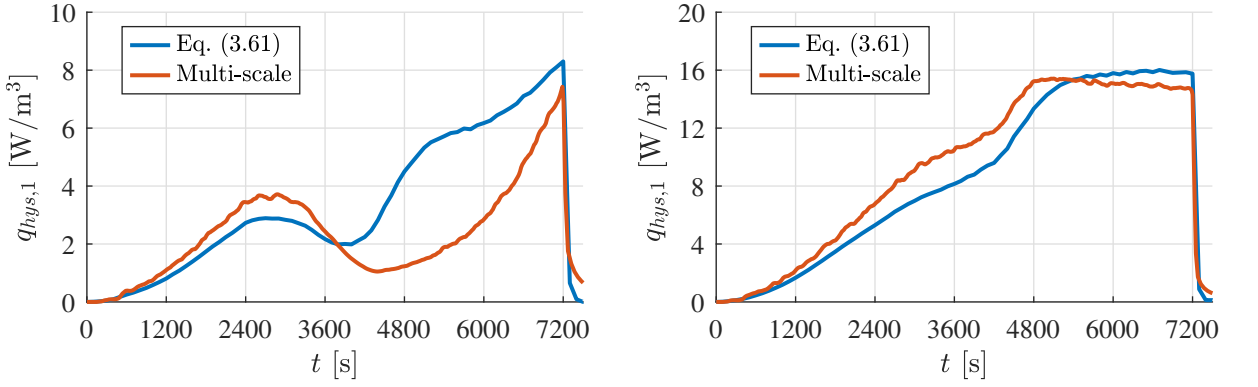

Figure B.6: Local filament hysteresis loss $\bar{q}_{\text{hys},1}$ computed with the multi-scale approach compared to the results of Eq. (3.61), in zones $\{39, 44\}$ of Fig. B.2. Zone 39 at left and zone 41 at right.

BIBLIOGRAPHY

[1] J. Mandrillon *et al.*, *Status on NHa C400 cyclotron for hadrontherapy*, presented at CYC2022, Beijing, China, Dec. 2022, paper THBI01, to be published.

[2] T. P. Orlando, K. A. Delin, *Foundations of Applied Superconductivity*, Addison-Wesley Publishing Company, 1991.

[3] M. N. Wilson, *Superconducting magnets*, Oxford University Press, 1983.

[4] P. Dular, C. Geuzaine, F. Henrotte, and W. Legros, *A general environment for the treatment of discrete problems and its application to the finite element method*, IEEE Transactions on Magnetics, vol. 34, no. 5, pp. 3395-3398, 1998.

[5] C. Geuzaine and J.-F. Remacle, *Gmsh: a three-dimensional finite element mesh generator with built-in pre- and post-processing facilities*, International Journal for Numerical Methods in Engineering, vol. 79, no 11, pp. 1309-1331, 2009.

[6] C. Geuzaine, *High order hybrid finite element schemes for Maxwell's equations taking thin structures and global quantities into account*, Ph.D. thesis, 2001.

[7] J. Dular, *Standard and Mixed Finite Element Formulations for Systems with Type-II Superconductors*, Ph.D. thesis, 2023.

[8] W. J. Carr, Jr., *AC loss and macroscopic theory of superconductors*, 2nd edition, Taylor and Francis, 2001.

[9] U. Amaldi, *Particle Accelerators: From Big Bang Physics to Hadron Therapy*, Springer, 2015.

[10] R. R. Wilson, *Radiological use of fast protons*, Radiology, vol. 47, no. 5, pp. 487-491, 1946.

[11] H. Tsujii *et al.*, *Carbon-Ion Radiotherapy: Principles, Practices, and Treatment Planning*, Springer, 2014.

[12] H. Suit *et al.*, *Proton vs carbon ion beams in the definitive radiation treatment of cancer patients*, Radiotherapy and Oncology, vol. 95, no. 1, pp. 3-22, 2010.

[13] W. H. Bragg, R. Kleeman, *On the ionization curves of radium*, The London, Edinburgh, and Dublin Philosophical Magazine and Journal of Science, vol. 8, no. 48, pp. 726-738, 1904.

[14] T. D. Malouff, A. Mahajan, S. Krishnan, C. Beltran, D. S. Seneviratne, and D. M. Trifiletti, *Carbon Ion Therapy: A Modern Review of an Emerging Technology*, Frontiers in Oncology, vol. 10, p. 82, 2020.

[15] K. Strijckmans, *The isochronous cyclotron: principles and recent developments*, Computerized medical imaging and graphics, vol. 25, no. 2, pp. 69-78, 2001.

[16] S. Zaremba, W. Kleeven, *Cyclotrons: magnetic design and beam dynamics*, Ion Beam Applications, arXiv preprint arXiv:1804.08961, 2018.

[17] Y. Jongen *et al.*, *IBA C400 cyclotron project for hadron therapy*, Cyclotrons and Their Applications, Eighteenth International Conference, 2007.

[18] L. Maunoury, P. Velten, and Y. Paradis, *Status of the Field Mapping System Design for the C400 Cyclotron*, presented at IPAC'23, 14th International Particle Accelerator Conference, Venice, Italy, May 2023, paper THPM008.

[19] W. H. Hayt, J. A. Buck, *Engineering Electromagnetics*, 6th edition, McGraw-Hill, 2001.

[20] C. Kittel, *Introduction to solid state physics*, 8th edition, John Wiley & Sons, 2005.

[21] P. Dular, *Modélisation du champ magnétique et des courants induits dans des systèmes tridimensionnels non linéaires*, University of Liège, 1994.

[22] R. V. Sabariego, *ELEC0041: Modeling and design of electromagnetic systems*, ULiège, Lecture notes, 2022-2023.

[23] B. D. Cullity, C. D. Graham, *Introduction to magnetic materials*, John Wiley & Sons, 2011.

[24] P. Ferracin, *Superconducting Magnets: Session 1*, 2019 Joint Universities Accelerator School, 2019.

[25] P. Vanderbemden, *ELEN0047-1: Superconductivity*, ULiège, Lecture notes, 2022-2023.

[26] A. Devred, *Practical Low-Temperature Superconductors for Electromagnets*, CERN, 2004.

[27] A. P. Verweij, *Electrodynamics of superconducting cables in accelerator magnets*, 1995.

[28] D. Dew-Hughes, *The critical current of superconductors: an historical review*, Low temperature physics, vol. 27, no 9, pp. 713-722, 2001.

[29] Y. B. Kim, C. F. Hempstead, and A. R. Strnad, *Critical persistent currents in hard superconductors*, Physics Review Letters, vol. 9, pp. 306-309, 1962.

[30] L. Bottura, *A practical fit for the critical surface of NbTi*, IEEE Transactions on Applied Superconductivity, vol. 10, no. 1, pp. 1054-1057, 2000.

[31] M. S. Lubell, *Empirical scaling formulas for critical current and critical field for commercial NbTi*, IEEE Transactions on Magnetics, vol. 19, pp. 754-757, 1983.

[32] T. Boutboul, S. Le Naour, D. Leroy, L. Oberli, and V. Previtali, *Critical Current Density in Superconducting Nb-Ti Strands in the 100 mT to 11 T Applied Field Range*, IEEE Transactions on Applied Superconductivity, vol. 16, no. 2, pp. 1184-1187, 2006.

[33] A. Devred *et al.*, *Status of ITER Conductor Development and Production*, IEEE Transactions on Applied Superconductivity, vol. 22, no. 3, pp. 4804909-4804909, 2012.

[34] C. Spencer, P. Sanger, and M. Young, *The temperature and magnetic field dependence of superconducting critical current densities of multifilamentary Nb3Sn and NbTi composite wires*, IEEE Transactions on Magnetics, vol. 15, no. 1, pp. 76-79, 1979.

[35] C. P. Bean, *Magnetization of hard superconductors*, Physics Review Letters, vol. 8, no.6, pp. 250–253, 1962.

[36] A. K. Ghosh, *V–I transition and n-value of multifilamentary LTS and HTS wires and cables*, Physica C: Superconductivity, Volume 401, Issues 1–4, 2004.

[37] F. Grilli, E. Pardo, A. Stenvall, D. N. Nguyen, W. Yuan, and F. Gömöry, *Computation of Losses in HTS Under the Action of Varying Magnetic Fields and Currents*, IEEE Transactions on Applied Superconductivity, vol. 24, no. 1, pp. 78-110, 2014.

[38] E. Zeldov, N. Amer, G. Koren, A. Gupta, M. McElfresh, and R. Gambino, *Flux creep characteristics in high-temperature superconductors*, Applied physics letters, vol. 56, no. 7, pp. 680–682, 1990.

[39] A. Godeke, D. Turrioni, T. Boutboul, N. Cheggour, A. K. Ghosh, L. F. Goodrich, M. Meinesz, and A. den Ouden, *Interlaboratory Comparisons of NbTi Critical Current Measurements*, IEEE Transactions on Applied Superconductivity, vol. 19, no. 3, pp. 2633-2636, 2009.

[40] F. P. Incropera, D. P. DeWitt, T. L. Bergman, and A. S. Lavine, *Incropera's Principles of Heat and Mass Transfer*, John Wiley & Sons, 2017.

[41] M. N. Wilson, *NbTi superconductors with low ac loss: A review*, Cryogenics, Volume 48, Issues 7–8, 2008.

[42] R. A. Matula, *Electrical resistivity of copper, gold, palladium, and silver*, Journal of Physical and Chemical Reference Data, vol. 8, no 4, pp. 1147-1298, 1979.

[43] N. J. Simon, E. S. Drexler, and R. P. Reed, *Properties of copper and copper alloys at cryogenic temperatures.*, NIST Publication, 1992.

[44] F. Henrotte, B. Meys, H. Hedia, P. Dular, and W. Legros, *Finite element modelling with transformation techniques*, IEEE Transactions on Magnetics, vol. 35, no. 3, pp. 1434-1437, 1999.

[45] B. Skoczen, *Stability, fatigue and optimization of thin-walled structures under cryogenic conditions: Application in the structural design of colliders and cryogenic transfer lines*, CERN, 2001.

[46] C. Y. Ho, T. K. Chu, *Electrical resistivity and thermal conductivity of nine selected AISI stainless steels*, Thermophysical and Electronic Properties Information Analysis Center Lafayette, 1977.

[47] R. A. Serway, J. W. Jewett, *Physics for Scientists and Engineers*, 9th edition, Cengage learning, 2017.

[48] E. Creusé, P. Dular, and S. Nicaise, *About the gauge conditions arising in Finite Element magnetostatic problems*, Computers & Mathematics with Applications, vol. 77, no 6, pp. 1563-1582, 2019.

[49] J. Dular, *High-Temperature Superconductor in GetDP Various Finite Element Formulations*, GetDP Workshop, CERN, 22/04/2021.

[50] L. Bottura, *Cable Stability*, CERN, 2004.

[51] *Properties of solid materials from cryogenic- to room-temperatures*, `https://trc.nist.gov/cryogenics/materials/materialproperties.htm`, Accessed: 27/05/2023.

[52] C. Geuzaine, A. Kameni, and A. Stenvall, https://gitlab.onelab.info/doc/models/-/tree/master/Superconductors, Accessed: 30/05/2023.

[53] L. Prigozhin, *Analysis of critical-state problems in type-II superconductivity*, IEEE Transactions on Applied Superconductivity, vol. 7, no. 4, pp. 3866-3873, 1997.

[54] L. Denis, C. Geuzaine, B. Vanderheyden, W. Kleeven, V. Nuttens, and P. Velten, *Finite element study of AC losses in the superconducting coil of the NHa C400 cyclotron*, presented at IPAC'23, 14th International Particle Accelerator Conference, Venice, Italy, May 2023, paper THPM095, preprint: https://hdl.handle.net/2268/303568.

[55] L. Wu, V. D. Nguyen, N. G. Kilingar, and L. Noels, *A recurrent neural network-accelerated multi-scale model for elasto-plastic heterogeneous materials subjected to random cyclic and non-proportional loading paths*, Computer Methods in Applied Mechanics and Engineering, vol. 369, p. 113234, 2020.

[56] F. Purnode, F. Henrotte, F. Caire, J. d. Silva, G. Louppe, and C. Geuzaine, *A Material Law Based on Neural Networks and Homogenization for the Accurate Finite Element Simulation of Laminated Ferromagnetic Cores in the Periodic Regime*, IEEE Transactions on Magnetics, vol. 58, no. 9, pp. 1-4, 2022.

[57] *Royal Society of Chemistry - Copper*, https://www.rsc.org/periodic-table/element/29/copper, Accessed: 27/05/2023.

[58] *G-10 Fiberglass Epoxy Laminate Sheet*, https://www.matweb.com/search/datasheet_print.aspx?matguid=8337b2d050d44da1b8a9a5e61b0d5f85, Accessed: 27/05/2023.

[59] *Thyssenkrupp Materials (UK) Ltd - Stainless Steel 1.4307 - 304L*, https://www.thyssenkrupp-materials.co.uk/stainless-steel-304l-14307.html, Accessed: 27/05/2023.